

---

Electronic Theses and Dissertations, 2004-2019

---

2017

## Heat Transfer, Friction, and Turbulent Analysis on Single Ribbed-Wall Square Channel

Christopher Vergos  
*University of Central Florida*

 Part of the [Mechanical Engineering Commons](#)  
Find similar works at: <https://stars.library.ucf.edu/etd>  
University of Central Florida Libraries <http://library.ucf.edu>

This Masters Thesis (Open Access) is brought to you for free and open access by STARS. It has been accepted for inclusion in Electronic Theses and Dissertations, 2004-2019 by an authorized administrator of STARS. For more information, please contact [STARS@ucf.edu](mailto:STARS@ucf.edu).

---

### STARS Citation

Vergos, Christopher, "Heat Transfer, Friction, and Turbulent Analysis on Single Ribbed-Wall Square Channel" (2017). *Electronic Theses and Dissertations, 2004-2019*. 5936.  
<https://stars.library.ucf.edu/etd/5936>

HEAT TRANSFER, FRICTION, AND TURBULENT ANALYSIS ON SINGLE RIBBED-  
WALL SQUARE CHANNEL

by

CHRISTOPHER E. VERGOS  
B.S. University of Central Florida, 2014

A thesis submitted in partial fulfillment of the requirements  
for the degree of Master of Science in Mechanical Engineering  
in the Department of Mechanical and Aerospace Engineering  
in the College of Engineering and Computer Sciences  
at the University of Central Florida  
Orlando, Florida

Summer Term

2017

## ABSTRACT

An experimental investigation of heat transfer and friction behavior for a fully developed flow in a non-rotating square channel was conducted under a wide range of Reynolds numbers from 6,000 to 180,000. The rig used in this study was a single ribbed wall variant of Ahmed et al.'s [ 1 ] rig from which results of this rig were compared. Ahmed et al.'s rig was a replica of Han et al.'s square channel [ 2 ] used to validate their work, and expand the Reynolds number range for both heat transfer and friction data. The test section was 22 hydraulic diameters ( $D_h$ ) long, and made of four aluminum plates. One rib roughened bottom wall, and three smooth walls bounded the flow. Glued brass ribs oriented at  $45^\circ$  to the flow direction, with a ratio of rib height to channel hydraulic diameter ( $e/D_h$ ) and a ratio of pitch to rib height ( $p/e$ ) of 0.063 and 10, respectively, lined the bottom wall. A  $20D_h$  long acrylic channel with a continuation of the test section's interior was attached at the inlet of the test section to confirm the fully developed flow. Heat transfer tests were conducted in a Reynolds number range of 20,000 to 150,000. During these tests, the four walls were held under isothermal conditions. Wall-averaged, and module-averaged Nusselt values were calculated from the log-mean temperature differences between the plate surface temperature and calculated, by energy balance, fluid bulk temperature. Streamwise Nusselt values become constant at an  $x/D_h$  of 8 within the tested Reynolds number range. Wall averaged Nusselt values were determined after  $x/D_h=8$ , and scaled by the Dittus-Boelter correlation,  $Nu_o$ , for smooth ducts to yield a Nusselt augmentation value ( $Nu/Nu_o$ ). Non-heated friction tests were conducted from a Reynolds number range of 6,000 to 180,000. Pressure drop along the channel was recorded, and channel-averaged Darcy-Weisbach friction factor was calculated within the range of Reynolds number tested. Scaling the friction factor by the smooth-wall Blasius correlation,  $f_o$ , gave the

friction augmentation ( $f/f_0$ ). The thermal performance, a modified ratio of the Nusselt and friction augmentation used by Han et al. [ 2 ], was then calculated to evaluate the bottom-line performance of the rig. It was found that the Nusselt augmentation approached a constant value of 1.4 after a Reynolds number of 60,000 while friction augmentation continued to increase in a linear fashion past that point. This caused the overall thermal performance to decline as Reynolds number increased up to a certain point. Further studies were conducted in an all acrylic, non-heated variant of the rig to study the fluid flow in the streamwise direction on, and between two ribs in the fully developed region of the channel. Single-wire hot-wire anemometry characterized velocity magnitude profiles with great detail, as well as turbulence intensity for Reynolds numbers ranging from 5,000 to 50,000. As the Reynolds number increased the reattachment point between two ribs remained about stationary while the turbulence intensity receded to the trailing surface of the upstream rib, and dissipated as it traveled. At low Reynolds numbers, between 5,000 and 10,000, the velocity and turbulence intensity streamwise profiles seemed to form two distinct flow regions, indicating that the flow over the upstream rib never completely attached between the two ribs. Integral length-scales were also derived from the autocorrelation function using the most turbulent signal acquired at each Reynolds number. It was found that there is a linear trend between Reynolds number and the integral length-scale at the most turbulent points in the flow. For example, at  $Re=50,000$  the most the length scale found just past the first rib was on the order of two times the height of the rib. Rivir et al. [ 30 ] found in a similar case that at  $Re = 45,000$ , it was 1.5 times the rib height. Several factors could influence the value of this integral length-scale, but the fact that their scale is on the order of what was obtained in this case gives some level of confidence in the value.

## **ACKNOWLEDGEMENTS**

A very special thanks to:

My family for all their love and support, Dr. Kapat for giving me an exciting and rare opportunity to learn about the fundamentals and applications of turbomachinery through the CATER Lab and graduate courses, my coworkers and project manager for all the help, support, and memorable experiences at the lab, and finally Siemens Energy for making my project possible to further the studies of internal duct cooling.

# TABLE OF CONTENTS

LIST OF FIGURES .....	vii
LIST OF TABLES .....	ix
LIST OF ACRONYMS/ABBREVIATIONS .....	x
CHAPTER 1: INTRODUCTION .....	1
CHAPTER 2: RIG SETUP.....	4
2.1 Rig Design – Heat Transfer and Friction Analysis.....	4
2.2 Rig Design – Turbulence Analysis .....	10
CHAPTER 3: TESTING .....	14
3.1 Heat Transfer Analysis .....	14
3.1.1 Flow Leakage Testing.....	15
3.1.2 Heat Leakage Testing .....	15
3.1.3 Heat Transfer Testing .....	16
3.2 Friction Analysis.....	22
3.2.1 Friction Factor Testing.....	23
3.3 Hot-Wire Analysis .....	25
3.3.1 Understanding the Bridge .....	26
3.3.2 Sensor Heat Transfer Theory .....	27
3.3.3 Limitations .....	30
3.3.4 Temperature Corrections .....	33
3.3.5 Filtering.....	34

3.3.6 Sample Convergence .....	34
3.3.7 Calibration.....	37
3.3.8 Uncertainty Considerations.....	38
<b>CHAPTER 4: RESULTS AND DISCUSSION .....</b>	<b>39</b>
4.1 Heat Transfer Analysis Results.....	39
4.2 Friction Factor Analysis Results.....	42
4.3 Thermal Performance Analysis Results.....	44
4.4 Heat Transfer and Friction Experimental Uncertainty Results.....	45
4.5 Hot-wire Analysis Results .....	46
<b>CHAPTER 5: FINDINGS .....</b>	<b>55</b>
<b>APPENDIX A: UNCERTAINTIES OF MASS FLOWRATE .....</b>	<b>58</b>
<b>APPENDIX B: SYSTEMATIC UNCERTAINTIES OF NUSSELT NUMBER ....</b>	<b>60</b>
<b>APPENDIX C: SYSTEMATIC UNCERTAINTIES OF FRICTION FACTOR .....</b>	<b>63</b>
<b>APPENDIX D: SYSTEMATIC UNCERTAINTIES OF TURBULENCE .....</b>	<b>65</b>
<b>APPENDIX E: MATLAB CODE FOR TURBULENCE ANALYSIS .....</b>	<b>67</b>
Converting Voltage Files to Velocity Files: .....	68
Velocity, Turbulence Intensity, Spectral, and Length Scale Analysis:.....	69
Sample Convergence Testing: .....	91
King’s Law Analysis: .....	92
<b>REFERENCES.....</b>	<b>94</b>

## LIST OF FIGURES

Figure 1 Heat Transfer/ Friction Rig Assembly .....	4
Figure 2 Cross-section of metal test section. ....	5
Figure 3 Electrical Schematic of Heat Transfer Test Section.....	7
Figure 4 Schematic of Heat Transfer Testing Setup.....	8
Figure 5 Schematic of Friction Testing Setup .....	9
Figure 6 Overall Rig Design.....	10
Figure 7 Test Section Rig Design.....	11
Figure 8 Hot-wire Equipment Setup for Turbulence Analysis .....	11
Figure 9 Optimized Mesh Spacing – Side-View Section .....	12
Figure 10 Heat Leakage Test Section Setup (heaters shown exposed) .....	16
Figure 11 Calculated Bulk Fluid and Measured Wall Temperature at $Re=70,000$ .....	18
Figure 12 Calculated Bulk LMTD at $Re=70,000$ .....	19
Figure 13 Calculated Modular Heat Transfer Coefficient at $Re=70,000$ .....	19
Figure 14 Calculated Modular-Averaged Nusselt Number at $Re = 70,000$ .....	21
Figure 15 Pressure Drop Across Non-Heated Rig at $Re = 70,000$ .....	25
Figure 16 Anatomy of a CTA Wheatstone Bridge Amplifier Loop .....	26
Figure 17 Energy Balance of a Hot-Wire Sensor .....	28
Figure 18 Sensor Temperature Profile – Error Zones.....	29



Figure 19 First-order Response to Temperature Step Change.....	31
Figure 20 Square-Wave Response to DANTEC Sensor.....	32
Figure 21 Convergence of the Sample Mean.....	36
Figure 22 Convergence of the Sample Standard Deviation.....	36
Figure 23 Modular Nusselt Number distribution, $Re = 70,000$ .....	39
Figure 24 Wall-Averaged Nusselt number at various $Re$ ranging from 25,000 to 125,000 .....	40
Figure 25 Channel-Averaged Nusselt Augmentation for $Re$ ranging from 25,000 to 125,000....	41
Figure 26 Fanning Friction Factor for Both Single-Wall and Two-Wall Cases.....	43
Figure 27 Friction Augmentation for Both Single-Wall and Two-Wall Cases .....	43
Figure 28 Thermal Performance for Both Single, and Two-Wall Cases .....	45
Figure 29 Sample Contour Plot .....	46
Figure 30 $Re = 50,000$ TI Repeatability Test .....	47
Figure 31 Local Velocity Normalized by the Channel Bulk Velocity.....	48
Figure 32 Uncertainty of Normalized Velocity .....	49
Figure 33 RMS Velocity Fluctuations Normalized by Local Velocity (TI).....	50
Figure 34 Uncertainty in Turbulence Intensity .....	51
Figure 35 Autocorrelation Taken at Most Turbulent Point in $Re = 50,000$ .....	53
Figure 36 Velocity and Fluctuation Plots at $Re = 50,000$ .....	56

## LIST OF TABLES

Table 1: Streamwise Hot-Wire Locations.....	13
Table 2 Hot-wire Data Validation in Heat Transfer Testing .....	52
Table 3 Location of Most Turbulent Points at Various Re.....	53
Table 4 Integral Time and Length-Scales at Various Re.....	54

## LIST OF ACRONYMS/ABBREVIATIONS

$C_p$	= Specific heat of air (kJ/kg-K)
$D_h$	= Hydraulic diameter of the channel, (m)
$e$	= Rib height, (m)
$f$	= Friction factor
$H$	= Channel height, (m)
$h$	= Heat transfer coefficient, (W/m <sup>2</sup> K)
$\dot{m}$	= Mass flowrate, (kg/s)
$Nu$	= Nusselt number
$p$	= Rib pitch, (m)
$P$	= Pressure, (Pa)
$Q_{actual}$	= Actual heat input, (W)
$Q_{leakage}$	= Heat leakage, (W)
$R$	= Resistance, ( $\Omega$ )
$Re$	= Reynolds number
$T$	= Temperature, ( $^{\circ}$ C)
$T_{amb}$	= Ambient temperature, ( $^{\circ}$ C)
$T_f$	= Bulk temperature of the fluid, ( $^{\circ}$ C)
$v$	= Velocity, (m/s)
$V$	= Voltage, (V)
$W$	= Channel width, (m)
$W$	= Rib width, (m)

$X$  = Streamwise direction, (m)

***Greek***

$\Delta$  = Difference between two parameters

$\eta$  = Thermal performance

$\mu$  = Dynamic viscosity (kg/m-s)

$\rho_{\text{air}}$  = Air density (kg/m<sup>3</sup>)

**Subscripts**

0 = Smooth channels

W = Wall

## CHAPTER 1: INTRODUCTION

To achieve higher power output and greater thermal efficiency, advanced gas turbines run at higher inlet temperature ( $\sim 1600^{\circ}\text{C}$ ), exceeding the metallic airfoils' material melting temperature within the turbine. The airfoils at the greatest risk to failure due to thermal stresses and/or melting is the first stage of vanes and blades. In modern advanced gas turbines, both thermal barrier coating (TBC) and a variety of blade cooling techniques, including pin fins, crossovers, and impingement jet inserts, and advanced trailing edges ensure the airfoil's survival during its expected life cycle, and the successful operation of the engine. In one of such cooling technique, compressor air, bled out from one of its final stages before combustion, serpentine in multi-pass flow channels within the hollow airfoil which is known as Internal Duct Cooling (IDC). Turbulators, often incorporated in these passages, interrupt viscous sublayer formation, and promote mixing of the hotter fluid near the metallic surface with the colder fluid at the core, enhancing the heat transfer. Unfortunately, turbulators are also responsible for high pressure losses due to friction beyond typical surface roughness. To optimize the cooling performance of internal cooling channels, maximizing the amount of heat removed while simultaneously minimizing the pressure loss is critical. For the past fifty years, researchers have been improving the Heat Transfer Coefficient ( $h$ ) values (both local and overall) and friction factor in a plethora of turbulated internal cooling passage variations to further improve the cooling of the IDC airfoil passages.

Several parameters, including rib pitch, height, and angle, dictate whether an arrangement of rib turbulators will perform better than others. They are expressed as non-dimensional ratios such as  $p/e$  (pitch to height ratio),  $e/h$  (blockage ratio) to characterize the various channels studied. Aspect

ratio of the channel, number of ribbed walls in cooling channels, and rib arrangement (in line, staggered, v- and w- pattern) are all non-rib specific features also explored in this field of study. Han et al. [ 3 ][ 4 ] conducted many studies on these aspects of the rib turbulators. Rib angles between  $45^\circ$  and  $60^\circ$  show better thermal performance than transverse ribs ( $90^\circ$ ) during their tests, and a p/e of 10 was best for rectangular two-ribbed wall channels [ 5 ][ 6 ]. Park et al. [ 7 ] concluded that narrower aspect ratio channels yielded results favorable to that of larger aspect ratio channels, and that thermal performance is highly dependent on what aspect ratio the channel is and what angle the ribs are oriented in. In one such test, the narrow channel ( $AR=1/2$  or  $1/4$ ) showed higher thermal performance with  $45^\circ/60^\circ$  ribs, while, the wider channel ( $AR=4$  or  $2$ ) performs better with  $30^\circ/45^\circ$  ribs. Taslim and Lengkong [ 8 ] [ 9 ] found that transverse ribs show better thermal performance than  $45^\circ$  ribs for high blockage ratio ( $e/D_h=0.25$ ) ribs in a square channel, and that rounded-corner ribs show reduction in both heat transfer and friction factor. Taslim et al. [ 10 ] even investigated the effect of the number of ribbed walls, and discovered a full set of turbulated walls has a lot of potential for increasing the heat transfer performance. Berger and Hau [ 11 ], Bailey and Bunker [ 12 ], and Wang et al. [ 13 ] also conducted studies on several aspects of rib turbulators. Various rib configurations were also considered, such as continuous and broken V shaped, W shaped and wedges [ 14 ][ 15 ][ 16 ], etc. Even different measurement techniques were used to study IDC. Rau et al. [ 17 ] used Laser-Doppler Velocimetry (LDV) as well as thermochromic liquid crystal (TLC) to investigate the detailed heat transfer and aerodynamic behavior of a square channel with transverse ribs (blockage ratio equal to 0.1). With these methods, flow near the ribs was discovered to be very complex and three-dimensional, and that the average heat transfer data typically resolved in IDC tests may not entirely capture the true

thermal performance, due to inaccurate assumptions made for local heat transfer on the wall surface near the ribs.

Because of all these dependencies, and parametrization, no two researchers have rigorously studied a single set of rib parameters, especially at high Reynolds numbers. Most experiments found in literature focus on  $Re$  lower than 70,000. Rallabandi et al. [ 18 ] investigated the heat and pressure drop correlations for a square channel with  $45^\circ$  ribs by varying rib height to channel hydraulic diameter ratio  $e/D_h$  in the range between 0.1 and 0.18. Correlations proposed by Han et al. [ 6 ][ 19 ], where  $0.048 < e/D_h < 0.078$ ,  $10 < p/e < 20$ , and  $Re < 70,000$ , were modified to expand Reynolds numbers in the range of 30,000-400,000. This set the stage to investigate the effect of heat and pressure drop in the higher Reynolds numbers. Very few studies, however, were conducted on single ribbed-wall channels throughout the history of IDC research. Chandra et al. [ 20 ][ 21 ] found that although adding more ribbed walls increases average heat transfer with increasing  $Re$ , friction factor increases far more. Thus, the overall thermal performance of the channel suffers.

This thesis intends to shed light on the heat transfer and friction behavior of a fully developed turbulent flow in a square channel with  $45^\circ$  ribs and  $e/D_h=0.0625$ , with a single wall of ribbed turbulators. Except for the single ribbed wall, this set of rib parameters match Ahmed et al.'s research [ 1 ], which was conducted to validate the findings of Han et al.'s NASA Contractor Report in 1984 [ 2 ], in a wide range of  $Re$  from 6,000 to 180,000. In addition to heat transfer and friction, constant-temperature hot-wire anemometry will offer information on the turbulence behavior of the fluid under a moderate range of  $Re$  from 5,000 to 50,000.

## CHAPTER 2: RIG SETUP

### 2.1 Rig Design – Heat Transfer and Friction Analysis

The experiment divided into three test setups: heat transfer, friction, and turbulence analysis. The heat transfer rig was an isothermal heated square channel ( $AR=1$ ). Square ribs, featuring a pitch to height ratio ( $p/e$ ) of 10 and height to channel diameter (blockage) ratio ( $e/D_h$ ) of 0.0625 with an angle-of-attack of 45 degrees against the flow, lined the bottom wall of the channel only. The total length of the rig measured  $48D_h$  with a ribbed unheated acrylic inlet of  $20D_h$  to achieve hydrodynamically-developed flow upon entering the  $22D_h$  heated aluminum test section with glued brass ribs to continue of the rib geometry from the inlet. The flow then exited through a  $6D_h$  unheated acrylic smooth square duct to diminish any back-pressure effects from a dump diffuser box further downstream. Eight equally-spaced 1/16in dia. static-pressure tap holes were drilled into each aluminum wall from end to end, except the bottom to extract pressure drop data for friction analysis. In addition to the pressure taps in the test section, pressure taps line the left and right walls of the inlet section with a third of the test section spacing. Refer to Figure 1 below.

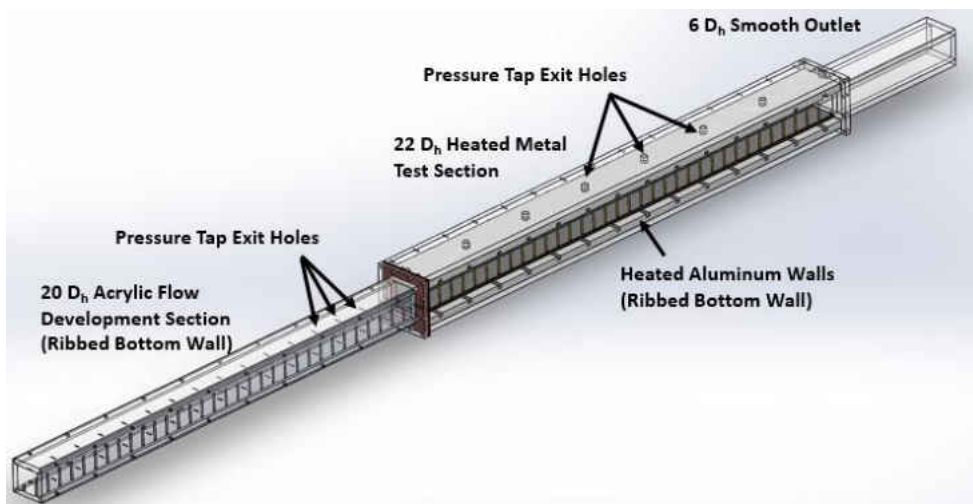


Figure 1 Heat Transfer/ Friction Rig Assembly



Between each pressure tap hole, two silicone rubber etched-foil heaters, bonded to the backs of each aluminum plate with double-sided polyimide tape from Kapton Tape<sup>®</sup>, totaled fourteen per wall. Beneath the center of each of the fourteen heaters per wall, two T-type thermocouples were cemented in small potting holes 1mm below the flow surface inside the channel. The cement used to secure these thermocouples was OMEGABOND<sup>®</sup> OB-600 high-temperature cement. All 112 test section thermocouples, with six more for test section inlet and outlet air temperature measurements, were routed to an array of six computer-controlled FLUKE 2640 NetDAQs to record, and check all rig temperatures simultaneously to support near-isothermal conditions, min/max rig temperature difference < 0.8°C, at any Reynolds number. 1mm thick strip cork insulated each heated aluminum wall from each other with their corner, and 0.5in-thick casing of Rohacell<sup>®</sup> foam core board (thermal conductivity ~ 0.03W/m-K) insulated the walls from the environment. Beyond the foam insulation, 0.5in-thick acrylic outer walls were bolted together to hold the structure of the glued metal interior. See Figure 2.

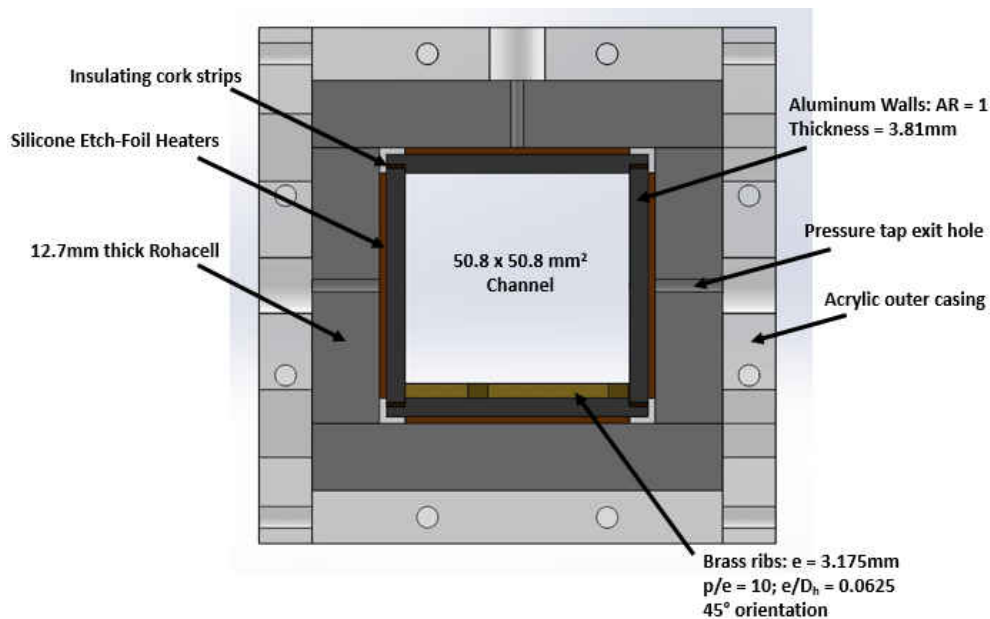


Figure 2 Cross-section of metal test section.

Designing the rig for isothermal wall temperatures, the heaters had to give various thermal loads to the rig in the streamwise direction along each wall. The ribbed wall needed the highest amount of heating to keep a target temperature because of the added cooling turbulent mixing caused by the ribs. The top smooth wall needed the least amount of cooling because it will see a greatly dampened effect from the turbulent mixing occurring on the bottom ribbed wall. The side walls needed a heat flux somewhere in between the bottom ribbed wall, and the top smooth wall requirements because near the ribs, the side walls will be cooled more effectively from the turbulent mixing pickup than near the smooth top wall. Between the two side walls, both needed about the same amount of heat flux. However, the left wall, where the ribs are directing toward at  $45^\circ$ , needed a small amount of added flux because the ribs cause a steering of the flow toward it, creating a level of impingement. Secondary vortices caused by the ribs add another, more local, cooling of the left wall through mixing in the recirculation regions upstream and downstream of the rib [ 22 ].

Knowing this, the electrical input to the test section had to be divided into three electrically heated zones: the top wall, bottom ribbed wall, and left-right (paired) walls. It was then further divided into nine streamwise sections per wall, which will be called modules, hereafter. A single rheostat controlled each module on each wall, totaling 36 rheostats. The first four modules on each wall were single-heater modules because control of the heat input was crucial in this entrance region. As the ambient air entered the test section from the inlet, the plates needed a large amount of heat flux at the entrance to maintain isothermal conditions throughout the channel. The large power demand from the heaters quickly died out as the plates heated the air to a higher bulk temperature compared to ambient downstream of the entrance. After the first four modules on each wall, the remaining five modules per wall used two heaters. Total control over each heater was not necessary

in the middle of the rig because the air temperature in the channel is high enough to have negligible effect on the heat transfer coefficient. However, the final module on each wall needed slightly more power than the earlier inner modules. Unlike the earlier modules, the final module does not have a heated exit downstream of it. It has the non-heated smooth acrylic outlet section. This induces a thermal back-pressure effect, which required the final module to work harder to maintain temperature than the ones prior. This final module, named the thermal exit module, was not included in the trends of the heat transfer analysis. Fifteen variacs (two controlling the first four modules, one for the next four modules, and one for the final module) power the rig’s three heated zones (Figure 3).

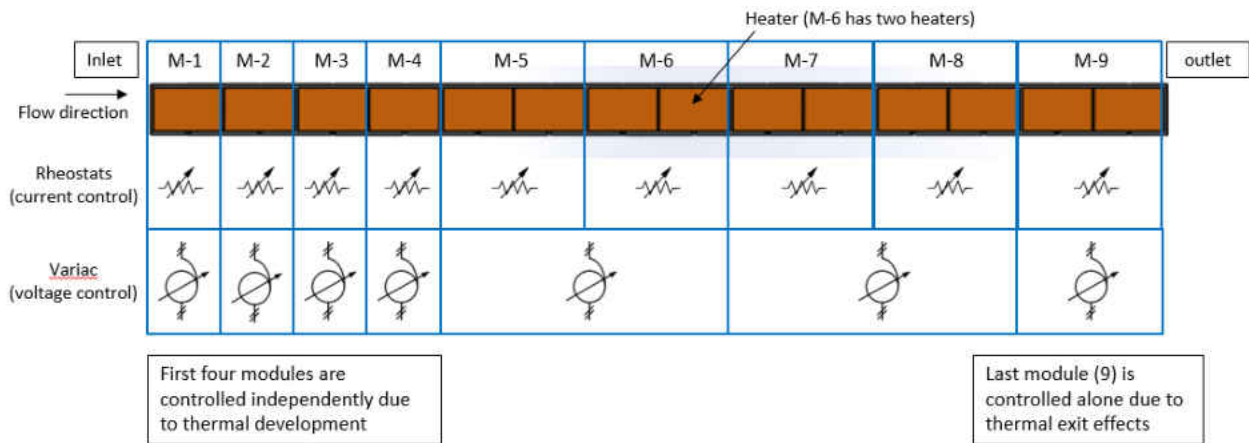


Figure 3 Electrical Schematic of Heat Transfer Test Section

A FLUKE 2638A Hydra DAQ acquired voltage information from the 36 total modules. A single VB110 Spencer® Vortex blower provided the flow through the rig under suction, and mass flowrate was measured from in-house, sonic nozzle calibrated Preso® venturi flowmeters just upstream of the blowers (Figure 4).

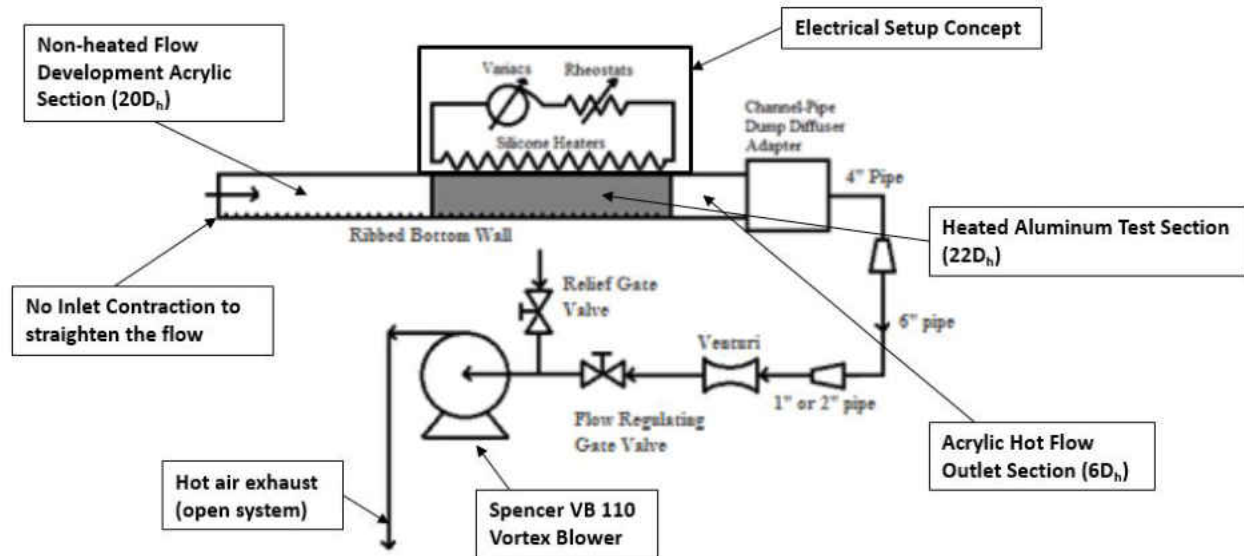


Figure 4 Schematic of Heat Transfer Testing Setup

Two OMEGA HHP240 – 5psi range handheld differential manometers measured both the venturi upstream pressure, and the venturi pressure differential simultaneously. An external barometer measured atmospheric pressure. A single calibrated T-type thermocouple measured the Venturi inlet temperatures. A gate valve in the blower piping adjusted the flow coming from the rig to acquire Reynolds numbers ranging from 6000 to 180,000. A relief valve controlled the rig exhaust temperature so the PVC does not sag due to increasing temperatures.

The friction test setup was the same setup as the heat transfer testing, however, during the friction testing, no heaters in the test section were active. It was an ambient temperature test (Figure 5).

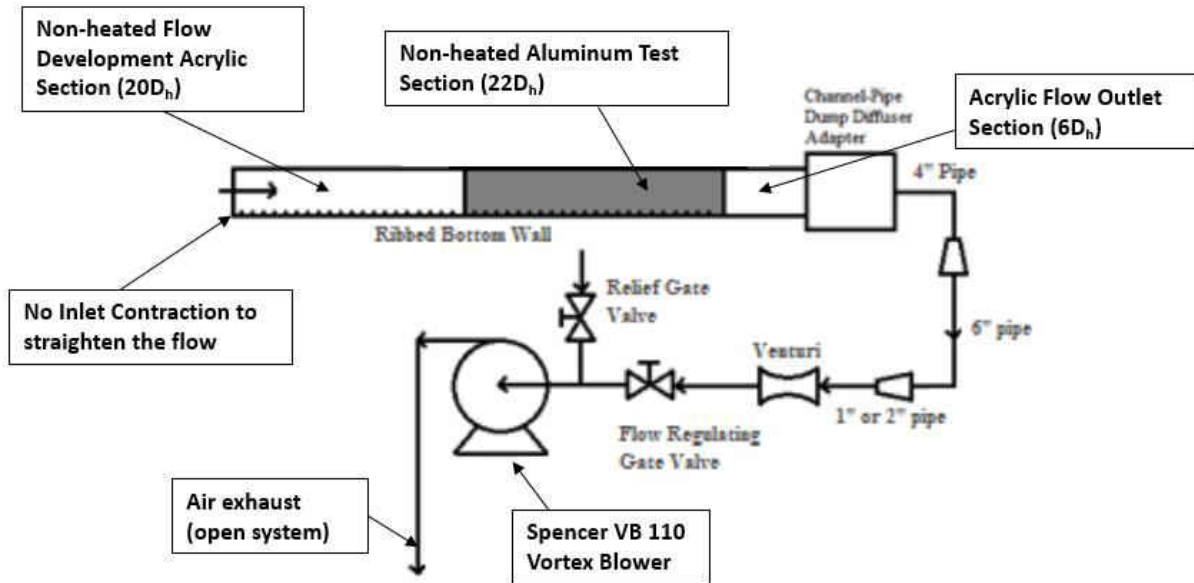


Figure 5 Schematic of Friction Testing Setup

The pressure taps along the test section and inlet section at known distances apart from each other were routed to a computer-controlled Single Scanivalve System (SSS48C Mk4) pressure scanner via vinyl tubing. The Scanivalve, and the pressure information from its transducer were controlled and recorded via LabView on the computer. Pressures inside the rig were close to that of smooth wall rigs given that this rig only has a single ribbed wall. Therefore, a 20inH<sub>2</sub>O range transducer sufficed rather than a usually equipped 5-psi range transducer. Utilizing the smallest range possible for a test allows for the acquisition of data with higher accuracy. Since no voltage needed to be recorded from the heaters, and no steady state temperature of the rig needed to be reached, the friction tests were much faster than heat transfer tests. This allowed more friction tests to be conducted, and more confidence in the shape of the correlation curve between friction factor and Reynolds number during post-processing.

## 2.2 Rig Design – Turbulence Analysis

The metal test section was removed after completing the heat transfer and friction analyses, and a  $20D_h$  acrylic turbulence test section was inserted between the ribbed inlet and smooth exit, Figure 6. The top wall of the turbulence test section was modified to be broken into three puzzle-piece components: a  $15.6D_h$  entrance plate, a  $1.56D_h$  interrogation plate, and a  $2.84D_h$  exit plate. The interrogation plate was machined to allow a rectangular piece with a centered hole to slide freely inside. Because the rig was under suction from the Vortex blowers, the rectangular slide piece was sucked to the interior surface of the interrogation piece, creating a seal. This allowed a single wire hot-wire probe to be inserted through the rectangular piece's hole and traverse freely in the streamwise direction without flow leakage through a traditional traverse slot. A traverse slot on the bottom of the interrogation piece allowed the single wire hot-wire probe to measure velocity magnitudes, and turbulence intensities between and on top of two ribs, rib 57 and 58, out of a total of 63 ribs, Figure 7.

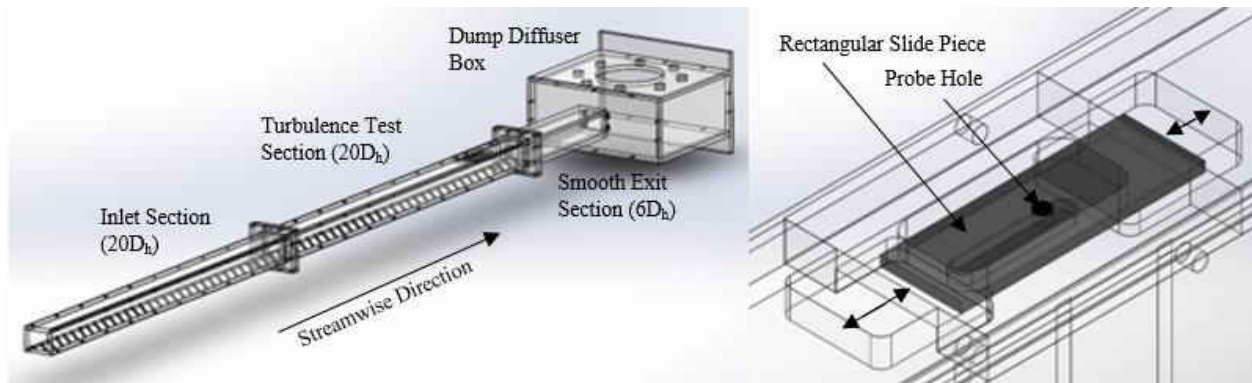


Figure 6 Overall Rig Design

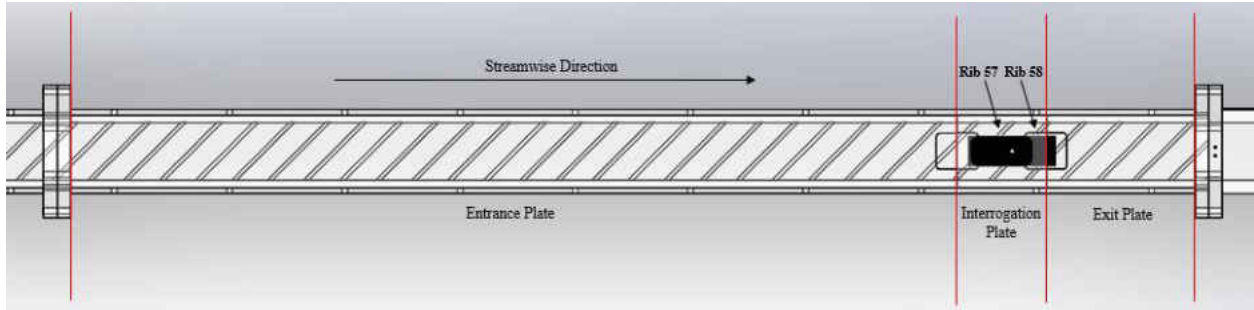


Figure 7 Test Section Rig Design

The hot-wire system comprised of a USB-controlled DANTEC Dynamics StreamLine Pro Constant Temperature Anemometer (CTA) with a 55P11 single-sensor miniature wire probe, a TSI™ 1127 manual flow nozzle calibrator, a VELMEX XSlide™ stepper-motor 2-D traverse assembly with NI motion controls, and an NI PXI-e Chassis for the computer to communicate with the motion controls through NI MAX software. To make sure that none of the above-mentioned instruments interferes with the CTA, the CTA was plugged in to its own electrical outlet, and that the BNC cable for the probe was away from any EMF emitter in the immediate area. See Figure 8 for further details.

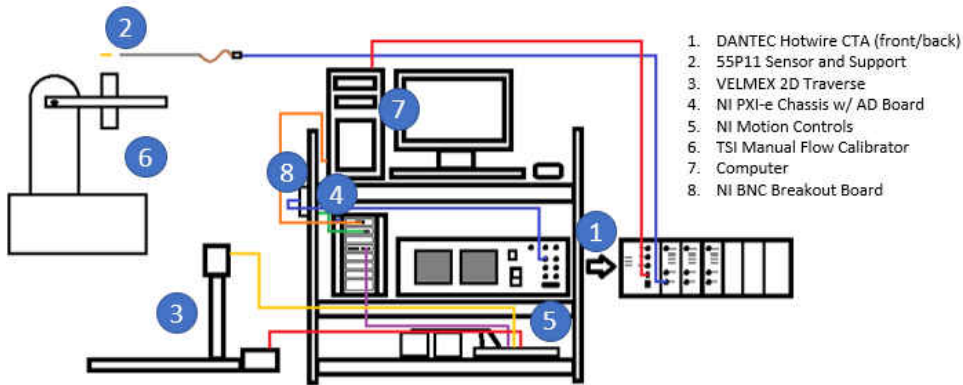


Figure 8 Hot-wire Equipment Setup for Turbulence Analysis

The same VB110 Spencer® Vortex blower provided the flow through the rig under suction. A pitot static probe was inserted into a small  $3D_h$  smooth inlet upstream of the ribbed inlet section to measure the flowrate going through the rig. Lastly, a 3mm-square mesh grid was attached to the entrance to add turbulence to the flow from the start. The interrogation plane, located on the rig's streamwise midplane, comprised of 15 streamwise locations of interest. Three of the location were located on the leading edge, mid-rib, and trailing edge of the first rib, and two locations on the leading and mid-rib points on the second rib. The rest of the streamwise location were below-rib. Preliminary testing on this rig with a very fine spacing up to 500 points within a 33.63mm x 19.18mm plane was done to figure out the optimal wall-normal spacing for each grid streamwise location. After the data was processed, several points were taken out while keeping the structure of the velocity and standard distribution curves at each streamwise location. The optimal spacing is shown below in Figure 9, which is comprised of 200 points located at each intersection of the black lines.

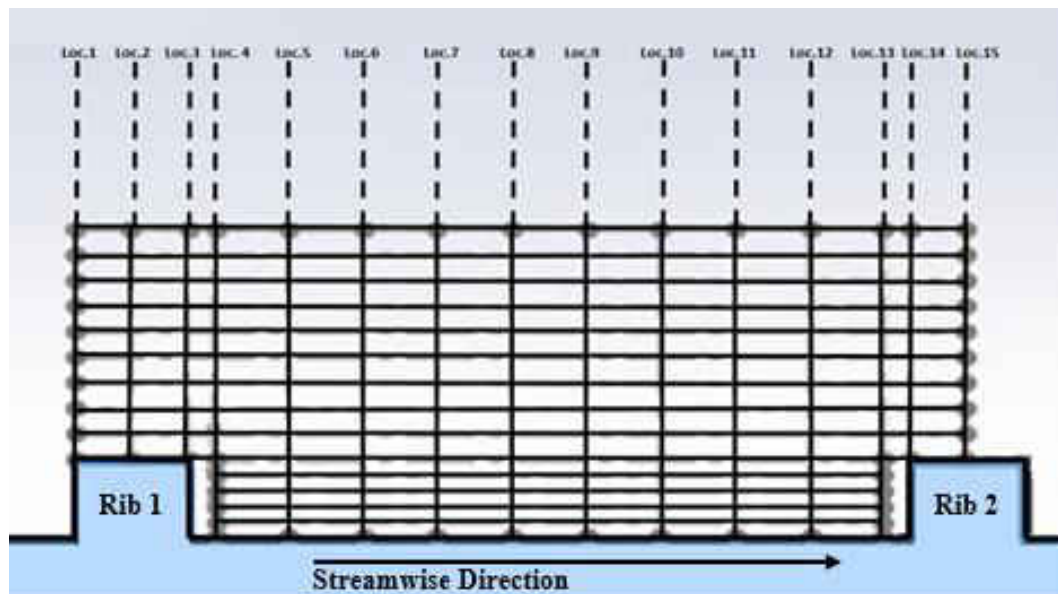


Figure 9 Optimized Mesh Spacing – Side-View Section



The wire does not go all the way down to the surface, but hovers about 0.15mm above at all streamwise locations. Sensor wire positions should always face perpendicular with the flow direction, so velocities could not be measured flush against the rib walls (Rib 1 trailing wall, and Rib 2 leading wall) because the ribs faced 45° to the wire. To make sure the wire does not hit the ribs and break, ‘buffer’ regions were calculated to accommodate the 45° angle between the wire and the ribs. These buffer regions, measuring 1mm streamwise, were positioned between locations 3 and 4, and 13 and 14. To verify that the flow was fully developed, locations 1-2, and 14-15 were critical because location 1 and 14 should have the same velocity and turbulence intensity profiles, as well as location 2 and 15. The grid spacing in region named the valley, between the ribs near the wall’s surface, was finer than the grid spacing outside, above the ribs. Studies suggest that the flow behavior within this valley region contains rapidly changing velocities and turbulent intensities due to the wall’s no-slip conditions, the recirculation zones in front of and behind the ribs, and the flow reattachment point at the wall. The vertical, y-direction, grid spacing in the valley was 0.63mm, while the grid spacing outside this region was 1.06mm.

Table 1 below show the distances of each streamwise location with a starting point at the first rib’s leading edge (location 1). Additional information of the location’s distance with respect to the length of the entire rig is also given in non-dimensional distance ( $x/D_h$ ).

Table 1: Streamwise Hot-Wire Locations

Streamwise Location	1	2	3	4	5	6	7	8
Dist. from rib 1-edge (mm)	0.00	2.16	4.32	5.32	8.12	10.91	13.70	16.50
Dist. From rig start ( $x/D_h$ )	35.00	35.04	35.09	35.10	35.16	35.21	35.27	35.32
Streamwise Location	9	10	11	12	13	14	15	
Dist. from rib 1-edge (mm)	19.29	22.09	24.88	27.67	30.47	31.47	33.63	
Dist. From rig start ( $x/D_h$ )	35.38	35.43	35.49	35.54	35.60	35.62	35.66	

## CHAPTER 3: TESTING

### 3.1 Heat Transfer Analysis

The purpose of conducting this test was to find when the flow inside a heated channel will become fully thermally developed, and how the wall-averaged Nusselt number changes as a function of Reynolds Number. Due to the mixing mechanic of turbulent flows, heat transfer is enhanced beyond the threshold of laminar flow heat transfer. Studies using rib-turbulated channels found a higher thermal performance than that of studies conducting with smooth channels. This showed a promising future in blade cooling research for more efficient gas turbines engines. With greater thermal performance of internal cooling, engines can burn hotter, less combustion cooling, and creep closer toward the harnessing true potential of natural gas.

This section marks the first of three in the chapter dedicated to the testing conducted in this research. Here the heat transfer testing approach will be explained from preparatory flow and heat leakage testing to the actual heat transfer analysis, in which an energy balance fluids temperature marching scheme will be introduced, as well as the use of LMTD for constant temperature walls. From there, an elaboration on how both modular-averaged, and wall-average heat transfer coefficient and Nusselt values can be calculated from the LMTD. An augmentation of the Nusselt results will also be presented using smooth-pipe the Dittus-Boelter correlation for turbulent flow as a reference to prove the enhancement this rib geometry delivers to the channel cooling effectiveness.

### 3.1.1 Flow Leakage Testing

Before running a heat transfer test, it was important to make sure that the rig was completely sealed. Any cool air from the environment leaking into the heated rig under suction would cause temperatures to fall, and require an, otherwise unnecessary, increase in power to maintain the target plate temperature. The resulting heat transfer coefficient in the affected area would be predicted higher than what it really should be. To make sure the rig was leak-proof, incense was lit with a match to produce smoke. The incense stick was taken along the rig, and if the leak was present, the smoke will get sucked into the rig, instead of going up into the air. If a leak was discovered, silicone caulking was used to cover up the leak and let dry. Downstream of the rig, the piping to the blower was also checked for leaks. Any leaks downstream of the rig would cause an inaccurate, overprediction in the rig mass flowrate due to an additional source of air to the blower other than the rig. Checks were also made downstream of the venturi, but made no difference to the mass flow calculation because the calculation was made at the venturi, not downstream of it. The only change it would cause was the highest Reynolds number achievable in the rig since the blower has a maximum pressure drop of 200inH<sub>2</sub>O. To make the rig leaks as noticeable as possible, the highest Reynolds number the blower allowed was put through the rig.

### 3.1.2 Heat Leakage Testing

Despite there being a 0.5in layer of Rohacell<sup>®</sup> and another 0.5in thick layer of acrylic, nothing is a perfect insulator, and heat loss to the surrounding must be accounted for to obtain accurate heat transfer data. Prior to testing, the inlet and exit of the test section was blocked off so that no air flow can go in or out (Figure 10).

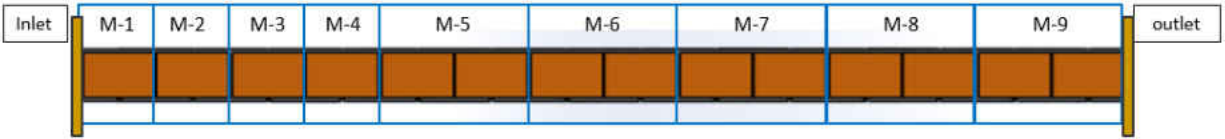


Figure 10 Heat Leakage Test Section Setup (heaters shown exposed)

The aim of the test was to create a 3-point linear curve-fit correlating the rig-surrounding temperature difference, and the required energy input from the silicone heater pads. If the rig was truly adiabatic, the energy input needed to maintain a steady rig temperature would be zero. Therefore, the nonzero energy input will be equivalent to the heat loss from the rig. These heat losses were recorded at rig temperatures of 50°C, 60°C, and 70°C along with the ambient temperature, and the difference between rig and ambient temperature was correlated with the required heat input. Heater resistances were also measured to account for the temperature dependence of electrical resistance, and were also correlated to the rig temperature with a linear curve-fit. Because only three points were taken to define the linear trend, these curves usually had high uncertainty. This was considered acceptable base on the fact that the magnitude of the heat loss compared to the overall heat flux due to convective cooling is very low, typically around 4-5%.

### 3.1.3 Heat Transfer Testing

A bulk fluid temperature marching scheme base on energy balance, and the log-mean temperature difference, LMTD, are used to determine the temperature difference between the isothermal plate and the air at each module. A pair of thermocouple are placed midway through the acrylic inlet of the rig to measure the inlet air bulk temperature. Since the air velocities are within the

incompressible regime ( $Ma < 0.3$ ), the total temperature the thermocouples are reading will match the bulk air temperature, and the effect of kinetic energy transfer to thermal energy at the thermocouple bead's stagnation point will be negligible.

When the first four modules from each wall reaches a steady state temperature, the power input to the heaters are added up, and the heat leakage, calculated by the plate-ambient temperature difference, is subtracted from that power input to give the conducting heat input through the aluminum plates at those four first modules. Knowing the heat capacity of the air is about constant ( $\sim 1.006 \text{ kJ/kg-K}$ ) and the mass flowrate from the venturi flowmeter, the fluid bulk temperature can be determined by the equation:

$$T_{air_{bulk,f}} = T_{air_{bulk,i}} + \frac{Q_{act}}{c_p \dot{m}} \quad (3.1)$$

where  $T_{air_{bulk,i}}$  is the averaged bulk fluid temperature entering the module,  $Q_{act}$  is the actual heat input to the aluminum plates after subtracting heat leakage, and  $T_{air_{bulk,f}}$  is the bulk fluid temperature exiting the heated module. The next modular bulk fluid temperature would use the calculated first modular bulk fluid temperature, and reiterate the process with the next averaged wall temperature and heat input, creating a marching scheme. This reiteration of fluid bulk temperatures marches all the way to the last module where thermocouples are inserted just downstream through an acrylic flange to directly measure the test section exit temperature. Ideally, the calculated final module bulk temperature should match exact with the measured exit temperature.

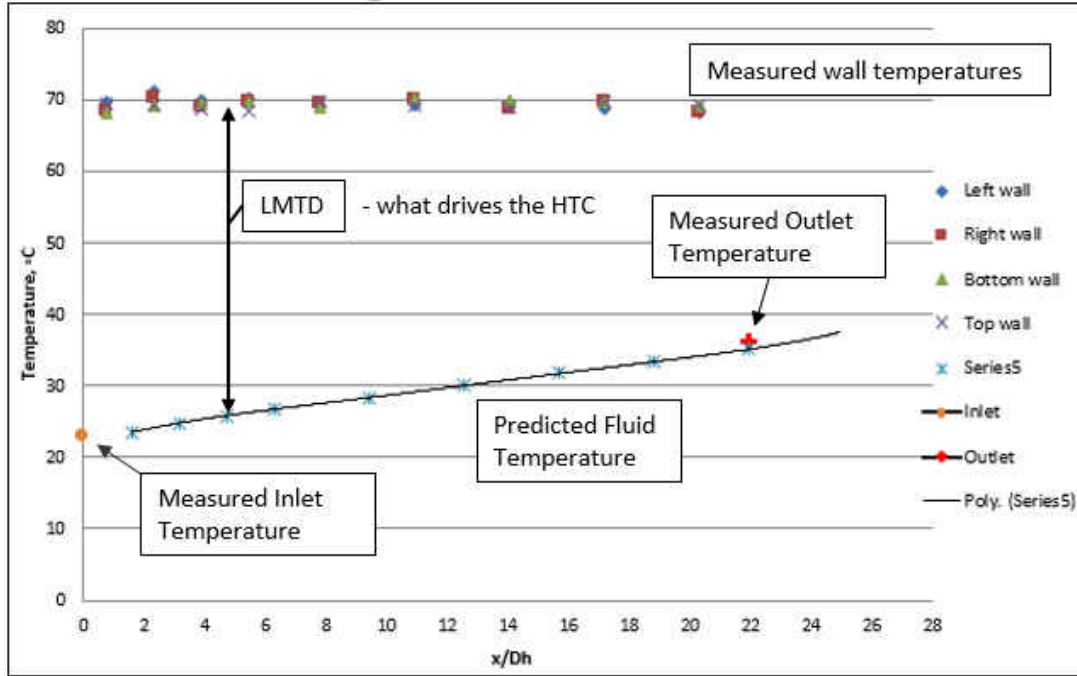


Figure 11 Calculated Bulk Fluid and Measured Wall Temperature at Re=70,000

The logarithmic mean temperature difference,  $LMTD_x$ , method was used to average the difference between the calculated fluid temperatures and constant wall temperature at each module:

$$LMTD_x = \frac{(T_{w,x} - T_{f,i,x}) - (T_{w,x} - T_{f,o,x})}{\ln\left(\frac{T_{w,x} - T_{f,i,x}}{T_{w,x} - T_{f,o,x}}\right)} = \frac{T_{f,o,x} - T_{f,i,x}}{\ln\left(\frac{T_{w,x} - T_{f,i,x}}{T_{w,x} - T_{f,o,x}}\right)} \quad (3.2)$$

where  $T_{w,x}$ ,  $T_{f,i,x}$ , and  $T_{f,o,x}$  are the wall temperature, income bulk fluid temperature and outgoing fluid temperature, respectively, of a module at location  $x$  (Figure 12).

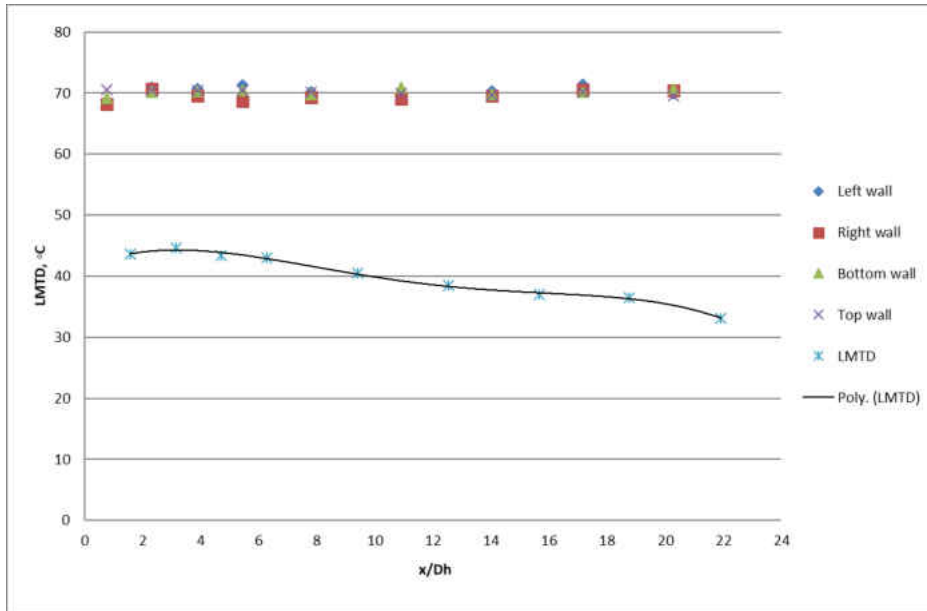


Figure 12 Calculated Bulk LMTD at Re=70,000

The LMTD was then factored into a module based Newton cooling equation to calculate the module's heat transfer coefficient,  $\bar{h}_x$ .

$$\bar{h}_x = \frac{Q_x}{A_x(LMTD_x)} \quad (3.3)$$

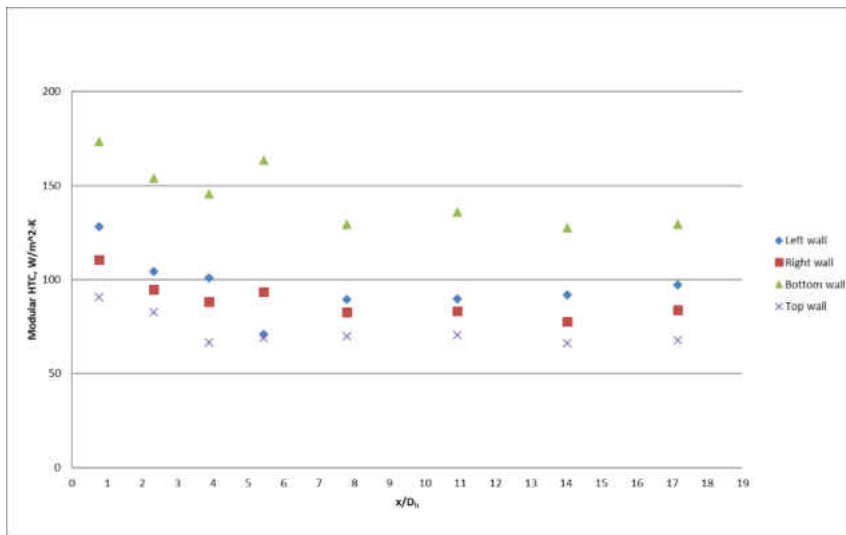


Figure 13 Calculated Modular Heat Transfer Coefficient at Re=70,000

Since each wall was of a single aluminum plate, lateral conduction had to be calculated to understand how it affects the energy balance. The lateral conduction in the aluminum plates was determined by taking the average recorded temperature from neighboring modules on a wall, and calculate the conduction heat transfer driven by the temperature gradient these two averaged temperatures create between the two modules.

$$Q_{lat.cond.} = -A_{cs}k_{Al}(T_{avg})\frac{T_{m1}-T_{m2}}{1.5D_h} \quad (3.4)$$

where  $A_{cs}$  is the cross section of the aluminum plate,  $k_{Al}$  is the thermal conductivity of the aluminum as a function of the average temperature between the two modules, and  $T_{m1}$  and  $T_{m2}$  are the average temperatures of module 1 and 2, respectively. The distance between the two temperature measurements was  $1.5D_h$  in this experiment. The lateral conduction through the aluminum plates was found negligible, less than 1%, between each module because the temperature difference between each module was very small in the isothermal wall testing.

The module-averaged Nusselt number, the ratio of convective heat transfer to conductive heat transfer, was calculated from the heat transfer coefficient at each wall module, the hydraulic diameter of the channel as the length scale, and the temperature dependent thermal conductivity of the air. Module-averaged Nusselt numbers for each wall were determined for this experiment.

$$Nu_{D_h} = \frac{\bar{h}_x D_h}{k_{air}(T)} \quad (3.5)$$



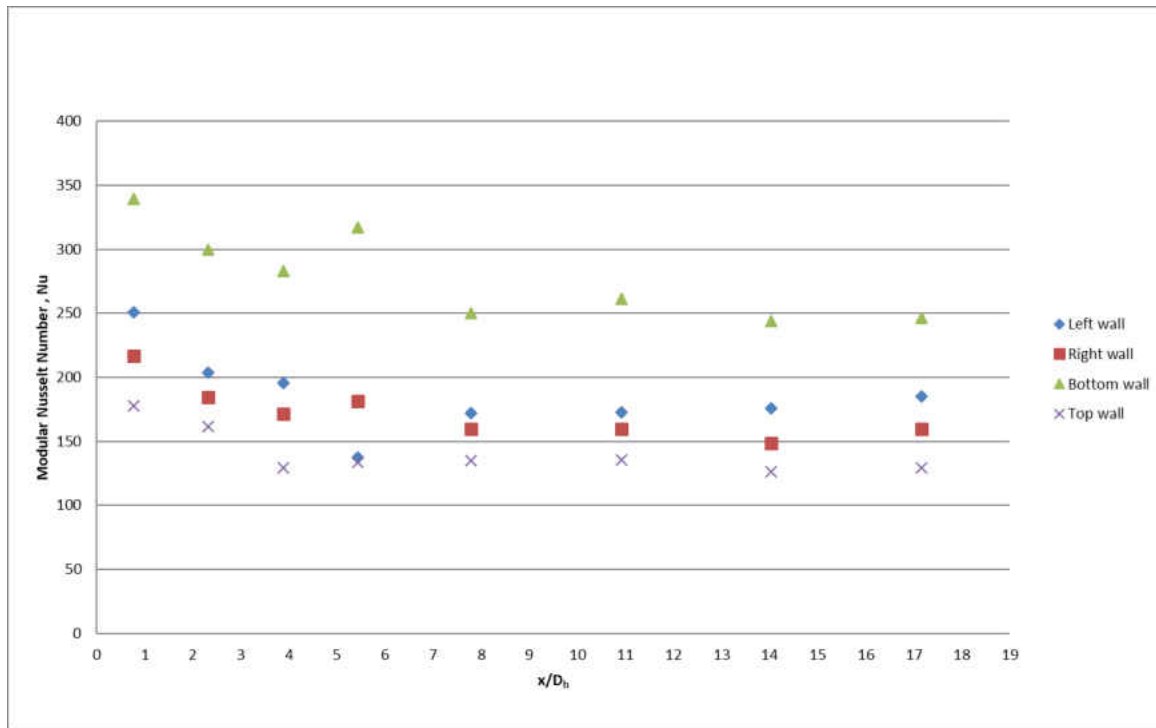


Figure 14 Calculated Modular-Averaged Nusselt Number at Re = 70,000

In internal flows, when a constant temperature surface is the heat source and the air is the cooling medium, the heat transfer due to convection is greatest at the entrance of the channel because of the high temperature gradient between the air and the hot surface. As the flow moves down the channel, it retains the heat it picked up from the walls due to its low specific heat capacity, increasing its temperature. If the surface stays a constant temperature and the air is picking up less and less energy from the walls as the temperature difference between the wall and air gets smaller and smaller. Consequently, the heat input to the plates from the heaters are forced to be smaller and smaller as well for constant wall temperature cases. As the temperature difference decreases, and the heat input decrease, there comes a point where the two drops become proportional, and thus the ratio of the two, the heat transfer coefficient, becomes constant. It is at this point where

the flow becomes fully thermally developed. Since Nusselt number is proportional to the heat transfer coefficient, it also follows the same behavior.

If the fully thermally developed Nusselt number is only considered, the wall-averaged Nusselt number can be calculated. Mentioned previously, this Nusselt number will not change after the point of full development. If the channel was very long, the average Nusselt number across a wall would average to this value because the developing region would be comparatively small and would not have much effect on the mean. If Prandtl number, the ratio of momentum diffusivity to thermal diffusivity, is considered constant for air, the wall-averaged Nusselt number will only be a function of Reynolds number. An augmentation of the wall-averaged Nusselt number at each wall module can be expressed by the ratio of the rig's Nusselt number over the Nusselt number obtained through Dittus-Boelter's smooth-wall correlation.

$$Nu_o = 0.023Re^{0.8}Pr^{0.4} \quad (Dittus - Boelter) \quad (3.6)$$

$$\frac{Nu}{Nu_o} = \frac{\frac{\bar{h}_x(Re)D_h}{k_{air}}}{0.023Re^{0.8}Pr^{0.4}} \quad (3.7)$$

The Dittus-Boelter correlation is only valid for Reynolds numbers  $> 10,000$ ,  $0.6 < Pr < 160$ , and  $L/D_h > 10$ . The lowest Reynolds number studied in this experiment was 20,000,  $Pr \sim 0.7$ , and  $L/D_h \sim 23$ . Under these rig conditions, the Dittus-Boelter correlation was valid.

### 3.2 Friction Analysis

The purpose for this test is to figure out what friction cost results from reaching a certain Reynolds number in the channel. In real applications, this friction the ribs create is associated with the

pressure cost required to cool the first couple of stages in the turbine section in a gas turbine engine. The pressure originates from a bleed valve near the final stages of the compressor section. Any airflow removed from the compressor exit will be wasted work potential. However, for the turbine airfoils' survival at the combustor exit, this cost of compressor work potential output is necessary. Without this mode of internal cooling, the airfoils would surely melt in a short amount of time, destroying the engine. Given that the friction is proportional to compressor work potential loss, it would be right to seek the least amount of friction possible that would be the least detriment to the engine's overall performance. Therefore, an optimization is in order. In the earlier chapter, the heat transfer capabilities of the ribs were discovered. This enhanced heat transfer is largely attributed to the turbulent mixing of the ribs. Unfortunately, the turbulent mixing heightens the frictional losses. Smooth ducts have much less friction, but also much less heat transfer than ribbed-wall channels.

In this chapter, the approach on how, and which friction factor definition used will be explained. Assumptions will be elaborated, and a brief reference back to the rig design will supplement the approach. As in the previous chapter, an augmentation value referenced to a perfectly smooth pipe wall, the Blasius correlation, will emphasize the friction impact a single ribbed-wall channel will cause.

### 3.2.1 Friction Factor Testing

The friction factor of the rig was calculated by using the Fanning equation, which is a quarter of the Darcy-Weisbach friction. A total pressure drop was not measured for the friction factor, but rather the static pressure drop along the rig through several pressure taps. Using the mass flow rate

equation, and understanding that mass flow rate through the rig will be constant, a negligible change in density means a negligible change in velocity in a constant cross section duct. For an incompressible flow at low Mach number along a streamline, the change in dynamic pressure should be negligible. Thus, by Bernoulli's equation, the change in total pressure drop should be directly proportional to the change in rig static pressure. Although negligible as just described, the average velocity was considered for the friction factor calculation by the slight change in density that occurred in the channel through turbulent dissipation heating. With the spacing of the pressure taps known, a pressure drop slope can be calculated

$$f_{Fanning} = \frac{1}{4} f_{Darcy} = \frac{1}{4} \frac{\frac{\partial P}{\partial x} D_h}{\frac{1}{2} \rho_{avg} u_{avg}^2} = \frac{\frac{\partial P}{\partial x} D_h}{2 \rho_{avg} u_{avg}^2} \quad (3.8)$$

where  $\rho_{avg}$  is the average density,  $\partial P / \partial x$  is the pressure drop slope, and  $u_{avg}$  is the average velocity determined by the mass flowrate and the average density.

A rough indication that the flow is fully developed through the acrylic inlet can be observed through the straightness of the pressure drop curves measured by the Scanivalve. If the flow is fully developed the velocity profiles should remain constant. The same goes for the drop in static pressure.

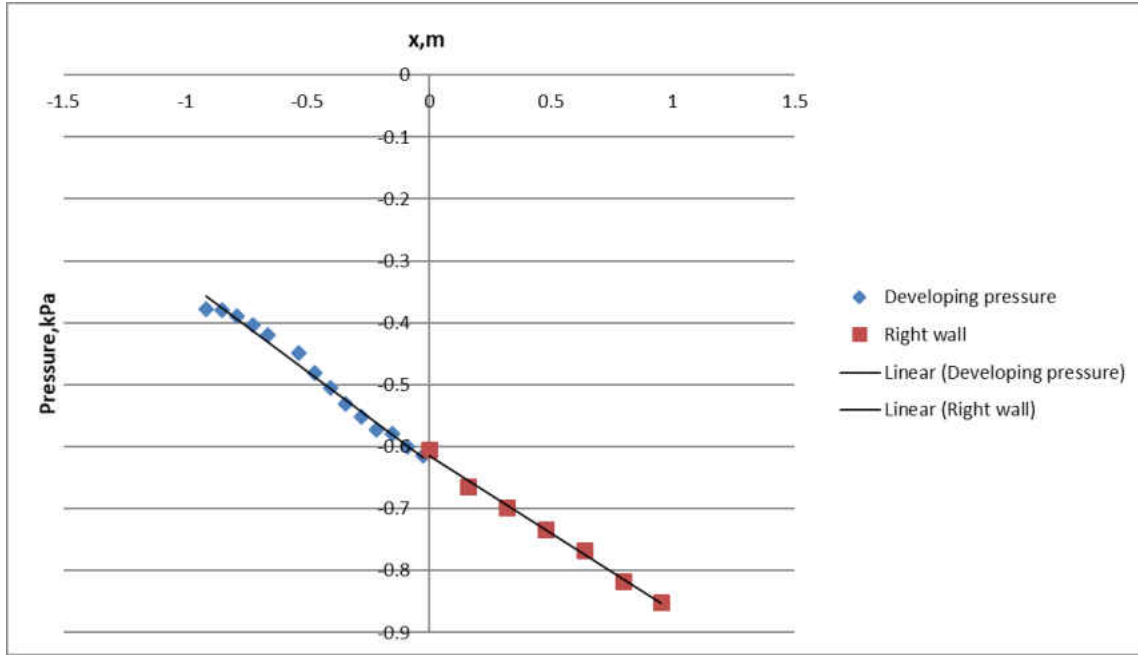


Figure 15 Pressure Drop Across Non-Heated Rig at  $Re = 70,000$

Like the Nusselt number augmentation, a friction factor augmentation was also formed by the ratio of the rig's friction factor to the smooth-wall Blasius friction factor correlation

$$f_o = \frac{0.0791}{Re^{0.25}} \quad (Blasius) \quad (3.9)$$

which is valid for  $2100 < Re < 100,000$ .

### 3.3 Hot-Wire Analysis

The purpose of this study was to determine how the flow of air changes over a specific rib geometry at a low Reynolds number range. It was of particular interest to investigate how the separation and reattachment points move, and evolve, as Reynolds number changes from low to moderate values. Because the sensor is only a single wire, the direction of the velocity cannot be determined, only the magnitude. Calculations of Reynold's shear stress, and turbulent kinetic energy (TKE) cannot

be accurately measured. Only time-averaged velocity profiles, and turbulence intensities will be presented in this study.

### 3.3.1 Understanding the Bridge

Mechanically, a constant temperature hot-wire anemometer is a Wheatstone bridge where the bridge error, the voltage difference between the left and right 'arms' of the bridge top is fed to a shaping servo amplifier's non-inverting (+) pin and inverting (-) pin as a differential input. There are two types of bridge sets available in the DANTEC StreamLine Pro CTA: a 1:20 bridge, and a 1:1 bridge. The set resistors located on the bridge top are each 20ohms in the 1:1 arrangement. However, the set resistor located on the right arm is adjustable to  $20 \times 20 \Omega$  ( $400 \Omega$ ) in the 1:20 arrangement (Figure 16).

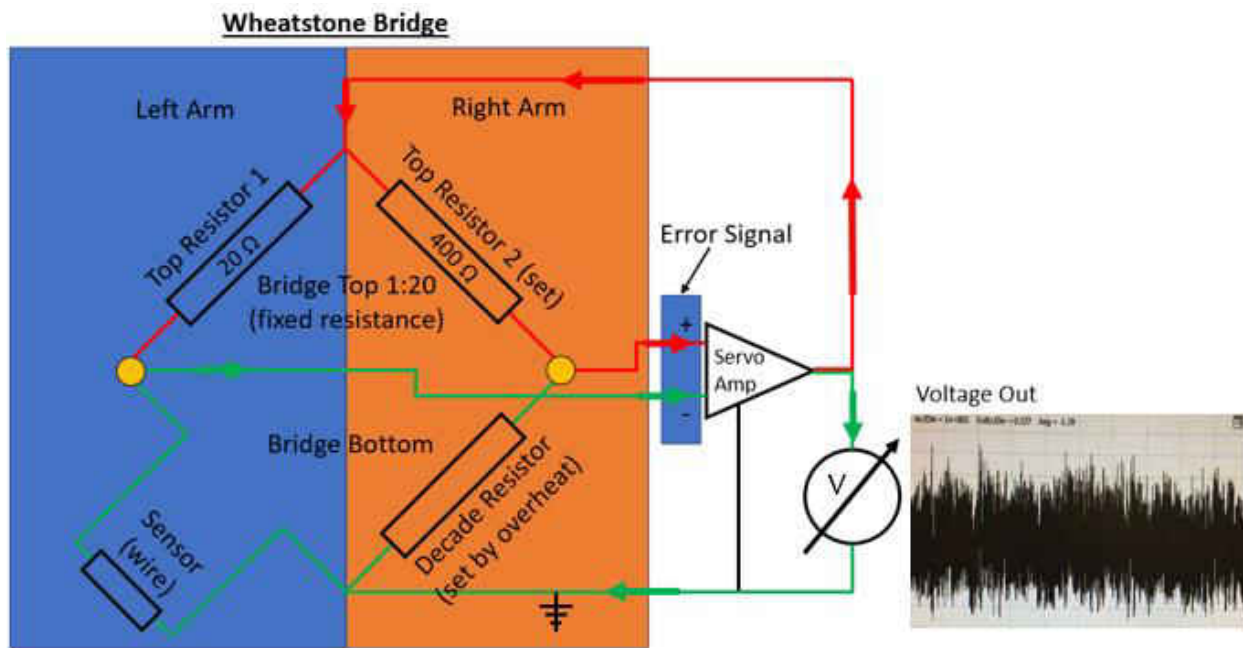


Figure 16 Anatomy of a CTA Wheatstone Bridge Amplifier Loop

For this experiment, the 1:20 bridge was selected (1) because the 1:1 setting is only used for very high frequency responses  $\sim 1\text{MHz}$ , and (2) the 1:1 settings requires an external overheat resistor put into the sensor's BNC cable to compensate the bridge impedance, which was not included in the CTA package. As the sensor resistance rises, the voltage input to the non-inverting (+) pin of the amplifier becomes less than the voltage input to the inverting (-) pin of the amplifier since the resistance of the voltage divider circuit of the right arm is fixed by the high precision decade resistor. The inverse response occurs if the sensor resistance drops. This is how the feedback loop of the amplifier works to bring the error voltage back to zero, where the voltage drop across each of the two set resistors in the 1:20 bridge become equal.

### 3.3.2 Sensor Heat Transfer Theory

The sensor itself operates under the simple principle of a heated infinitely long pin-fin from two sides cooled by convective air, Figure 17. The objective of the anemometer is to keep the sensor at a constant resistance by controlling the current through the servo amplifier so that the sensor temperature, and therefore resistance, remains constant under varying convective flow velocities.

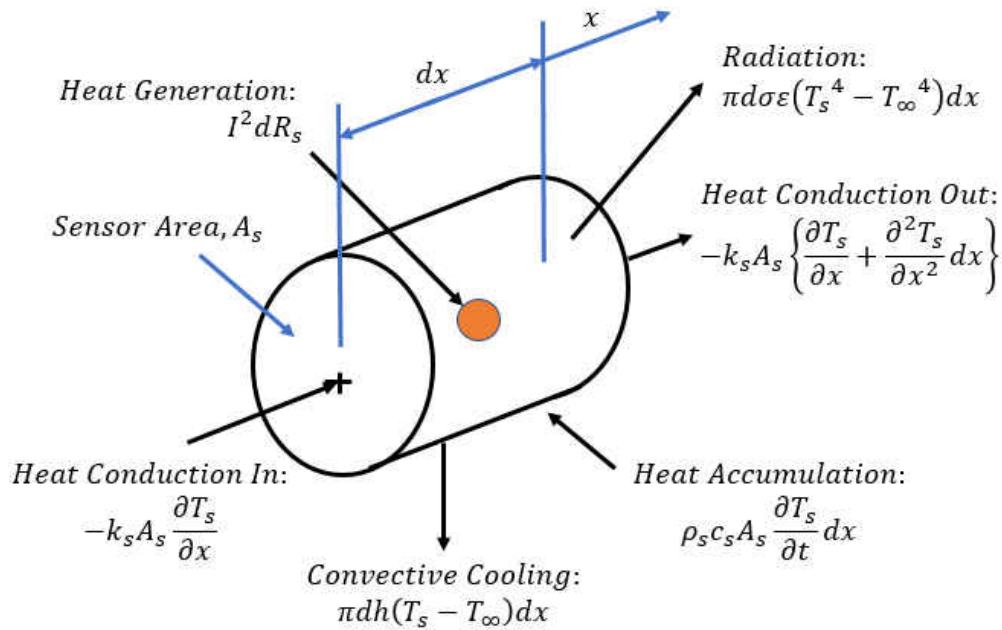


Figure 17 Energy Balance of a Hot-Wire Sensor

The equation below describes the energy balance that occurs in a control volume around the sensor with convective flow.

$$k_s A_s \frac{\partial^2 T_s}{\partial x^2} + I^2 dR_s - \pi Dh(T_s - T_\infty)dx - \pi D\sigma\epsilon(T_s^4 - T_\infty^4)dx = \rho_s c_s A_s \frac{\partial T_s}{\partial t} dx \quad (3.10)$$

Because the sensor operates under this heat transfer principle, there are regions near the prongs of the sensor where the temperature is colder than its operating temperature. The aspect ratio ( $2l_s/d_s$ ), where  $l_s$  is the sensor length and  $d_s$  is the diameter of the sensor, needs to be very large to minimize this heat loss (Figure 18).



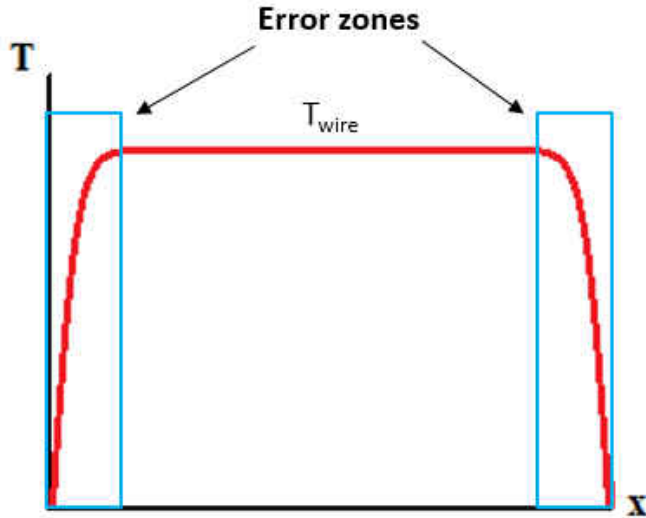


Figure 18 Sensor Temperature Profile – Error Zones

The DANTEC 55P11 Single-sensor Miniature Wire Probe has a sensor length of 1.25mm, and a sensor diameter of 5 $\mu$ m. This yields an aspect ratio of 500. Champagne et al [ 27 ] recommends an aspect ratio greater than 200 to make the heat loss error negligible.

In the region of the wire where the difference in temperature of the sensor becomes infinitesimally small, the effective length, the heat conduction terms of the above energy balance become negligible. Assuming the measurements are taken during a time where the sensor stabilizes, at or below the cut-off frequency, temporal dependencies can be considered negligible. Lastly, if radiation is neglected, the energy balance then becomes:

$$I^2 R_s = \pi D L_{eff} h (T_s - T_\infty) = \pi D L_{eff} \left( \frac{Nuk}{D} \right) (T_s - T_\infty) \quad (3.11)$$

It can be shown that Nusselt number, the ratio of convective heat transfer vs conductive, is a dependent on many non-dimensional parameters: Reynolds number, Prandtl number, Knudsen number, several geometric factors, etc. However, in 1914, L.V. King discovered a fundamental

relation between the heat transfer from an infinite cylinder and Reynold's number with his thermal dispersion mass flowmeter, which he later named "hot-wire anemometer". This relationship, shown below, was published as King's Law.

$$Nu = A_1 + B_1 Re^n = A_2 + B_2 U^n \quad (3.12)$$

Therefore, the expression for the reduced energy balance equation can be equated with King's law with the minor adjustment to the energy balance equation by adding a length scale (sensor length), and fluid thermal conductivity.

$$I^2 R_s = \pi D L_{eff} \left( \frac{Nu k}{D} \right) (T_s - T_\infty) = (A + B U^n) (T_s - T_\infty) = E^2 \quad (3.13)$$

### 3.3.3 Limitations

Before the servo-amplifier electronics, hot-wire studies relied on the thermal response, purely on the sensor itself.

$$\left( \frac{mc}{hA} \right) \frac{dT}{dt} + T = T_\infty \quad \rightarrow \quad T(t) = T_\infty \left( 1 - e^{-t/\left(\frac{mc}{hA}\right)} \right) = \frac{T(t) - T_\infty}{T_0 - T_\infty} = e^{-t/\left(\frac{mc}{hA}\right)} \quad (3.14)$$

This first-order response only resolved frequencies in several hundred hertz, where the time constant is  $\frac{mc}{hA}$ , Figure 19.

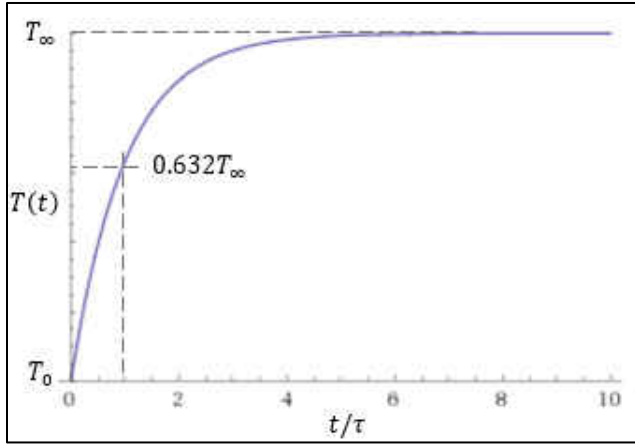


Figure 19 First-order Response to Temperature Step Change

When more advance anemometers were built in the 70's, the frequency resolution increased by three orders of magnitude to several hundred kilohertz thanks to the servo amplifier loop.

Hot-wires have been designed to give very accurate flow data up to several hundred meters per second, but there is a lower velocity limit at which the convective flow over the sensor is overcome by flow created by the heated sensor itself through natural convection. The sensor is typically heated to about 240°C, and when convective flow is so low, natural convection takes over, and the flow velocity cannot be accurately resolved. DANTEC has estimated the influence of natural convection holds for their probes up until a velocity of 0.20m/s. They also specify a maximum velocity of 500m/s for wire structural reasons.

Another limitation comes from the steady-state assumption made earlier in the energy balance equation (3.10). This limitation is the cut-off frequency, the smallest time-scale the sensor can observe. The DANTEC StreamLine Pro CTA is equipped with a square-wave generator that is used to test its overall system response limitations. The CTA sends a square-wave signal through the sensor while exposed to an expected maximum flow velocity. The signal throws the sensor off

balance, and the time it takes for the servo-amplifier loop to balance out the error in the bridge gives the CTA's overall response time lag, Figure 20.

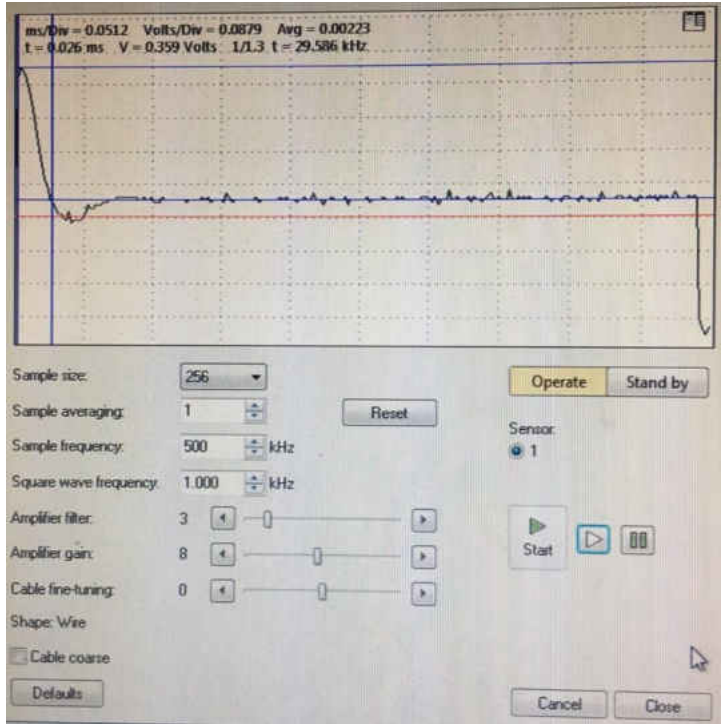


Figure 20 Square-Wave Response to DANTEC Sensor

This response lag can then be converted to a frequency by the equation below for turbulent flows DANTEC provides based on the work of Freymuth et al. [ 29 ]. The  $\Delta t$  is determined by the time it takes for the bridge to recover from 97% of its peak voltage disturbance “height” from the square-wave generated within the anemometer.

$$f_{cut-off} = \frac{1}{1.3\Delta t} \quad (3.15)$$

### 3.3.4 Temperature Corrections

Because the sensor must maintain a constant temperature to work, there are several environmental factors that can make the measurement less accurate. Changes in local temperature can impact the accuracy of the sensor. DANTEC warns that each unaccounted 1°C change in temperature can induce a 2% error in the velocity measurement. StreamLine Pro has a few options to help avoid this issue. The first option is to maintain a fixed decade resistance and overheat ratio, a non-dimensional measure the increase in temperature with sensor resistance, but correct the voltage output with a modification of an equation proposed by Brunn et al. [ 28 ], shown below,

$$E_{s,ref} = E_s \left[ \frac{T_s - T_{ref}}{T_s - T_{amb}} \right]^{1/2(1 \pm m)} \quad (3.16)$$

where  $m$  is a thermal loading factor (typically 0.2 for air on wire sensors with an overheat ratio of 0.8).  $E_s$  is the measured voltage,  $T_s$  is the temperature of the sensor,  $T_{ref}$  is the temperature of the fluid at the time the measurement was taken, and  $T_{amb}$  is the ambient temperature that was recorded just prior to calibrating, or testing. For this process, a reference temperature must be taken before each measurement with the use of a temperature probe near the wire. Since turbulence temperature fluctuations were not an objective in this experiment, primarily because this is experiment is purely aerodynamic, and has no noticeable thermal gradients, a probe would not be needed direct by the sensor to disrupt the flow. However, a temperature probe was not available for the experiment, so corrections by other means had to be taken.

The second option, the option that does not require a reference temperature adjustment is the automatic overheat adjust operation. In this scenario, the overheat ratio is fixed, and the decade

resistance is adjusted to maintain the overheat resistance at a constant value. Therefore, there was need to retake a reference temperature.

### 3.3.5 Filtering

After obtaining the raw analog signal, the CTA puts the signal through conditioning. While taking measurements with the CTA, the Butterworth lowpass filter StreamLine Pro possesses should be set to the cut-off frequency as closely as possible. The cut-off frequency will be treated as the Nyquist frequency, the highest resolvable frequency in a signal. Through the StreamWare software, the user can define the square-wave frequency, and is required to adjusted the amplifier gain and filter settings up until the point where the response starts to ‘ring,’ indicating that the bridge has become unstable and cannot recover. The highest flow velocity expected in this experiment was 100m/s, and after tuning the amplifier, the square-wave test yielded a 126kHz frequency limit. The lowpass filter was thus set to 130kHz. The Nyquist equation states that the sampling frequency should be at least twice that of the highest resolvable frequency in a signal, so the sampling frequency was set to 262kHz for hot-wire measurements in this experiment.

### 3.3.6 Sample Convergence

In order ensure that a stochastic signal will yield a constant mean and standard deviation, the duration of the sampling must be determined. Sample convergence analysis tracks the mean and standard deviation of a signal in time from  $t=0$  to  $t=T$  (the duration of the signal). How it works is that for every sample collected, it will be ‘added’ into the cumulated mean and standard deviation. Convergence is reach when the ‘addition’ of the next point fails to change the overall mean and

standard deviation. Since the standard deviation is a higher order equation than the mean, it will take longer than the mean to converge. Shown below are partial expansions of the sequences for mean and standard deviation convergence.

Mean Convergence Sequence:

$$\mu_1 = x_0, \mu_2 = \frac{x_0+x_1}{2}, \mu_3 = \frac{x_0+x_1+x_2}{3}, \mu_4 = \frac{x_0+x_1+x_2+x_3}{4}, \dots \quad (3.17)$$

Standard Deviation Convergence Sequence:

$$\sigma_1 = 0, \sigma_2 = \sqrt{\frac{1}{2} \sum_{i=1}^2 (x_i - \mu_1)^2}, \sigma_3 = \sqrt{\frac{1}{3} \sum_{i=1}^3 (x_i - \mu_2)^2}, \sigma_4 = \sqrt{\frac{1}{4} \sum_{i=1}^4 (x_i - \mu_3)^2}, \dots \quad (3.18)$$

The convergence test was conducted in the most turbulent region found at the highest Reynolds number tested, 50,000. The most turbulent region was found to be a few locations downstream of the first rib where the shear layer coming from the rib due to flow separation interacts with the recirculation zone just behind the rib's trailing edge. This location was chosen because it is where the signal will be least willing to converge due to its high turbulence. The convergence of the mean for the above sampling frequency was about 1 second worth of signal (Figure 21), and the standard deviation of the signal converged after about 1.5 seconds (Figure 22).

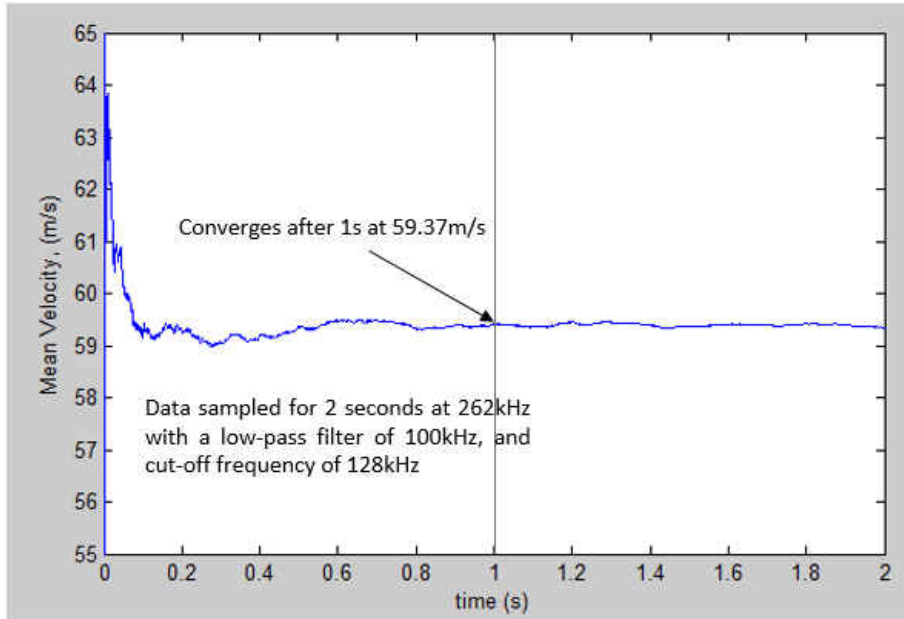


Figure 21 Convergence of the Sample Mean

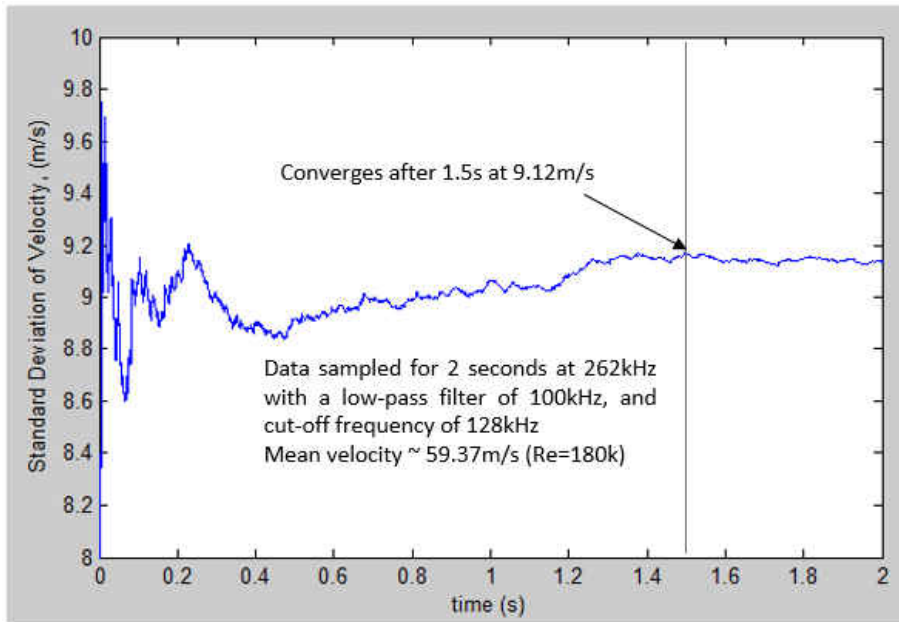


Figure 22 Convergence of the Sample Standard Deviation



To ensure the signal will converge for any Reynolds number, the chosen sampling duration was 4 seconds, a little more than twice the convergence time of the standard deviation. This gave a sample count of just over a million data points.

### 3.3.7 Calibration

A TSI™ 1127 manual velocity calibrator's three nozzle sets were used to calibrate the sensor for various velocity ranges. Contrary to common hot-wire calibration practices, a 4<sup>th</sup>-order polynomial curve fit was used to correlate the voltage the anemometer was outputting and the velocity of the air from the nozzle set. Since the 16-bit A/D board's voltage input range of 10V, -5 to +5 volts, the calibration voltage output was offset and amplified to -5 to +5 volts, or however close to the A/D converter's limit the CTA would allow without overshooting. When converting the analog signal to a digital signal, increasing the usage of the A/D board's range will maximize the number of 'bins' the analog voltage can be placed in during the digitization process. 20 equally-spaced points are taken within the voltage range the CTA's amplifier gain will allow for a given calibration.

To ensure the sensor is accurate while taking measurements, a calibration of the sensor was done before, and after each test to account for any voltage drift caused by contaminate accumulation on the sensor during testing, and internal errors that might occur when the CTA is switched between Standby and Operate mode.

Prior to introducing flow to the sensor, and voltage offset and amplification, an initial (0m/s) voltage measurement is taken for later use when creating King's Law curve fits.

The velocity of the flow at the nozzle exit was calculated by using high-order polynomial correlations TSI provides with their calibrator units that link the nozzle set's venturi pressure differential to nozzle exit velocity. With the velocity known at each point as well as the sensor's voltage, fitting a correlation between the two was possible.

### 3.3.8 Uncertainty Considerations

DANTEC provides a list of velocity uncertainty equations used to calculate errors from a multitude of physical phenomena including local temperature variation effects, ambient pressure fluctuations, and density changes due to temperature and pressure. These errors as well as systematic errors such as sensor yaw angle and curve-fit biases were considered during the analysis and for all Reynolds number case, most of the errors amounted to about 5-6% of the velocity measurement. DANTEC gave a rough estimate of 3% on the total uncertainty of the velocity measurement. Given that their estimate was based on the use of their automated calibrator and that the curve-fit error was responsible for most of the uncertainty, 5% with the use of a manual calibrator is reasonable. The equations for these uncertainties are listed in the Appendix D.

## CHAPTER 4: RESULTS AND DISCUSSION

### 4.1 Heat Transfer Analysis Results

The heat transfer experiments were tested at seven Reynolds numbers ranging from 25,000 to 125,000. The module-averaged Nusselt distribution (Figure 23) showed that the highest heat transfer coefficient occurs at the entrance of the test section due to thermal development as the flow just begins to be heated. At the entrance, the largest temperature gradient between the plate and fluid temperature exists.

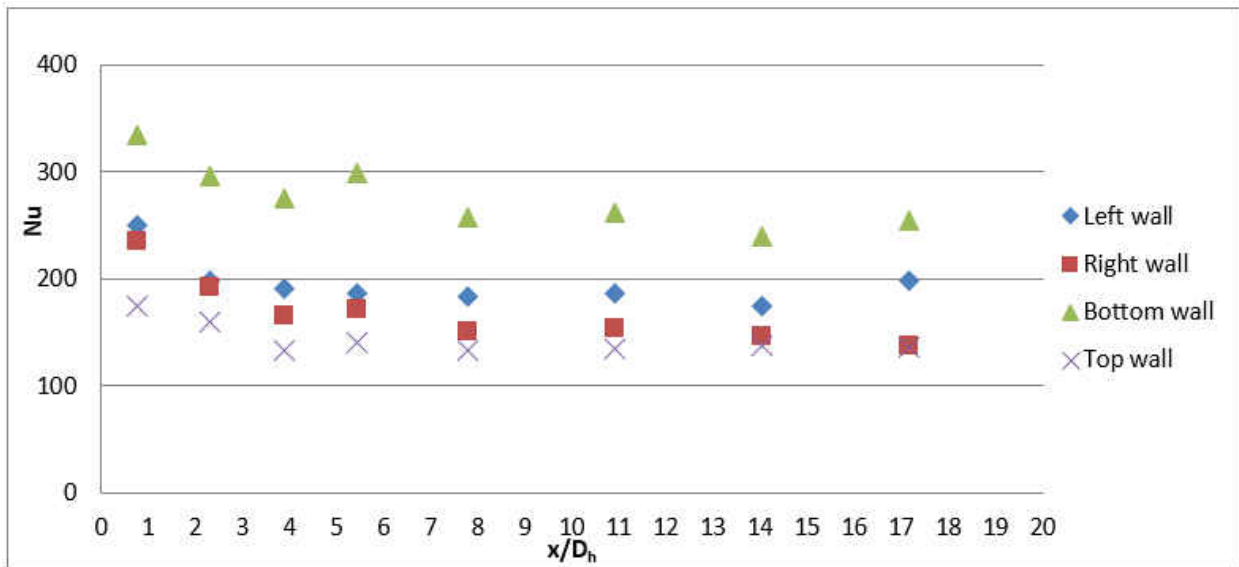


Figure 23 Modular Nusselt Number distribution,  $Re = 70,000$

Tests conducted by Ahmed et al. [ 1 ] for the two ribbed-wall case conclude that the heat transfer coefficient became constant after around eight hydraulic diameters in all  $Re$  cases. Figure 23 shows that the same holds true for the single ribbed wall case.  $x/D_h$  begins at zero at the test section

entrance in this figure. Since the bulk air temperature increases along the test section, local  $Re$  decreases along the streamwise direction.

For the remainder of this paper, averaged wall-based  $Nu$  values, calculated by fully turbulent heat transfer coefficients will be discussed. These Nusselt values will be plotted against test section averaged  $Re$  calculated by averaged test section bulk temperature properties, and mass flowrate derived average flow velocity. The averaged wall-based  $Nu$  was decomposed into three curves: averaged smooth top walls, averaged smooth left and right walls, and averaged ribbed bottom wall for each  $Re$ , and can be seen in Figure 24. It is seen that the bottom ribbed wall had the most effective heat transfer, and that the top smooth wall had the least effectiveness. The smooth side walls had a higher  $Nu$  than the top walls due to turbulence which is generated by the bottom ribbed wall, weakening toward the top wall.

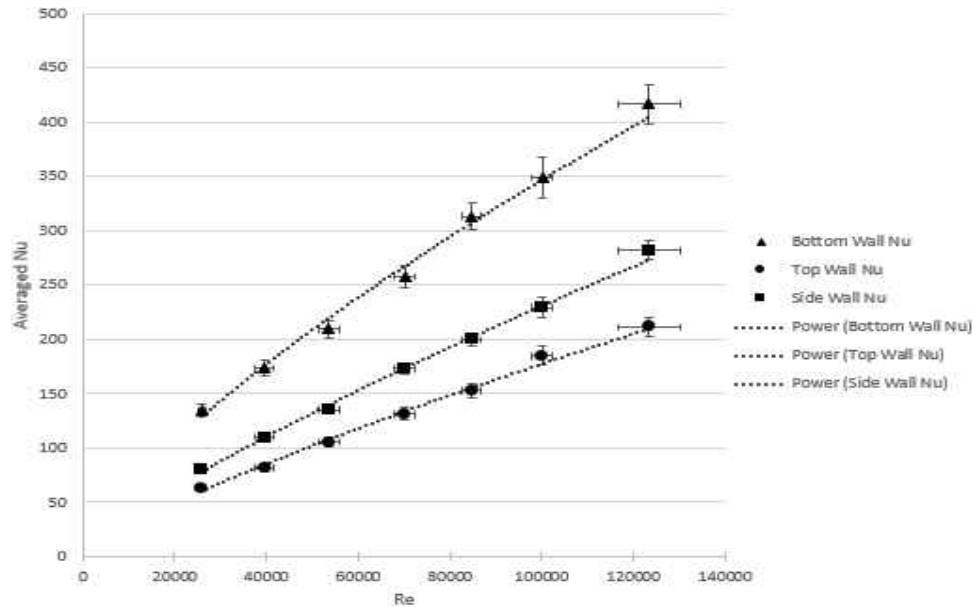


Figure 24 Wall-Averaged Nusselt number at various  $Re$  ranging from 25,000 to 125,000

In Ahmed et al.'s two ribbed wall study [ 1 ], the top and bottom ribbed walls had nearly identical Nu values since boundary conditions in the channel were about the same, and thus could be appropriately averaged together to get an averaged rough wall Nu for both walls. Figure 25 presents the channel-averaged heat transfer augmentation ( $Nu/Nu_0$ ) at various Re for both one ribbed wall and two ribbed wall cases.

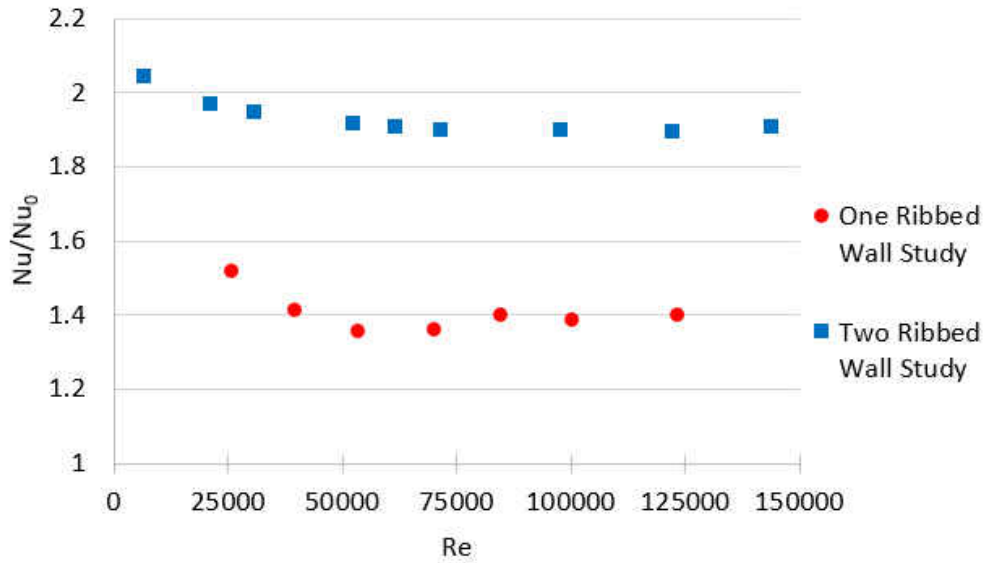


Figure 25 Channel-Averaged Nusselt Augmentation for Re ranging from 25,000 to 125,000

The channel-averaged Nusselt numbers were normalized with a smooth channel  $Nu_0$  value, based on Dittus Boelter correlations for smooth circular tubes, just as Han et al. [ 3 ] [ 5 ] [ 6 ], and Ahmed et al. [ 1 ] had done, to properly compare results. It should be noted that the Dittus Boelter equation is valid for  $0.6 < Pr < 160$ ,  $L/D > 10$ , and  $Re_D > 10,000$  for turbulent flows. All tests in this experiment were conducted within this range.

$$Nu_{0Dh} = 0.023Re_{Dh}^{0.8}Pr^{0.4} \text{ (Dittus Boelter)} \quad (4.19)$$

The results show a nearly constant augmentation of around 1.4 for all Re after 90,000 for the one-wall case. The two-wall case revealed an augmentation of about 1.3 to 1.5 times higher than the one wall case as it settles at around 1.9 for Re greater than 50,000 [ 1 ]. This was to be expected since the two-wall case had much more turbulent mixing than the single-wall channel.

#### 4.2 Friction Factor Analysis Results

To guarantee the accuracy of the friction testing, an extensive investigation was conducted with several data points at repeated Reynolds numbers. The friction calculation is affected by channel geometry, flow rate measurements, pressure measurements. Error in any of these measurements can lead to erroneous friction results. Because of this, all error sources in these measurements were checked rigorously. Flow rate measurement was confirmed by checking venturi calibrations and recalibrating when needed. Flow leakage tests through the inlet, test section, and downstream plumbing were all checked with incense. Venturi upstream pressure and pressure drop were compared with flow data taken from the heat transfer tests with valid energy balances. Tests were repeated two or three times for each Reynolds number, and plotted to ensure that these measurements matched every time. Any geometric inconsistencies in the alignment of the acrylic inlet and test section were checked, and realigned if needed prior to testing.

From the friction results, one can observe that the friction factors for both the one-wall and Ahmed et al.'s [ 1 ] two-wall cases are relatively high at Reynolds numbers below 22,000. Above Re = 120,000, friction factor holds constant at 0.012 for the single-wall case. Ahmed et al.'s [ 1 ] two ribbed-wall study described an effect where high  $e^+$  values at higher Re show that ribs can no

longer be treated as roughness, but physical obstacles, and friction factor start to increase.

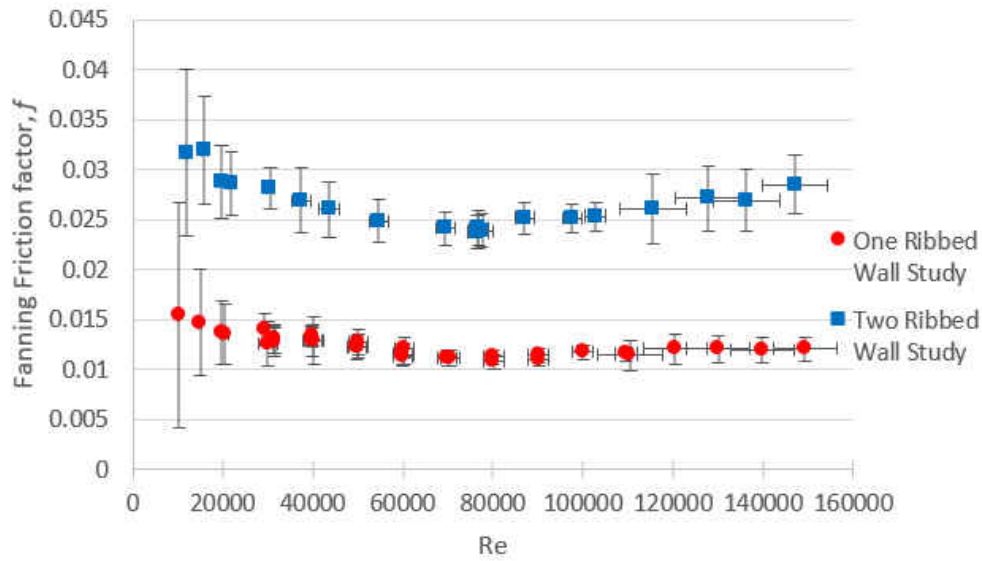


Figure 26 Fanning Friction Factor for Both Single-Wall and Two-Wall Cases

Friction factor augmentation, Fanning friction factor normalized by the Blasius correlation for turbulent flows, at different  $Re$  for the one-wall and two-wall cases are presented in Figure 27.

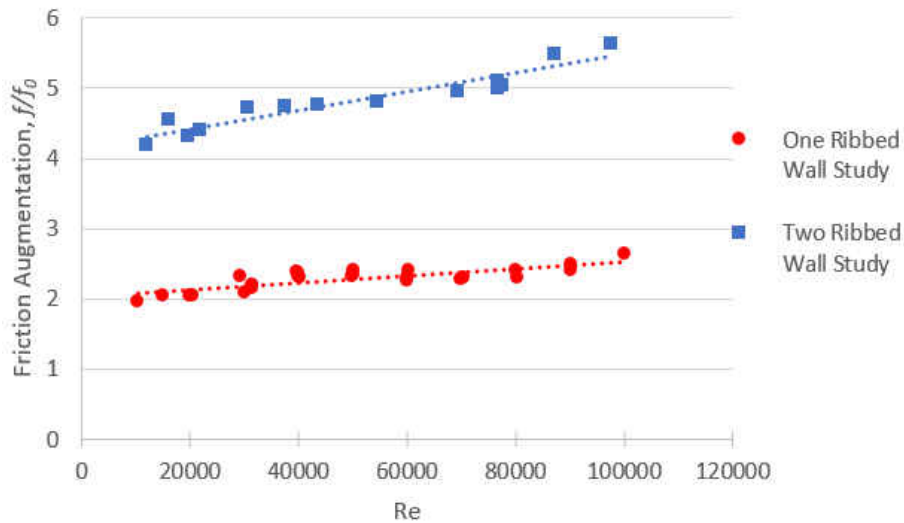


Figure 27 Friction Augmentation for Both Single-Wall and Two-Wall Cases

These curves exhibit an approximately linear relationship with Reynolds Number. The two ribbed-wall study showed about a 2.2 times higher friction augmentation than the one-wall case. The Blasius correlation is only valid between Reynolds numbers of 5,000 to 100,000, so although the friction factor is calculated up to  $Re = 125,000$ , the Augmentation is only valid when the Blasius correlation is valid. Once again, the Blasius correlation is used in this study because both Han et al. [ 3 ] [ 5 ] [ 6 ], and Ahmed et al. [ 1 ] determined their augmentations with this correlation.

#### 4.3 Thermal Performance Analysis Results

Heat transfer tests have been conducted for seven  $Re$  in the range of 25,000 to 125,000 for the one-wall case. The pressure drop/friction experiments were conducted at a wider range. A linear curve fit, generated from the friction augmentation against  $Re$ , allowed the prediction of a friction augmentation at the same  $Re$  used during heat transfer testing. This made possible the calculation of the thermal performance. Han et al. [ 22 ] used an equation to define thermal efficiency:

$$\eta = \frac{Nu/Nu_0}{(f/f_0)^{1/3}} \quad ( 4.20 )$$

Ahmed et. al [ 1 ] incorporated the same equation in their validation case of Han's square channel. To make one-to-one comparisons between these results, the same equation was used in this case. Due to lower friction augmentation, the thermal efficiency was higher at low Reynolds numbers. With the increasing  $Re$ , however, the friction augmentation took a toll on the Nusselt augmentation.



Thermal performance decreased until about  $Re = 70,000$ , where it holds constant around unity for the single ribbed-wall case, Figure 28. Within the Reynolds number range studied, the two-wall case continually decreases.

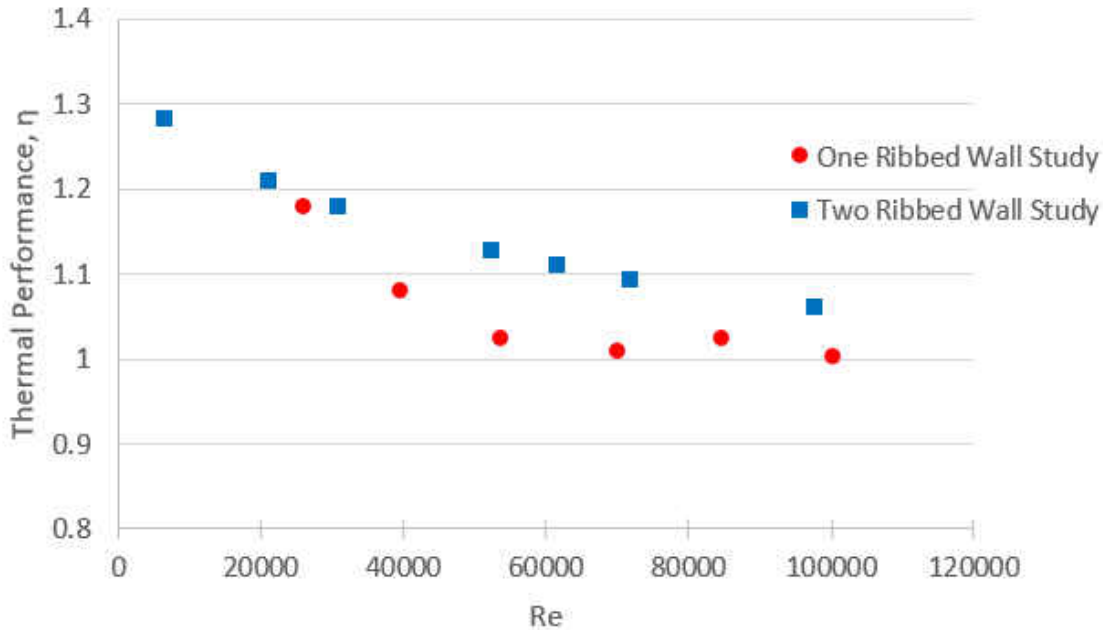


Figure 28 Thermal Performance for Both Single, and Two-Wall Cases

#### 4.4 Heat Transfer and Friction Experimental Uncertainty Results

Uncertainties in the experimental results have been quantified by the methods described by Kline and McClintock [ 25 ] and Moffat [ 26 ]. Refer to Appendix A-D for further detail on the uncertainty analysis. The uncertainty for Reynolds number was estimated to be less than 6% in all cases, Noting that the mass flow rate measurement contributes the most to this uncertainty. The highest uncertainty estimated for Nu was less than 5%. Uncertainties in values such as voltages, resistances, temperatures, and flow rate measurements were the main contributors to Nu uncertainty. Pressure and flow rate measurements contributed to the uncertainty estimation in the

friction factor which was estimated to be less than 12% for  $Re > 20,000$ . The mass flow rate uncertainty took over in friction factor uncertainty for  $Re < 20,000$ . The uncertainty in friction factor jumped to 21%-73% for  $10,000 < Re < 20,000$  due to the minute pressure drop across the rig at this Reynolds number range. Pressure drop uncertainty became comparable to the physical measurement.

#### 4.5 Hot-wire Analysis Results

Single-wire hot-wire anemometry was used to characterize velocity magnitude profiles in great detail, as well as turbulence intensity for Reynolds numbers ranging from 5,000 to 50,000. It was seen that as Reynolds number increased, the reattachment point between two ribs remained relatively stationary while the turbulence intensity receded to the trailing surface of the upstream rib, and dissipated as it traveled. At low Reynolds numbers between 5,000 and 10,000 the velocity and turbulence intensity streamwise profiles seemed to form two distinct flow regions, indicating that the flow over the upstream rib never completely attached between the two ribs.

The following figures will be presented in this fashion:

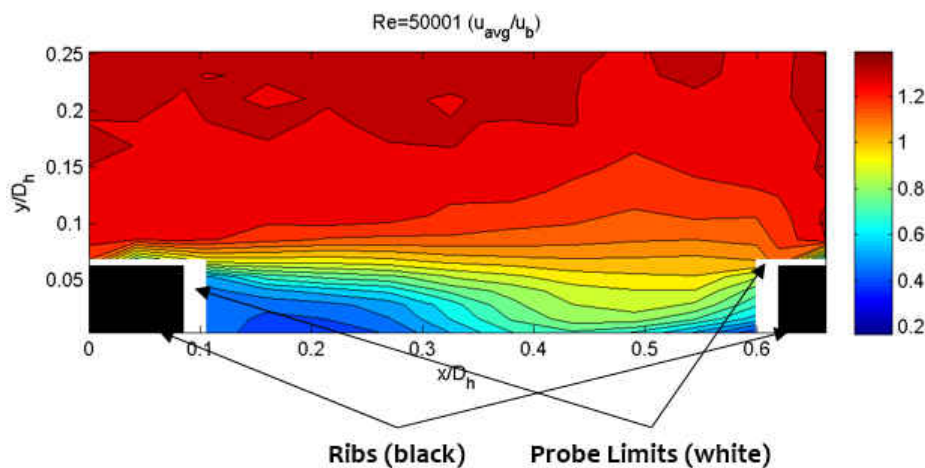


Figure 29 Sample Contour Plot

Figure 29 depicts a normalized velocity contour plot taken at Reynolds number of 50000. The black rectangles seen in the figure represent the physical, to scale, ribs in a midspan cross section of the flow. The white spaces represent the areas the sensor midpoint could not get to because the sensor had to be faced perpendicularly to the flow direction. Unfortunately, this meant that the sensor could not be mounted flush with the ribs, and had to have a  $45^\circ$  angle between them. The thickness of the white spaces aft and forward of the upstream and downstream rib, respectively, indicates the distance between the sensor midpoint and rib edge as they have a  $45^\circ$  misalignment. The contour plots are mapped to each of the intersections in Figure 9. The scale to the right of the contour plots indicates what numeric values are assigned to each color in the plot. To observe the evolution of the flow, the scales are kept the same between all tested Reynolds numbers and measurement type.

To make sure the hot-wire measurement was stable and repeatable, a repeatability test was conducted at  $Re = 50000$ . Shown below is a contour of turbulence intensity and its associated uncertainty percentage for this Reynolds number.

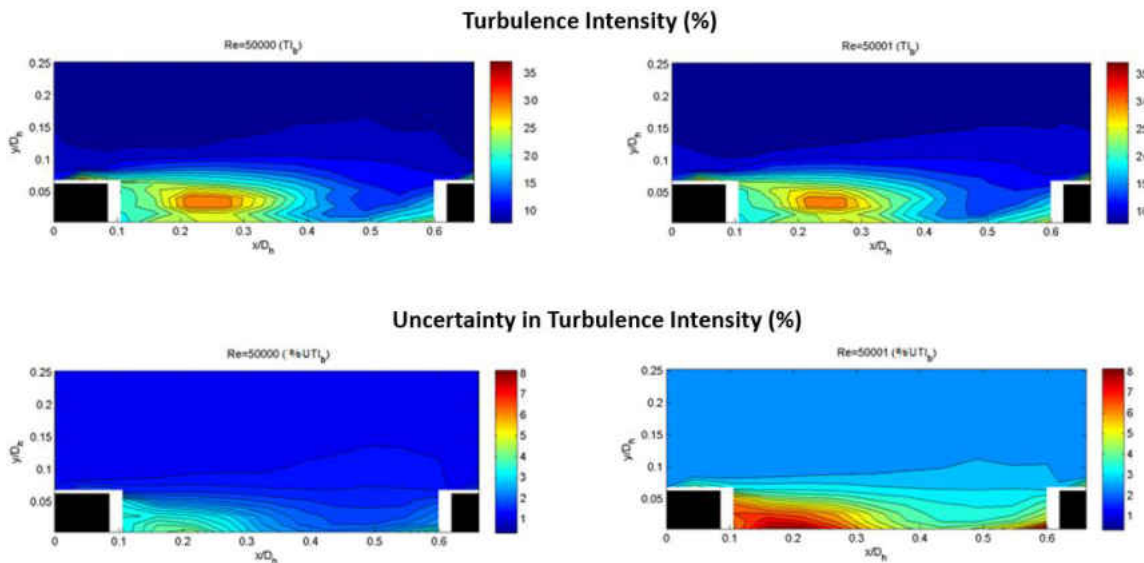


Figure 30  $Re = 50,000$  TI Repeatability Test

In Figure 30, the two top plots are nearly identical, indicating that the testing is repeatable. However, the uncertainty plots beneath are quite different in magnitude. This was due to the systematic uncertainty of the velocity calibration curve fit error. Further details on the uncertainty is shown in Appendix D.

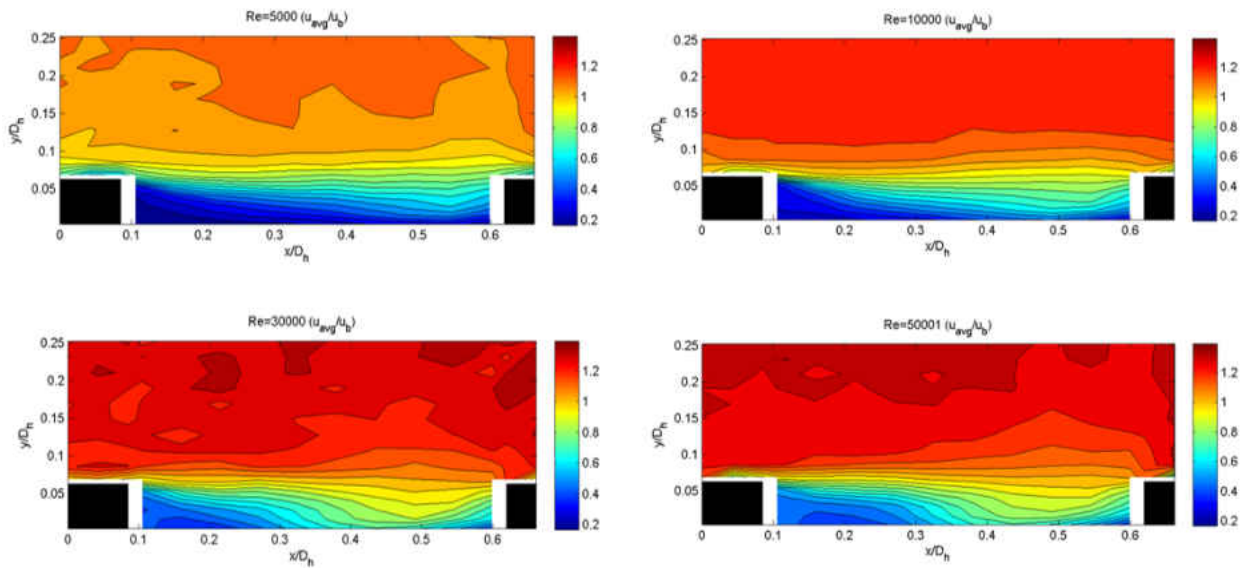


Figure 31 Local Velocity Normalized by the Channel Bulk Velocity

In Figure 31, it is seen that the scaled velocity increased dramatically in the free stream, above the rib until  $Re = 30,000$ , where the freestream velocities between  $Re = 30,000$  and  $50,000$  appear to be about the same. Another observation can be made near the wall at  $x/D_h \sim 0.48$  to  $0.55$ . This is where the reattachment point was located in the Reynolds number range tested. Although not clear if the flow is reattaching at  $Re = 5,000$  at  $x/D_h = 0.55$ , it can be seen in the other Reynolds numbers tested. The reattachment point location seems to have a weak, but existent, correlation with flow increase. As  $Re$  increase, the reattachment point slowly moves back toward the aft of the upstream

rib. Further Reynolds number data need to be obtained to determine if the position stops after  $Re = 50,000$  because it does not appear to change between this flow rate, and that of  $Re = 30,000$ .

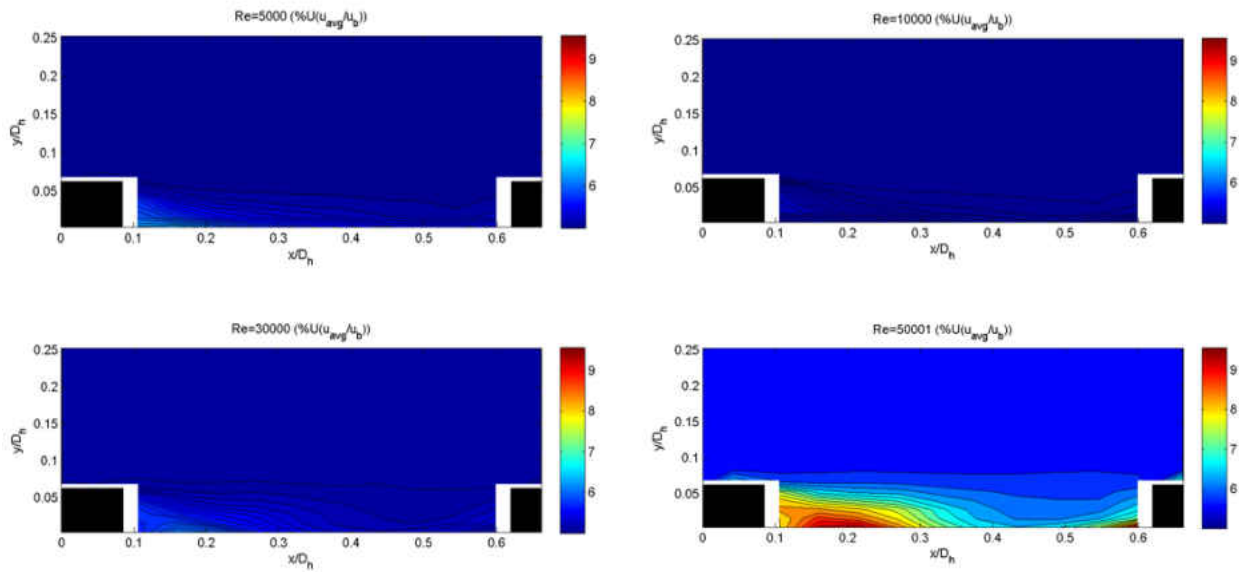


Figure 32 Uncertainty of Normalized Velocity

Figure 32 shows that, except for the repeated case of  $Re = 50,000$ , the uncertainty of the normalized velocity peaks about 6.5% near the bottom aft corner if the upstream rib where the flow velocity is very small and difficult to resolve.

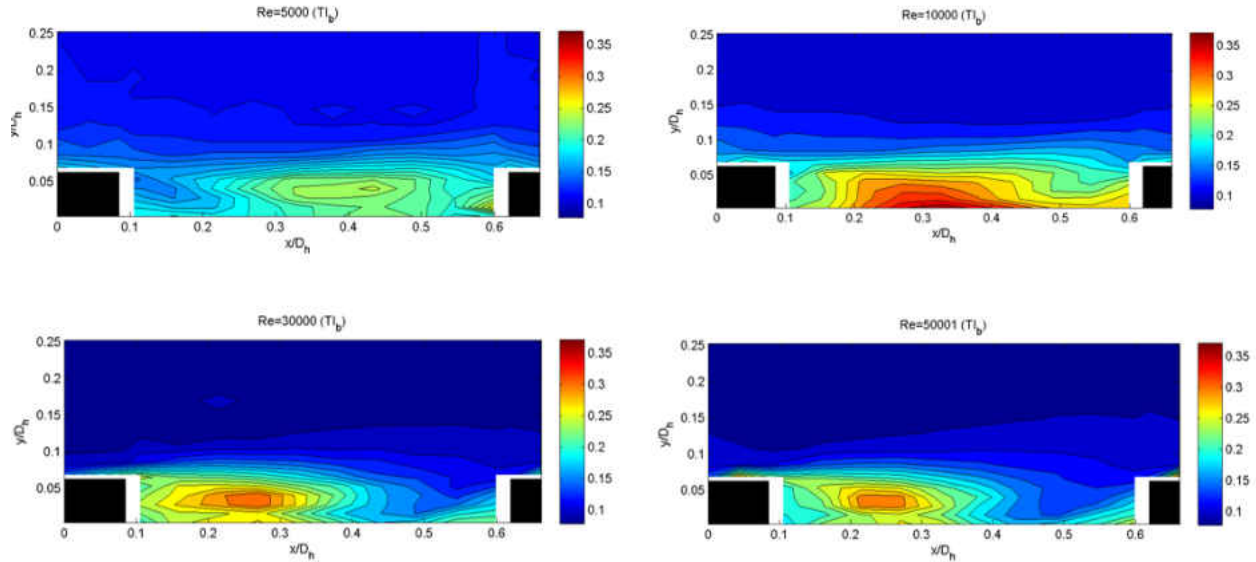


Figure 33 RMS Velocity Fluctuations Normalized by Local Velocity (TI)

Figure 33 depicts the turbulence intensity of the flow at the tested Reynolds numbers. It was observed that as Reynolds number increased, the peak in intensity dramatically moves upstream toward the aft of upstream rib, and maintained peak intensity within the Reynolds numbers tested. Unfortunately, after  $Re = 30,000$ , the peak in turbulence intensity was not located on the bottom wall surface. This shows that potential turbulent mixing is being “wasted” just above the recirculation zone, as it is not interacting much with the bottom wall surface.

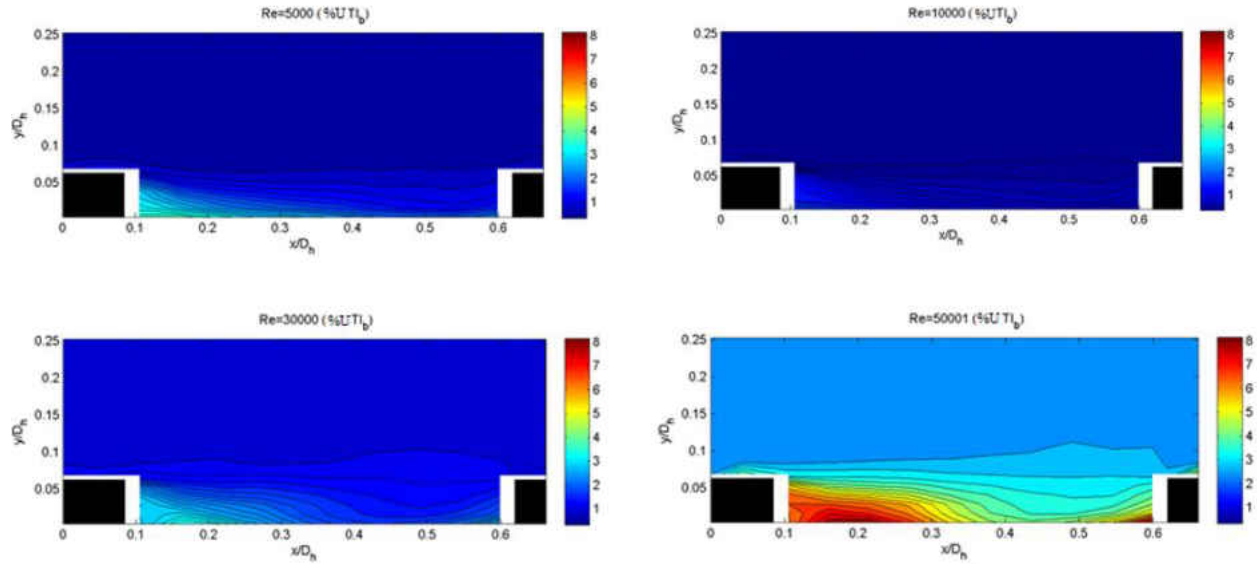


Figure 34 Uncertainty in Turbulence Intensity

Turbulence data was taken at ambient temperature flow conditions, but heat transfer data was obviously taken at heated flow conditions. A check to make sure that the turbulence data is still applicable for the heat transfer environment can be accomplished using Richardson number (Ri), the ratio of buoyant, natural convective forces over forced convection. In heated flow, the effect of density changes due to local air thermal gradients on the forced convection from the channel's driving pressure drop is scrutinized. A general rule of thumb for Richardson number is as follows: if  $Ri < 0.1$ , then natural convective forces are dominated by forced convection, and if  $Ri > 10$ , then natural convection dominates the forced convection. An Ri in between these limits implies that neither of these forces can be ignored in the overall flow behavior of the fluid.

$$Ri = \frac{g\beta(T_{hot}-T_{ref})L}{V^2} \begin{cases} Ri < 0.1 \text{ (natural convection is ignored)} \\ Ri > 10 \text{ (forced convection is ignored)} \\ 0.1 < Ri < 10 \text{ (neither can be ignored)} \end{cases} \quad (4.21)$$

Since local fluid temperature variations could not be calculated in the heat transfer experiments extreme values of temperature difference and local velocity will be used to estimate an upper and lower bound of this number to determine if density change would play a role in the turbulence calculations during a heat transfer run. Because the plate temperature is assumed to be isothermal at the target temperature of 70°C, the following table will show various scenarios of temperature differences, and velocities while holding the plate temperature constant. The length-scale of the Richardson number will be that of the hydraulic diameter of the channel,  $D_h = 0.0508\text{m}$ , and  $g$  will be the gravitational constant,  $9.81\text{m/s}^2$ .

Table 2 Hot-wire Data Validation in Heat Transfer Testing

	High $\Delta T$ , high V	Low $\Delta T$ , high V	High $\Delta T$ , low V	Low $\Delta T$ , low V
$T_{\text{plate}}$ (K)	343.15	343.15	343.15	343.15
$T_{\text{fluid}}$ (K)	298.15	323.15	298.15	323.15
$\beta$ , (1/K)	3.40E-03	3.10E-03	3.40E-03	3.10E-03
V (m/s)	100	100	1	1
Ri	7.62472E-06	3.08976E-06	0.076247244	0.030897576

In Table 2, even with a very high predictable temperature difference and a low velocity of 1 m/s, which has been observed within the recirculation regions in low Re, Richardson number remains below 0.1. This means that the flow should not be influenced by thermal effects even under the worst conceivable circumstance of column three in the above table.

Integral length-scale calculations were also made within the Reynolds number range of 5,000 to 50,000. At each Reynolds number, the most turbulent, highest standard deviation in velocity, point was located using a search algorithm in MATLAB. Below in Table 3, is a summary of these



locations, and what time-averaged velocity and standard deviation occurs at these locations. The majority of highest turbulence locations fall between  $x/D_h = 0.27$ , and  $y/D_h = 0.04$  to  $0.053$ .

Table 3 Location of Most Turbulent Points at Various Re

Re	$x/D_h$	$y/D_h$	$u_{avg}$ (m/s)	$u_{rms}$ (m/s)
5000	0.435	0.053	1.126	0.261
10000	0.270	0.053	2.123	0.676
30000	0.270	0.040	6.432	2.037
50000	0.270	0.053	11.434	2.964

The autocorrelation function, ACF, was utilized on the velocity fluctuations recorded at these locations.

$$R(\tau) = \frac{\langle w(t)w(t+\tau) \rangle}{\langle w^2 \rangle} \quad (4.22)$$

Data was collected for four seconds at a sampling frequency of 262kHz, with a lowpass filter of less than half the sampling frequency, 130kHz. A sample autocorrelation plotted against lags in seconds is shown below at  $Re = 50,000$ .

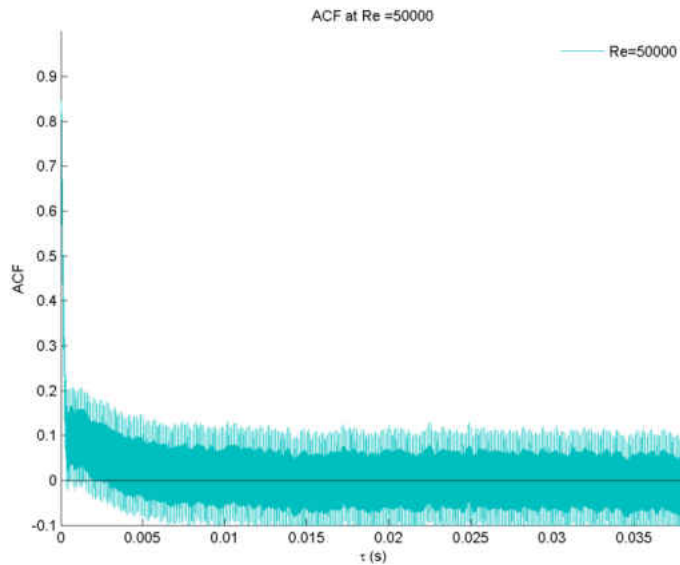


Figure 35 Autocorrelation Taken at Most Turbulent Point in  $Re = 50,000$

The integral length-scale was calculated using the ACF and the Taylor Frozen Hypothesis. The area under the curve of ACF yields the eddy integral time-scale,

$$T = \int_0^{\infty} r(\tau) d\tau \quad (4.23)$$

and the Taylor Frozen Hypothesis (which states that the local disturbances in a turbulent eddy as it passes a sensor are considered negligible, and the eddy velocity can be estimated as the local convective velocity) gives the eddy velocity. These terms can be multiplied together to get an eddy integral length scale. Below, in Table 4, integral time, and length-scales at each Reynolds number are tabulated.

Table 4 Integral Time and Length-Scales at Various Re

	$T$ (s)	$\Lambda$ (mm)	$\Lambda/e$
5000	0.00390	4.151	1.307
10000	0.00094	2.427	0.764
30000	0.00040	3.371	1.062
50000	0.00048	6.588	2.075

Table 4 shows that  $\Lambda/e$ , the ratio of integral length-scale to rib height has a generally increasing trend as a function of Reynolds number. At a Reynolds number of 45,000, Rivir et al. [ 30 ] calculated an integral length-scale of 1.5 times the rib height of a two-wall transverse rib case just downstream of the rib (very close to where this case's point was taken).

## CHAPTER 5: FINDINGS

In curiosity of how a replication, and extension of Han et al.'s [ 2 ] work with  $45^\circ$  ribs with a  $p/e$  of 10, and  $e/D_h$  of 0.0625 conducted by Ahmed et al. [ 1 ] would compare to a slight modification to Ahmed et al.'s original channel (converting a two-ribbed wall channel to single-ribbed wall channel), heat transfer, friction, and turbulence testing were carried out. Under nearly the same Reynolds number range of Ahmed et al.'s case, the single ribbed-wall case yielded  $\sim 1.4$  times less channel-averaged heat transfer capability than the two-wall case, but also half the friction than the two ribbed-wall case. Overall, the channel thermal performance as a function of Reynolds number between the two cases were about the same, the two ribbed-wall case having slightly better performance in the mid-range Reynolds numbers. Chandra et al. [ 20 ] concluded that overall performance declines as more ribbed walls are added, but this case and the two ribbed-wall case comparatively suggest that there are nearly no differences in thermal performance.

On a wall-based scale, the heat transfer of the two ribbed-wall case had nearly identical Nusselt curves for the top and bottom, and left and right walls, consecutively. This being explained by the channel's symmetric boundary conditions on the inner walls. The single ribbed-wall case, however, had asymmetric boundary conditions on the inner walls since only one wall (bottom) had ribs. The bottom ribbed-wall, by no surprise, yielded the highest heat transfer of the four walls in the single ribbed-wall case, the top smooth wall had the least, and the left and right walls having some heat transfer in between the top and bottom walls.

This lead to the idea of testing fully developed turbulence intensity within the channel, because there was a turbulent mixing gradient between the top and bottom walls as the heat transfer results hinted. The turbulent testing results shown that the mixing intensity, at least midspan of the

channel, did not have that much of a noticeable TI gradient, as conjectured. Turbulence intensity invoked by the ribs, nearly diminished only 10% of the channel height above the bottom wall surface. Velocity contours indicated that, although no directional information can be determined from a single wire hot-wire sensor, the location of a reattachment point of the flow after deflecting off an upstream rib can be roughly identified. As Reynolds number increase, the reattachment point appears hold position, but the velocities around the reattachment point increase, “filling in” the space between the ribs with faster and faster flow. The TI starts about midstream between two ribs, and retracts toward the upstream rib as Reynolds number increases. It was seen that the highest TI zones at each Reynolds number was not located on, or near the flow surface, where heat transfer would take place. This is unfortunate, to “waste” the mixing potential, but by modifying the IDC parameters, the high TI zone might be brought down closer to the surface to increase mixing heat transfer.

To ensure that the flow is under fully turbulent conditions, both the velocity of the flow at  $Re = 50,000$  and the standard deviation of the fluctuations were compared at the upstream rib center and the downstream rib center.

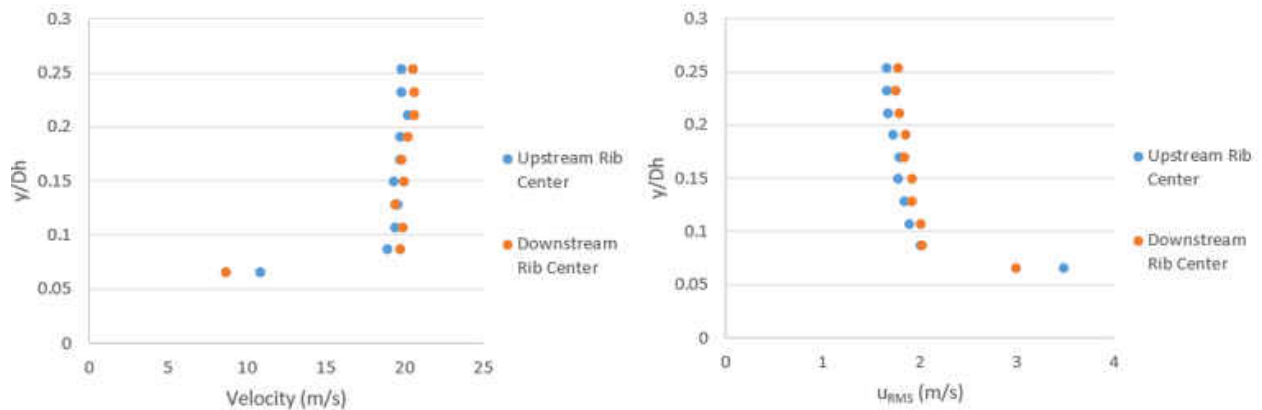


Figure 36 Velocity and Fluctuation Plots at  $Re = 50,000$

Figure 36 shows that at the same geographic locations in the rig, the center points of two ribs, the velocity and fluctuation profiles nearly match and are well within uncertainty of the velocity measurement. The flow is indeed fully turbulent at between the two ribs tested in the turbulence analysis.

Integral length-scale calculations predict an increasing trend between the Reynolds number, and length-scale located at the most turbulent point in the flow at each Re. Because there isn't a lot of length-scale as a function of Reynolds number data existing in literature for IDC, it is difficult to assert that the results obtained in this study are accurate. However, Rivir et al.'s [ 30 ] results show that at about the same location tested with respect to the ribs they used, the integral length-scale was approximately 1.5 times the rib height at a Reynolds number of 45,000. In this case the length-scale at  $Re = 50,000$  was twice the height. Several factors mentioned in the beginning of this thesis could influence the value of this integral length-scale, such as rib pitch, number of ribbed walls, rib angle (in his case transverse, 90deg). The fact that their scale is on the order of what was obtained in this case gives some level of confidence in the value.

Heat transfer testing was obviously conducted under hot wall condition, but the turbulent testing was done all at ambient temperature. If one were to try to compare, or extend the turbulence data to the heat transfer testing, could it be done? The Richard number, the ratio of natural vs. forced convection suggest that under the Reynolds numbers test, temperature gradients off the walls should not affect the flow with adverse air density gradients. The flow is too fast for natural convection to make any contribution to the flow mixing, or direction.

**APPENDIX A:**  
**UNCERTAINTIES OF MASS FLOWRATE**

$$P_{upstream} = P_{static} + P_{atm}$$

$$(U_{P_{upstream}})_{P_{static}} = \frac{\partial P_{upstream}}{\partial P_{static}} \cdot U_{P_{static}} = U_{P_{static}}$$

$$(U_{P_{upstream}})_{P_{atm}} = \frac{\partial P_{upstream}}{\partial P_{atm}} \cdot U_{P_{atm}} = U_{P_{atm}}$$

$$U_{P_{upstream}} = RSS \left[ (U_{P_{upstream}})_{P_{static}}, (U_{P_{upstream}})_{P_{atm}} \right]$$

$$T(K) = \frac{5}{9} (T(^{\circ}F) - 32) + 273.15$$

$$(U_{T(K)})_{T(^{\circ}F)} = \frac{\partial T(K)}{\partial T(^{\circ}F)} \cdot U_{T(^{\circ}F)} = \frac{5}{9} \cdot U_{T(^{\circ}F)}$$

$$\rho_{fluid} = \frac{P_{upstream}}{R T_{fluid}}$$

$$(U_{\rho_{fluid}})_{P_{upstream}} = \frac{\partial \rho_{fluid}}{\partial P_{upstream}} \cdot U_{P_{upstream}} = \frac{U_{P_{upstream}}}{R T_{fluid}}$$

$$(U_{\rho_{fluid}})_{T_{fluid}} = \frac{\partial \rho_{fluid}}{\partial T_{fluid}} \cdot U_{T_{fluid}} = \frac{P_{upstream}}{R T_{fluid}^2} \cdot U_{T_{fluid}, K}$$

$$U_{\rho_{fluid}} = RSS \left[ (U_{\rho_{fluid}})_{P_{upstream}}, (U_{\rho_{fluid}})_{T_{fluid}} \right]$$

$$\dot{m} = \rho_{fluid} Q$$

$$(U_{\dot{m}})_{\rho} = \frac{\partial \dot{m}}{\partial \rho} \cdot U_{\rho} = Q \cdot U_{\rho}$$

$$(U_{\dot{m}})_{Q} = \frac{\partial \dot{m}}{\partial Q} \cdot U_{Q} = \rho \cdot U_{Q}$$

$$U_{\dot{m}} = RSS \left[ (U_{\dot{m}})_{\rho}, (U_{\dot{m}})_{Q} \right]$$

**APPENDIX B:**  
**SYSTEMATIC UNCERTAINTIES OF NUSSELT NUMBER**



$$Q_{input} = \frac{V^2}{R}$$

$$U(Q_{input})_V = \frac{2V}{R}$$

$$U(Q_{input})_R = \left(\frac{V}{R}\right)^2$$

$$Q_{act} = Q_{input} - Q_{leakage}$$

$$U(Q_{act})_{Q_{input}} = U(Q_{input})$$

$$U(Q_{act})_{Q_{leakage}} = U(Q_{leakage})$$

$$T_{fluid,f} = \frac{Q_{act}}{\dot{m}c_p} + T_{fluid,i}$$

$$U(T_{fluid,f})_{Q_{act}} = \frac{U(Q_{act})}{\dot{m}c_p}$$

$$U(T_{fluid,f})_{\dot{m}} = \frac{U(\dot{m})Q_{act}}{\dot{m}^2 c_p}$$

$$U(T_{fluid,f})_{T_{fluid,i}} = U(T_{fluid,i})$$

$$\Delta T_{in,x} = T_{wall,x} - T_{fluid,i,x}$$

$$U(\Delta T_{in,x})_{T_{wall,x}} = U(T_{wall,x})$$

$$U(\Delta T_{in,x})_{T_{fluid,i,x}} = U(T_{fluid,i,x})$$

$$\Delta T_{out,x} = T_{wall,x} - T_{fluid,f,x}$$

$$U(\Delta T_{out,x})_{T_{wall,x}} = U(T_{wall,x})$$

$$U(\Delta T_{out,x})_{T_{fluid,f,x}} = U(T_{fluid,f,x})$$

$$LMTD_x = \frac{\Delta T_{in,x} - \Delta T_{out,x}}{\ln\left(\frac{\Delta T_{in,x}}{\Delta T_{out,x}}\right)}$$

$$U(LMTD_x)_{\Delta T_{in,x}} = U(\Delta T_{in,x}) \frac{\Delta T_{in,x} \ln\left(\frac{\Delta T_{in,x}}{\Delta T_{out,x}}\right) + \Delta T_{out,x} - \Delta T_{in,x}}{\Delta T_{in,x} \ln\left(\frac{\Delta T_{in,x}}{\Delta T_{out,x}}\right)^2}$$

$$U(LMTD_x)_{\Delta T_{out,x}} = U(\Delta T_{out,x}) \frac{\Delta T_{out,x} \ln\left(\frac{\Delta T_{in,x}}{\Delta T_{out,x}}\right) + \Delta T_{in,x} - \Delta T_{out,x}}{\Delta T_{out,x} \ln\left(\frac{\Delta T_{in,x}}{\Delta T_{out,x}}\right)^2}$$

$$\bar{h}_x = \frac{Q_{act} A}{T_{wall,x} - T_{fluid,f_x}}$$

$$U(\bar{h}_x)_{Q_{act}} = \frac{U(Q_{act}) A}{T_{wall,x} - T_{fluid,f_x}}$$

$$U(\bar{h}_x)_{T_{wall,x}} = \frac{U(T_{wall,x}) Q_{act} A}{(T_{wall,x} - T_{fluid,f_x})^2}$$

$$U(\bar{h}_x)_{T_{fluid,f_x}} = \frac{U(T_{fluid,f_x}) Q_{act} A}{(T_{wall,x} - T_{fluid,f_x})^2}$$

$$Nu_{D,x} = \frac{\bar{h}_x D_h}{k}$$

$$U(Nu_{D,x}) = \frac{U(\bar{h}_x) D_h}{k}$$

**APPENDIX C:**  
**SYSTEMATIC UNCERTAINTIES OF FRICTION FACTOR**

$$P_{in,abs} = P_{in,g} + P_{atm}$$

$$U(P_{in}) = RSS \left[ U(P_{in})_{P_{in,g}}, U(P_{in})_{P_{atm}} \right]$$

$$P_{out,abs} = P_{out,g} + P_{atm}$$

$$U(P_{out}) = RSS \left[ U(P_{out})_{P_{out,g}}, U(P_{out})_{P_{atm}} \right]$$

$$P_{avg,abs} = \frac{P_{in,atm} + P_{out,atm}}{2}$$

$$U(P_{avg,abs}) = RSS \left[ \frac{1}{2} U(P_{avg,abs})_{P_{in,atm}}, \frac{1}{2} U(P_{avg,abs})_{P_{out,atm}} \right]$$

$$\rho_{avg} = \frac{P_{avg,abs}}{R_{air} T_{amb}}$$

$$U(\rho_{avg})_{P_{avg,abs}} = \frac{U(P_{avg,abs})}{R_{air} T_{amb}}$$

$$U(\rho_{avg})_{T_{amb}} = U(T_{amb}) \frac{P_{avg,abs}}{R_{air} T_{amb}^2}$$

$$u_{avg} = \frac{\dot{m}}{\rho_{avg} A}$$

$$U(u_{avg})_{\dot{m}} = \frac{U(\dot{m})}{\rho_{avg} A}$$

$$U(u_{avg})_{\rho_{avg}} = U(\rho_{avg}) \frac{\dot{m}}{\rho_{avg}^2 A}$$

$$f_{Fanning,avg} = \frac{\frac{dP}{dx} D_h}{2 \rho_{avg} u_{avg}^2}$$

$$U(f_{Fanning,avg})_{\rho_{avg}} = U(\rho_{avg}) \frac{\frac{dP}{dx} D_h}{2 \rho_{avg}^2 u_{avg}^2}$$

$$U(f_{Fanning,avg})_{u_{avg}} = U(u_{avg}) \frac{\frac{dP}{dx} D_h}{\rho_{avg} u_{avg}^3}$$

**APPENDIX D:**  
**SYSTEMATIC UNCERTAINTIES OF TURBULENCE**

Source of uncertainty	Input varians	Typical value	Relative output varians	Typical value	Coverage factor	Relative standard uncertainty
	$\Delta x_i$	$\Delta x_i$	$\frac{1}{U} \cdot \Delta y_i$	$\frac{1}{U} \cdot \Delta y_i$	$k$	$\frac{1}{k} \cdot \frac{1}{U} \cdot \Delta y_i$
Calibrator	$\Delta U_{cal}$	1%	$2 \cdot \text{STDV}(100 \cdot \Delta U_{cal})$	0.02	2	0.01
Linearisation	$\Delta U_{fit}$	0.5%	$2 \cdot \text{STDV}(100 \cdot \Delta U_{fit})$	0.01	2	0.005
A/D resolution	$E_{AD}$ $n$	10 volts 12 bit	$\frac{1}{U} \cdot \frac{E_{AD}}{2^n} \cdot \frac{\partial U}{\partial E}$	0.000 8	$\sqrt{3}$	0.0013
Probe positioning	$\theta$	1°	$1 - \cos \theta$	0.000 15	$\sqrt{3}$	$\approx 0$
Temperature variations <sup>1)</sup>	$\Delta T$	1 °C	$\frac{1}{U} \cdot \frac{\Delta T}{(T_w - T_0)} \cdot \left( \frac{A}{B} \cdot U^{-0.5} + 1 \right)$	0.013	$\sqrt{3}$	0.008
Temperature variations <sup>2)</sup>	$\Delta T$	1 °C	$\frac{\Delta T}{273}$	0.004	$\sqrt{3}$	0.002
Ambient pressure	$\Delta P$	10 kPa	$\frac{P_0}{P_0 + \Delta P}$	0.01	$\sqrt{3}$	0.006
Humidity	$\Delta P_{wv}$	1 kPa	$\frac{1}{U} \cdot \frac{\partial U}{\partial P_{wv}} \cdot \Delta P_{wv}$	0.000 6	$\sqrt{3}$	$\approx 0$
Relative expanded uncertainty <sup>3)</sup> : $U(U_{\text{sample}}) = 2 \cdot \sqrt{\sum \left( \frac{1}{k} \cdot \frac{1}{U} \cdot \Delta y_i \right)^2} = 0.030 = 3 \%$						

**APPENDIX E:**  
**MATLAB CODE FOR TURBULENCE ANALYSIS**

## Converting Voltage Files to Velocity Files:

```
b=input('New hotwire Calibration? (y/n) ','s');
if b=='y'
    %Open calibration M-file, and retrieve velocity coeffs
    disp('Select calibration correlation MATLAB file');
    [filename, pathname]=uigetfile({'*.m'},'File Selector');
    run(strcat(pathname,filename));

    %Steps:
    %Load calibration M-file
    %Select calibration text file
    %Enter recorded calibration ambient pressure [mbar]
    clc;
    clearvars htwcal v b
else
end

disp('Locate Hotwire Voltage Data Folder');
directory=uigetdir;
cd(directory)
files=dir(directory);
fileindex=find(~[files.isdir]);
filelist=cell(length(fileindex),1);
for i=1:length(fileindex)
    filelist{i}=files(fileindex(i)).name;
end
clearvars i
clc

VEL=zeros(length(getfield(importdata(filelist{1},'\t',23),'data')),1);

disp('Locate Hotwire Velocity Data Folder');
directory2=uigetdir;

for i=1:length(fileindex)
    B=getfield(importdata(strcat(directory,'\',filelist{i}),'\t',23),'data');
    Bin=B(:,2);
    VEL=calibcoeff(1,1).*Bin.^4+... % VEL = matrix of (data points,y-locations,x-locations)
        calibcoeff(1,2).*Bin.^3+... % Using Calibrator Venturi Nozzle
        calibcoeff(1,3).*Bin.^2+...
        calibcoeff(1,4).*Bin+...
        calibcoeff(1,5);

    fileID=fopen(strcat(directory2,'\',strep(filelist{i},'.lvm','.txt')),'w');
    fprintf(fileID,'%10.6f\r\n',VEL);
    Bin(:)=0;
    VEL(:)=0;
    clc
    disp(strcat('progress: ',num2str(i),'/',num2str(length(fileindex))))
```



```
end
clearvars i
```

*Published with MATLAB® R2014a*

Velocity, Turbulence Intensity, Spectral, and Length Scale Analysis:

```
% Hotwire Analysis for Ribbed Channels (2D Region)
% streamwise traversing is done backwards (upstream direction)
```

### Defining Zonal Layout in Topographic 2-D Region

```
disp('Locate main hotwire folder')
maindir=uigetdir;
cd(maindir)

disp('Locate Relevant Velocity Data File for Sample Size Determination')
sizedir=uigetdir;
cd(sizedir)
NS=size(load('z1x1y1.txt'),1); %Number of samples collected
cd(maindir)

x_matr = [1,2;1,10;1,3]; % x-locations per section
xmax=sum(x_matr(:,2));

y_matr = [6,10;6,9;6,10]; % y-locations per section
ymax=max(sum(y_matr,2));

z_matr = [0,1;2,3;0,4]; % zones (zones with solids should be valued "0")
sects=size(z_matr,1);

zero_pts=6; % number of y-points that will be within a solid per zone)

q1=input('Adding another test? (y/n) ','s');
if q1=='y'
    ZBin=zeros(NS,ymax,max(z_matr(:)));
    XBin=zeros(NS,xmax);
    VEL=zeros(NS,ymax,xmax);
    clc
    disp('Navigate to section:')
    disp('Velocity Binning')
else
    clc
    disp('Navigate to section:')
    disp('Mesh Gridding & Re/Bulk Velocity Test Matrix Setup')
```

```
clearvars x_matr ymax zmax
end
```

## Velocity Binning

```
cd(sizedir)
pos=0;
for i=1:sects % i = 1 to number of streamwise sections - (1 to 3 for IDC)

    % Scanning each x-location
    m=x_matr(i,:); % m-vector is defined as the (i)th row of x_matr
    for x=min(m(m>0), [],2): max(m)
        % max/min non-zero values in m - (number of x-pts in (z)th zone)

        % Creating Zone matrices per x-location
        n=z_matr(i,:); % n-array is defined as the (i)th row of z_matr
        for z=min(n(n>0), [],2): max(n)
            % max/min non-zero values in n - (zone numbers per section)

            % Filling in z(th) Zone matrix
            p=y_matr(i,:);
            % p-array is defined as the (i)th row of y_matr
            % - (number of y-pts in (z)th zone)
            for y=1:p(find(n==z)) %#ok<FNDSB>
                disp('streamwise position')
                disp(pos+1)
                disp('streamwise location')
                disp(x)
                disp('zone')
                disp(z)
                disp('vertical location')
                disp(y)
                ZBin(:,y,z)=load(strcat('z',num2str(z),'x',num2str(x),...
                    'y',num2str(y),'.txt'));
                clc
            end
        end
    end

    col=1;
    for j=min(n(n>0), [],2): max(n)
        for k=1:sum(ZBin(1,:,j)~=0)
            XBin(:,col)=ZBin(:,k,j);
            col=col+1;
        end
    end

    pos=pos+1;
    VEL(:, :, pos)=circshift(XBin, sum(XBin(1, :)==0), 2);
    XBin=zeros(NS,ymax);
end
```

```

end
clc
cd(maindir)
clearvars i j k x y z col m n p pos sizedir XBin ZBin

disp('Navigate to section:')
disp('Gridded Velocities/STDEVs')

```

## Gridded Velocities/STDEVs

```

clc
avgvel=zeros(1,ymax,xmax); % Average velocities initial matrix building
for i=1:xmax
    for j=1:ymax
        avgvel(1,j,i)=mean(VEL(:,j,i));
    end
end
avgvel=reshape(avgvel,ymax,xmax);
avgvel=fliplr(avgvel);
avgvel(1:zero_pts,1:max(x_matr(3,:)))=NaN;
avgvel(1:zero_pts,sum(x_matr(2:3,2))+1:sum(x_matr(2:3,2))+x_matr(1,2))=NaN;
avgvel(1,:)=[];

stdev=zeros(1,ymax,xmax); % Standard deviations initial matrix building
for i=1:xmax
    for j=1:ymax
        stdev(1,j,i)=std(VEL(:,j,i));
    end
end
stdev=reshape(stdev,ymax,xmax);
stdev=fliplr(stdev);
stdev(1:zero_pts,1:max(x_matr(3,:)))=NaN;
stdev(1:zero_pts,sum(x_matr(2:3,2))+1:sum(x_matr(2:3,2))+x_matr(1,2))=NaN;
stdev(1,:)=[];
clearvars i j

% Saving avgvel and stdev matrices to defined directory
q2=input('What Reynolds Number did you test? ');
save(strcat(maindir,'\avgvel\',num2str(q2),'_avgvel.mat'),'avgvel');
save(strcat(maindir,'\stdev\',num2str(q2),'_stdev.mat'),'stdev');
clearvars q2
clc

disp('Navigate to section:')
disp('Mesh Gridding & Re/Bulk Velocity Test Matrix Setup')
disp('You will need:')
disp({'Tested Reynolds number';'Bulk velocity at that Reynolds number'})

```

## Mesh Gridding & Re/Bulk Velocity Test Matrix Setup

```

clc
% Load x, and y arrays (x=[1:N], y=[N:1])
load(strcat(maindir, '\parameters\probecoord'));
x_Dh=x./0.0508;
y_Dh=y./0.0508;
[X,Y]=meshgrid(x_Dh,y_Dh);

% Test velocities
% Load bulk velocity array, and Reynolds number array w/ new entries [N:1]

q3=input('First hot-wire test? (y/n) ','s');
if q3=='y'
Re=input('Input Reynolds number tested -> ');
velb=input('Input bulk (mass flow) velocity tested -> ');
elseif q1=='y'
load(strcat(maindir, '\parameters\flowparam'));
m=length(Re);
a=input('Input Reynolds Number -> ');
b=input('Input bulk (mass flow) velocity -> ');
if a>max(Re) % new entries added from the right
Re(m+1)=a;
velb(m+1)=b;
clearvars a b
elseif a<min(Re) % new entries added from the left
Re(m+1)=0;
Re=circshift(Re,1,2);
Re(1)=a;
clearvars a
velb(m+1)=0;
velb=circshift(velb,1,2);
velb(1)=b;
clearvars b
else % new entries added in between existing entries
for i=1:m
if and(Re(i)<a,Re(i+1)>a);
Re=[Re(1:i) a Re(i+1:end)];
velb=[velb(1:i) b velb(i+1:end)];
end
end
clearvars a b i
end
else
load(strcat(maindir, '\parameters\flowparam'));
end
clearvars q3
m=find(Re==max(Re));
save(strcat(maindir, '\parameters\flowparam.mat'),'Re','velb');
clc

qunc=input('Uncertainty Calculations for your plots? (y/n) ','s');
if qunc=='y'

```

```

cd(maindir)
run('Kings_law.m')
run('Calibration_Uncertainty.m')
q4='n';
disp('Navigate to section:')
disp('Obstacle Image Preparation')
else
q4=input('Just plotting integral length scale and spectra? (y/n) ','s');
disp('Navigate to section:')
disp('Obstacle Image Preparation')
end

```

## Obstacle Image Preparation

```

clc

r1=input('Number of streamwise locations on first streamwise rib (3)-> ');
r2=input('Number of streamwise locations on second streamwise rib (2)-> ');
probe1xo=min(x_Dh); % Probe boundary image cut (/Dh)
probe1yo=min(y_Dh); %
probe1w=x_Dh(r1+1)-min(x_Dh); %
probe1h=y_Dh(zero_pts); %
probe2xo=x_Dh(length(x_Dh)-r2); %
probe2yo=probe1yo; %
probe2w=max(x_Dh)-x_Dh(length(x_Dh)-r2); %
probe2h=probe1h; %

load(strcat(maindir, '\parameters\rib_spec.mat'))

delay=0.75; % Set time delay (seconds) for animated GIF images
disp('Navigate to section:')
disp('MAX/MIN Scaling Control')

```

## MAX/MIN Scaling Control

```

clc
AVGL=zeros(length(y),length(x),m);
NONAVGL=zeros(length(y),length(x),m);
STDV=zeros(length(y),length(x),m);
NONSTDV=zeros(length(y),length(x),m);
TI=zeros(length(y),length(x),m);

NONVELUNCRTPRCNT=zeros(length(y),length(x),m);
TIUNCRTPRCNT=zeros(length(y),length(x),m);

for i=1:m
load(strcat(maindir, '\avgvel\ ', num2str(Re(i)), '_avgvel.mat'));
load(strcat(maindir, '\stdev\ ', num2str(Re(i)), '_stdev.mat'));

```

```

AVGL(:, :, i)=avgvel;
STDV(:, :, i)=stdev;
if q4=='n'
    NONAVGL(:, :, i)=avgvel./velb(i);
    NONSTDV(:, :, i)=stdev./velb(i);
    TI(:, :, i)=stdev./avgvel;
    if qunc=='y'
%         load(strcat(maindir, '\hotwire calibrations\UVELB.mat'))
        NONVELUNCRTPRCNT(:, :, i)=100.*sqrt((mean(...
            UPRCNT.(strcat('Re', num2str(Re(i))))(:, 6))./velb(i)).^2+...
            (1./velb(i).^2.*UVELB(i).*avgvel).^2)./NONAVGL(:, :, i);
        TIUNCRTPRCNT(:, :, i)=100.*mean(UPRCNT.(strcat('Re', num2str(Re(i))))...
            (:, 6))./avgvel.^2.*stdev./TI(:, :, i);
    end
else
end
end
clearvars i

if q4=='n'
    nonavg1_max=max(NONAVGL(:));
    nonavg1_min=min(NONAVGL(:));
    ti_max=max(TI(:)); %----- user control!!
    ti_min=min(TI(:));
    stdev_max=max(STDV(:)); %----- user control!!
    stdev_min=min(STDV(:));
    nonstdv_max=max(NONSTDV(:)); %----- user control!!
    nonstdv_min=min(NONSTDV(:));
    nonveluncrtprcnt_min=min(NONVELUNCRTPRCNT(:));
    nonveluncrtprcnt_max=max(NONVELUNCRTPRCNT(:));
    tiuncrtprcnt_min=min(TIUNCRTPRCNT(:));
    tiuncrtprcnt_max=max(TIUNCRTPRCNT(:));
    contlyr=15; %----- user control!! (number of contour layers)
    disp('Navigate to section:')
    disp('Interpolated Surface Plots (Non-D Velocity, TI, STDEV, Non-D STDEV)')
else
    disp('Navigate to section:')
    disp('Locating Most Turbulent Grid Points on Rib for All Re Cases')
end
% clearvars q4

```

## Locating Most Turbulent Grid Points for All Re Cases in Rib Valley

```

stdevloc=zeros(m, 2);
velFluctBin=zeros(NS, m);

cd autocorrelations
b=struct2cell(dir('*autocorr*'));
c=sort(str2double(strrep(b(1, :), '_autocorr.mat', '')));
cd(maindir)

```

```

clearvars b

valoc=input('Number of points taken in rib valley (5) -> ');
r1=input('Number of streamwise locations on first streamwise rib (3)-> ');
r2=input('Number of streamwise locations on second streamwise rib (2)-> ');

% Locating relevant velocity data files (in Zone 2 -rib valley)
for a=1:m
    clc
    if any(c==Re(a))
        velFluctBin(:,a)=0;
        disp(strcat(sprintf('%.0f%%',100*(a/m)), ' - velFluctBin complete'))
    else
        STDV_sub=STDV(:, :, a);
        % [y's from bottom surface, downstream x's]
        [i,j]=ind2sub(size(STDV_sub(1:valoc,(r1+1):(length(x_Dh)-r2))),...
            find(STDV_sub(1:valoc,(r1+1):(length(x_Dh)-r2))==...
                max(max(STDV_sub(1:valoc,(r1+1):(length(x_Dh)-r2))))));
        stdevloc(a,:)=[i,j];
        filename=strcat(maindir,'\hotwire tests\',strcat(num2str(Re(a)),...
            ' Raw\Velocities\z2x',num2str(stdevloc(a,2)), 'y',num2str(stdevloc(a,1)),...
            '.txt'));
        % d(a,1)={filename}; % to check which files are being pulled
        B=load(filename);
        velFluctBin(:,a)=B(1:NS,1);
        clearvars B filename STDV_sub
        disp(strcat(sprintf('%.0f%%',100*(a/m)), ' - velFluctBin complete'))
    end
end
clearvars a i j

for i=1:m
    clc
    if std(velFluctBin(:,i))==0
        disp(strcat(sprintf('%.0f%%',100*(i/m)), ' - U-file complete (already done)'))
    else
        U=velFluctBin(:,i);
        U_bar=mean(velFluctBin(:,i));
        u=U-U_bar;
        save(strcat(maindir,'\autocorrelations\turb velocity fluct\',...
            num2str(Re(i)), '_U.mat'), 'U');
        save(strcat(maindir,'\autocorrelations\turb velocity fluct\',...
            num2str(Re(i)), '_U_bar.mat'), 'U_bar');
        save(strcat(maindir,'\autocorrelations\turb velocity fluct\',...
            num2str(Re(i)), '_u_fluct.mat'), 'u');
        clearvars U
        disp(strcat(sprintf('%.0f%%',100*(i/m)), ' - U-file complete'))
    end
end
clc

clearvars velFluctBin vel U_bar u U i

```

```
disp('Navigate to section:')
disp('Length Scales - Autocorrelation')
```

## Length Scales - Autocorrelation

```
% Autocorrelation Parameter Setup
f_s=262000;      % sampling frequency (Hz)
f_s_new=262000;
fr=f_s/f_s_new;
dt = 1/f_s_new;  % time step (s)
maxlag=10000;   % autocorrelation lags
lags=0:maxlag;
tau=lags.*dt;
clearvars f_s

%Autocorrelation
cor=zeros(m,maxlag+1);
lgnd=cell(1,m);
%   % Autocorrelation function; u = U - <U>
%
%       rho(tau)= <u(t)*u(t+tau)>
%               -----
%               <u^2(t)>

for i=1:m
    if any(c==Re(i))
        disp(strcat(sprintf('%.0f%%',100*(i/m)), ' - autocorr-file complete'))
    else
        disp(strcat(sprintf('%.0f%%',100*(i/m)), ' - autocorr-file complete'))
        lgnd{i}=strcat('Re = ',num2str(Re(i)));
        load(strcat(maindir, '\autocorrelations\turb velocity fluct\', ...
            num2str(Re(i)), '_u_fluct.mat'));
        u_new=u(1:fr:NS);
        %   sumacorr=zeros(maxlag,1);
        %       for k=0:maxlag
        %           u_new_tau=circshift(u_new, [-k,0]);
        %           prod=u_new.*u_new_tau;
        %           sumacorr(k+1)=sum(prod(1:(length(prod)-k)));
        %       end
        %   acorr=1/(length(u_new)-1).*sumacorr./var(u_new);
        rho=xcorr(u_new,maxlag)./((length(u_new)-1).*var(u_new));

        save(strcat(maindir, '\autocorrelations\', num2str(Re(i)), '_autocorr.mat'), ...
            'rho');
        cor(i,:)=rho(maxlag+1:2*maxlag+1);
        clearvars u U
        clc
    end
end
```



```

figure
hold on
atcr=plot(tau,cor);
lclr={get(atcr,'color')};
lnc1r=lclr{1,1};
legend(lgnd);
legend('boxoff');
plot([0 max(tau)], [0 0], 'color', 'k')
xlim([0 max(tau)])
xlabel('\tau (s)');
ylim([-0.1 1])
ylabel('ACF');
title('ACF for all Re');
hold off
saveas(gcf, strcat(maindir, '\figures\acf'), 'png');
set(gcf, 'visible', 'off');

for i=1:m
    figure
    hold on
    plot(tau,cor(i,:), 'color', lnc1r{i});
    plot([0 max(tau)], [0 0], 'color', 'k')
    xlim([0 max(tau)])
    xlabel('\tau (s)');
    ylim([-0.1 1])
    ylabel('ACF');
    lgnd(i)={strcat('Re=', num2str(Re(i)))};
    legend(strcat('Re=', num2str(Re(i))));
    legend('boxoff');
    title(strcat('ACF at Re = ', num2str(Re(i))));
    hold off
    saveas(gcf, strcat(maindir, '\figures\', num2str(Re(i)), '_acf'), 'png');
    set(gcf, 'visible', 'off');
end

% clearvars lclr i j u

% Taylor Microscales
cd autocorrelations
lag_tylr=3;
max_tylr_tau=lag_tylr.*dt;
tau_tylr=0:dt:dt*(lag_tylr-1);
tylr_tscale=zeros(1,m);
tylr_autocorr_fit=zeros(m,3);

for i=1:m
    load(strcat(maindir, '\autocorrelations\turb velocity fluct\', ...
        num2str(Re(i)), '_U_bar.mat'));
    ubar(i)=U_bar; %#ok<SAGROW>
end

figure

```

```

for i=1:m
    tylr_autocorr_fit(i,:)=polyfit(tau(1:lag tylr),cor(i,1:lag tylr),2);
    rts=roots(tylr_autocorr_fit(i,:));
    tylr_tscale(i)=rts(rts>0);
    hold on
    atcr=plot(tau,cor);
    tau tylr parab=linspace(0,tylr_tscale(i),lag tylr);
    tylr_para=tylr_autocorr_fit(i,1).*tau tylr parab.^2+...
        tylr_autocorr_fit(i,2).*tau tylr parab+...
        tylr_autocorr_fit(i,3);
    para=plot(tau tylr parab,tylr_para,'Color',lnc1r{i},'LineStyle','--');
    clc
end

tylr_lscale=tylr_tscale.*ubbar; % Taylor Frozen Field Hypothesis

save(strcat(maindir,'\autocorrelations\Taylor scales\tylr_tscale.mat'),...
    'tylr_tscale');
save(strcat(maindir,'\autocorrelations\Taylor scales\tylr_lscale.mat'),...
    'tylr_lscale');

legend(lgnd);
legend('boxoff');
str={'ACF - solid';'Taylor - dashed'};
dim=[0.4 0.6 0.3 0.3];
annotation('textbox',dim,'String',str,'FitBoxToText','on','FontSize',9);
title('ACF for all Tested Re - Taylor Parabolas');
xlabel('\tau (s)');
ylabel('ACF');
ylim([0,1])
xlim([0,2*max(tylr_tscale)])
hold off
saveas(gcf,strcat(maindir,'\figures\acf_taylor_tscales'),'png');
set(gcf,'visible','off');
cd(maindir)

% Integral Scales - Trapezoidal Integral Approximation
cd autocorrelations
int_tscale=zeros(1,m);
int_lscale=zeros(1,m);
for i=1:m
    int_tscale(i)=trapz(tau,cor(i,:));
    int_lscale(i)=int_tscale(i)*ubbar(i);
    save(strcat(maindir,'\autocorrelations\integral scales\int_tscale.mat'),...
        'int_tscale');
    save(strcat(maindir,'\autocorrelations\integral scales\int_lscale.mat'),...
        'int_lscale');
end
cd(maindir)
clearvars i

```

## Energy Spectrum - Autocovariance to Fourier Transform

```
% Autocovariance
cov=zeros(m,maxlag+1);
for i=1:m
%   if any(c==Re(i))
%   disp(strcat(sprintf('%.0f%%',100*(i/m)),' - autocorr-file complete'))
%   else
tic
disp(i)
lgnd{i}=strcat('Re = ',num2str(Re(i)));
load(strcat(maindir,'\autocorrelations\turb velocity fluct\',num2str(Re(i)),...
'_u_fluct.mat'));
R=xcov(u,maxlag)./(NS-1);
save(strcat(maindir,'\autocorrelations\',num2str(Re(i)),'_autocov.mat'),'R');
disp(strcat(sprintf('%.0f%%',100*(i/m)),' - autocov-file complete'))
cov(i,:)=R(maxlag+1:2*maxlag+1);
toc
clearvars U
clc
% end
end
```

## Fourier Transform

```
E2=zeros(1,maxlag+1);
E=zeros(1,maxlag/2+1);
for i=1:m
E2(i,:)=abs(fft(cov(i,:))/maxlag); %Two-sided spectrum
E(i,:)=2.*E2(i,1:maxlag/2+1); %Two-sided -> Single-sided spectrum
f=1/dt*(0:(maxlag/2))/maxlag;
hold on
figure
loglog(f,E(i,:));
title('Energy Spectra for all Tested Re');
legend(num2str(Re(i)));
legend('boxoff');
xlabel('Frequency');
ylabel('Energy');
hold off
save(strcat(maindir,'\autocorrelations\',num2str(Re(i)),'_energy.mat'),'E');
saveas(gcf,strcat(maindir,'\figures\energy_spectra_Re=',num2str(Re(i))),'png');
set(gcf,'visible','off');
end
```

```
figure
loglog(f,E);
title('Energy Spectra for all Tested Re');
legend(lgnd);
```

```

legend('boxoff');
xlabel('Frequency');
ylabel('Energy');
saveas(gcf, strcat(maindir, '\figures\energy_spectra'), 'png');

```

## Interpolated Surface Plots (Non-D Velocity, TI, STDEV, Non-D STDEV)

```

aspect=max(x)/max(y);

filename=strcat(maindir, '\gifs\surf_vel.gif');
for i=1:m % Non-Dimensional Average Velocity "u_{avg}/u_{bulk}"
    figure('Name', 'NonDim Velocity - SurfPlot', 'NumberTitle', 'off')
    hold on
    surfc(X,Y,AVGL(:, :, i)./velb(i), 'FaceColor', 'interp');
    title(strcat('Re= ', num2str(Re(i)), ' (u_{avg}/u_b)'));
    xlabel('x/D_h');
    ylabel('y/D_h');
    view(0,90);
    rectangle('position', [rib1xo, rib1yo, rib1w, rib1h], 'Facecolor', [0,0,0], ...
        'EdgeColor', 'k');
    rectangle('position', [rib2xo, rib2yo, rib2w, rib2h], 'Facecolor', [0,0,0], ...
        'EdgeColor', 'k');
    axis('tight');
    pbaspect([aspect 1 1])
    grid('on');
    colorbar;
    caxis([nonavgl_min nonavgl_max]);
    pause(1/2);
    [A, map] = rgb2ind(frame2im(getframe(gcf)), 256);
    if i == 1
        imwrite(A, map, filename, 'gif', 'LoopCount', Inf, 'DelayTime', delay);
    else
        imwrite(A, map, filename, 'gif', 'WriteMode', 'append', 'DelayTime', delay);
    end
    saveas(gcf, strcat(maindir, '\figures\surf_vel\' , num2str(Re(i)), '_surf_vel'), ...
        'png');
    set(gcf, 'visible', 'off');
end

filename=strcat(maindir, '\gifs\surf_uvel.gif');
for i=1:m % Non-Dimensional Average Velocity Uncertainty "%U(u_{avg}/u_{bulk})"
    figure('Name', 'NonDim Velocity %Uncertainty - SurfPlot', 'NumberTitle', 'off')
    hold on
    rectangle('position', [rib1xo, rib1yo, rib1w, rib1h], 'Facecolor', [0,0,0], ...
        'EdgeColor', 'k');
    rectangle('position', [rib2xo, rib2yo, rib2w, rib2h], 'Facecolor', [0,0,0], ...
        'EdgeColor', 'k');
    surfc(X,Y, NONVELUNCRTPRCNT(:, :, i), 'FaceColor', 'interp');
    title(strcat('Re= ', num2str(Re(i)), ' (%U(u_{avg}/u_b)'));
    xlabel('x/D_h');

```

```

ylabel('y/D_h');
view(0,90);
axis('tight');
pbaspect([aspect 1 1])
grid('on');
colorbar;
caxis([nonveluncrtprcnt_min nonveluncrtprcnt_max]);
pause(1/2);
[A,map] = rgb2ind(frame2im(getframe(gcf)),256);
if i == 1
    imwrite(A,map,filename,'gif','LoopCount',Inf,'DelayTime',delay);
else
    imwrite(A,map,filename,'gif','WriteMode','append','DelayTime',delay);
end
saveas(gcf,strcat(maindir,'\figures\surf_uvel\ ',num2str(Re(i)),'_surf_uvel'),...
    'png');
set(gcf,'visible','off');
end

filename=strcat(maindir,'\gifs\surf_ti.gif');
for i=1:m % Turbulence Intensities "u_{rms}/u_{avg}"
    figure('Name','TI - SurfPlot','NumberTitle','off')
    hold on
    surf(X,Y,STDV(:,:,i)./AVGL(:,:,i),'FaceColor','interp');
    title(strcat('Re= ',num2str(Re(i)),' (TI)'));
    xlabel('x/D_h');
    ylabel('y/D_h');
    view(0,90);
    rectangle('position',[rib1xo,rib1yo,rib1w,rib1h],'Facecolor',[0,0,0],...
        'EdgeColor','k');
    rectangle('position',[rib2xo,rib2yo,rib2w,rib2h],'Facecolor',[0,0,0],...
        'EdgeColor','k');
    axis('tight');
    pbaspect([aspect 1 1])
    grid on;
    colorbar;
    caxis([ti_min ti_max]);
    pause(1/2);
    [A,map] = rgb2ind(frame2im(getframe(gcf)),256);
    if i == 1
        imwrite(A,map,filename,'gif','LoopCount',Inf,'DelayTime',delay);
    else
        imwrite(A,map,filename,'gif','WriteMode','append','DelayTime',delay);
    end
    saveas(gcf,strcat(maindir,'\figures\surf_ti\ ',num2str(Re(i)),'_surf_ti'),...
        'png');
    set(gcf,'visible','off');
end

filename=strcat(maindir,'\gifs\surf_uti.gif');
for i=1:m % Turbulence Intensity Uncertainties "%U(u_{rms}/u_{avg})"
    figure('Name','TI Uncertainty - SurfPlot','NumberTitle','off')

```

```

hold on
surfc(X,Y,TIUNCRTPRCNT(:,:,i),'FaceColor','interp');
title(strcat('Re= ',num2str(Re(i)), ' (%U(TI))'));
xlabel('x/D_h');
ylabel('y/D_h');
view(0,90);
rectangle('position',[rib1xo,rib1yo,rib1w,rib1h],'Facecolor',[0,0,0],...
          'EdgeColor','k');
rectangle('position',[rib2xo,rib2yo,rib2w,rib2h],'Facecolor',[0,0,0],...
          'EdgeColor','k');
axis('tight');
pbaspect([aspect 1 1])
grid on;
colorbar;
caxis([tiuncrtprcnt_min tiuncrtprcnt_max]);
pause(1/2);
[A,map] = rgb2ind(frame2im(getframe(gcf)),256);
if i == 1
    imwrite(A,map,filename,'gif','LoopCount',Inf,'DelayTime',delay);
else
    imwrite(A,map,filename,'gif','writeMode','append','DelayTime',delay);
end
saveas(gcf,strcat(maindir,'\figures\surf_uti\' ,num2str(Re(i)),'_surf_uti'),...
        'png');
set(gcf,'visible','off');
end

filename=strcat(maindir,'\gifs\surf_stdev.gif');
for i=1:m % Standard Deviation "u_{rms}"
    figure('Name','Stdev - SurfPlot','NumberTitle','off')
    hold on
    surfc(X,Y,STDV(:,:,i),'FaceColor','interp');
    title(strcat('Re= ',num2str(Re(i)), ' (u_{rms})'));
    xlabel('x/D_h');
    ylabel('y/D_h');
    view(0,90);
    rectangle('position',[rib1xo,rib1yo,rib1w,rib1h],'Facecolor',[0,0,0],...
              'EdgeColor','k');
    rectangle('position',[rib2xo,rib2yo,rib2w,rib2h],'Facecolor',[0,0,0],...
              'EdgeColor','k');
    axis('tight');
    pbaspect([aspect 1 1])
    grid on;
    colorbar;
    caxis([stdev_min stdev_max]);
    pause(1/2);
    [A,map] = rgb2ind(frame2im(getframe(gcf)),256);
    if i == 1
        imwrite(A,map,filename,'gif','LoopCount',Inf,'DelayTime',delay);
    else
        imwrite(A,map,filename,'gif','writeMode','append','DelayTime',delay);
    end
end

```

```

saveas(gcf, strcat(maindir, '\figures\surf_stdev\', num2str(Re(i)), '_surf_stdev'), ...
    'png');
set(gcf, 'visible', 'off');
end

filename=strcat(maindir, '\gifs\surf_stdev_ub.gif');
for i=1:m % Standard Deviation / Bulk velocity "u_{rms}/u_{bulk}"
    figure('Name', 'NonDim Stdev - SurfPlot', 'NumberTitle', 'off')
    hold on
    surf(X,Y,STDV(:,:,i)./velb(i), 'FaceColor', 'interp');
    title(strcat('Re= ', num2str(Re(i)), ' (u_{rms}/u_b)'));
    xlabel('x/D_h');
    ylabel('y/D_h');
    view(0,90);
    rectangle('position', [rib1xo, rib1yo, rib1w, rib1h], 'Facecolor', [0,0,0], ...
        'EdgeColor', 'k');
    rectangle('position', [rib2xo, rib2yo, rib2w, rib2h], 'Facecolor', [0,0,0], ...
        'EdgeColor', 'k');
    axis('tight');
    pbaspect([aspect 1 1])
    grid on;
    colorbar;
    caxis([nonstdv_min nonstdv_max]);
    pause(1/2);
    [A, map] = rgb2ind(frame2im(getframe(gcf)), 256);
    if i == 1
        imwrite(A, map, filename, 'gif', 'LoopCount', Inf, 'DelayTime', delay);
    else
        imwrite(A, map, filename, 'gif', 'writeMode', 'append', 'DelayTime', delay);
    end
    saveas(gcf, strcat(maindir, '\figures\surf_stdev_ub\', num2str(Re(i)), ...
        '_surf_stdev_ub'), 'png');
    set(gcf, 'visible', 'off');
end
clc
disp('Navigate to section:')
disp('Contour Plots (Non-D Velocity, TI, STDEV, Non-D STDEV)')

```

### Contour Plots (Non-D Velocity, TI, STDEV, Non-D STDEV)

```

clc
filename=strcat(maindir, '\gifs\cont_vel.gif');
for i=1:m % Non-Dimensional Average Velocity "u_{avg}/u_{bulk}"
    figure('Name', 'NonDim Velocity - ContPlot', 'NumberTitle', 'off')
    contourf(X,Y,AVGL(:,:,i)./velb(i), contlyr);
    title(strcat('Re= ', num2str(Re(i)), ' (u_{avg}/u_b)'));
    xlabel('x/D_h');
    ylabel('y/D_h');
    caxis([nonavg1_min nonavg1_max]);
    axis('tight');
end

```

```

pbaspect([aspect 1 1])
colorbar;
rectangle('position', [probe1xo, probe1yo, probe1w, probe1h], 'Facecolor', ...
    [1,1,1], 'EdgeColor', 'w');
rectangle('position', [rib1xo, rib1yo, rib1w, rib1h], 'Facecolor', [0,0,0], ...
    'EdgeColor', 'k');
rectangle('position', [probe2xo, probe2yo, probe2w, probe2h], 'Facecolor', ...
    [1,1,1], 'EdgeColor', 'w');
rectangle('position', [rib2xo, rib2yo, rib2w, rib2h], 'Facecolor', [0,0,0], ...
    'EdgeColor', 'k');
[A, map] = rgb2ind(frame2im(getframe(gcf)), 256);
if i == 1
    imwrite(A, map, filename, 'gif', 'LoopCount', Inf, 'DelayTime', delay);
else
    imwrite(A, map, filename, 'gif', 'writeMode', 'append', 'DelayTime', delay);
end
saveas(gcf, strcat(maindir, '\figures\cont_vel\ ', num2str(Re(i)), '_cont_vel'), ...
    'png');
set(gcf, 'visible', 'off');
end

filename=strcat(maindir, '\gifs\cont_uvel.gif');
for i=1:m % Non-Dimensional Average Velocity Uncertainty "%U(u_{avg}/u_{bulk})"
    figure('Name', 'NonDim Velocity Uncertainty - ContPlot', 'NumberTitle', 'off')
    contourf(X, Y, NONVELUNCRTPRCNT(:, :, i), contlyr);
    title(strcat('Re= ', num2str(Re(i)), ' (%U(u_{avg}/u_b))'));
    xlabel('x/D_h');
    ylabel('y/D_h');
    caxis([nonveluncrtprcnt_min nonveluncrtprcnt_max]);
    axis('tight');
    pbaspect([aspect 1 1])
    colorbar;
    rectangle('position', [probe1xo, probe1yo, probe1w, probe1h], 'Facecolor', ...
        [1,1,1], 'EdgeColor', 'w');
    rectangle('position', [rib1xo, rib1yo, rib1w, rib1h], 'Facecolor', [0,0,0], ...
        'EdgeColor', 'k');
    rectangle('position', [probe2xo, probe2yo, probe2w, probe2h], 'Facecolor', ...
        [1,1,1], 'EdgeColor', 'w');
    rectangle('position', [rib2xo, rib2yo, rib2w, rib2h], 'Facecolor', [0,0,0], ...
        'EdgeColor', 'k');
    [A, map] = rgb2ind(frame2im(getframe(gcf)), 256);
    if i == 1
        imwrite(A, map, filename, 'gif', 'LoopCount', Inf, 'DelayTime', delay);
    else
        imwrite(A, map, filename, 'gif', 'writeMode', 'append', 'DelayTime', delay);
    end
    saveas(gcf, strcat(maindir, '\figures\cont_uvel\ ', num2str(Re(i)), '_cont_uvel'), ...
        'png');
    set(gcf, 'visible', 'off');
end

filename=strcat(maindir, '\gifs\cont_ti.gif');

```



```

for i=1:m % Turbulence Intensities "u_{rms}/u_{avg}"
figure('Name','TI - ContPlot','NumberTitle','off')
contourf(X,Y,TI(:,:,i),contlyr);
title(strcat('Re= ',num2str(Re(i)), ' (TI_b)'));
xlabel('x/D_h');
ylabel('y/D_h');
caxis([ti_min ti_max]);
axis('tight');
pbaspect([aspect 1 1])
colorbar;
rectangle('position',[probe1xo,probe1yo,probe1w,probe1h],'Facecolor',[1,1,1],...
'EdgeColor','w');
rectangle('position',[rib1xo,rib1yo,rib1w,rib1h],'Facecolor',[0,0,0],...
'EdgeColor','k');
rectangle('position',[probe2xo,probe2yo,probe2w,probe2h],'Facecolor',...
[1,1,1],'EdgeColor','w');
rectangle('position',[rib2xo,rib2yo,rib2w,rib2h],'Facecolor',[0,0,0],...
'EdgeColor','k');
[A,map] = rgb2ind(frame2im(getframe(gcf)),256);
if i == 1
imwrite(A,map,filename,'gif','LoopCount',Inf,'DelayTime',delay);
else
imwrite(A,map,filename,'gif','WriteMode','append','DelayTime',delay);
end
saveas(gcf,strcat(maindir,'\figures\cont_ti\',num2str(Re(i)),'_cont_ti'),...
'png');
set(gcf,'visible','off');
end

filename=strcat(maindir,'\gifs\cont_uti.gif');
for i=1:m % Turbulence Intensity Uncertainties "%U(u_{rms}/u_{avg})"
figure('Name','TI Uncertainties - ContPlot','NumberTitle','off')
contourf(X,Y,TIUNCRTPRCNT(:,:,i),contlyr);
title(strcat('Re= ',num2str(Re(i)), ' (TI_b)'));
xlabel('x/D_h');
ylabel('y/D_h');
caxis([tiuncrtprcnt_min tiuncrtprcnt_max]);
axis('tight');
pbaspect([aspect 1 1])
colorbar;
rectangle('position',[probe1xo,probe1yo,probe1w,probe1h],'Facecolor',[1,1,1],...
'EdgeColor','w');
rectangle('position',[rib1xo,rib1yo,rib1w,rib1h],'Facecolor',[0,0,0],...
'EdgeColor','k');
rectangle('position',[probe2xo,probe2yo,probe2w,probe2h],'Facecolor',...
[1,1,1],'EdgeColor','w');
rectangle('position',[rib2xo,rib2yo,rib2w,rib2h],'Facecolor',[0,0,0],...
'EdgeColor','k');
[A,map] = rgb2ind(frame2im(getframe(gcf)),256);
if i == 1
imwrite(A,map,filename,'gif','LoopCount',Inf,'DelayTime',delay);
else

```

```

        imwrite(A,map,filename,'gif','writeMode','append','DelayTime',delay);
    end
    saveas(gcf,strcat(maindir,'\figures\cont_uti\' ,num2str(Re(i)),'_cont_uti'),...
        'png');
    set(gcf,'visible','off');
end

filename=strcat(maindir,'\gifs\cont_stdev.gif');
for i=1:m % Standard Deviation "u_{rms}"
    figure('Name','Stdev - ContPlot','NumberTitle','off')
    load(strcat(maindir,'\stdev\' ,num2str(Re(i)),'_stdev.mat'));
    contourf(X,Y,STDV(:,:,i),contlyr);
    title(strcat('Re= ',num2str(Re(i)),' (u_{rms})'));
    xlabel('x/D_h');
    ylabel('y/D_h');
    caxis([stdev_min stdev_max]);
    axis('tight');
    pbaspect([aspect 1 1])
    colorbar;
    rectangle('position',[probe1xo,probe1yo,probe1w,probe1h],'Facecolor',...
        [1,1,1],'EdgeColor','w');
    rectangle('position',[rib1xo,rib1yo,rib1w,rib1h],'Facecolor',[0,0,0],...
        'EdgeColor','k');
    rectangle('position',[probe2xo,probe2yo,probe2w,probe2h],'Facecolor',...
        [1,1,1],'EdgeColor','w');
    rectangle('position',[rib2xo,rib2yo,rib2w,rib2h],'Facecolor',[0,0,0],...
        'EdgeColor','k');
    [A,map] = rgb2ind(frame2im(getframe(gcf)),256);
    if i == 1
        imwrite(A,map,filename,'gif','LoopCount',Inf,'DelayTime',delay);
    else
        imwrite(A,map,filename,'gif','writeMode','append','DelayTime',delay);
    end
    saveas(gcf,strcat(maindir,'\figures\cont_stdev\' ,num2str(Re(i)),'...
        '_cont_stdev'),'png');
    set(gcf,'visible','off');
end

filename=strcat(maindir,'\gifs\cont_stdev_ub.gif');
for i=1:m % Standard Deviation "u_{rms} /u_{bulk}"
    figure('Name','NonDim Stdev - ContPlot','NumberTitle','off')
    load(strcat(maindir,'\stdev\' ,num2str(Re(i)),'_stdev.mat'));
    contourf(X,Y,STDV(:,:,i)./velb(i),contlyr);
    title(strcat('Re= ',num2str(Re(i)),' (u_{rms}/u_b)'));
    xlabel('x/D_h');
    ylabel('y/D_h');
    caxis([nonstdv_min nonstdv_max]);
    axis('tight');
    pbaspect([aspect 1 1])
    colorbar;
    rectangle('position',[probe1xo,probe1yo,probe1w,probe1h],'Facecolor',...
        [1,1,1],'EdgeColor','w');

```

```

rectangle('position',[rib1xo,rib1yo,rib1w,rib1h],'Facecolor',[0,0,0],...
'EdgeColor','k');
rectangle('position',[probe2xo,probe2yo,probe2w,probe2h],'Facecolor',...
[1,1,1],'EdgeColor','w');
rectangle('position',[rib2xo,rib2yo,rib2w,rib2h],'Facecolor',[0,0,0],...
'EdgeColor','k');
[A,map] = rgb2ind(frame2im(getframe(gcf)),256);
if i == 1
    imwrite(A,map,filename,'gif','LoopCount',Inf,'DelayTime',delay);
else
    imwrite(A,map,filename,'gif','WriteMode','append','DelayTime',delay);
end
saveas(gcf,strcat(maindir,'\figures\cont_stdev_ub\' ,num2str(Re(i)),...
'_cont_stdev_ub'),'png');
set(gcf,'visible','off');
end

% clearvars -except avgvel n Re stdev velb X x x_Dh y Y y_Dh zero_pts xmax ymax
disp('Navigate to section:')
disp('Scatter Plots (Non-D Velocity, TI, STDEV, Non-D STDEV)')

```

### Scatter Plots (Non-D Velocity, TI, STDEV, Non-D STDEV)

```

clc
% U/Ub "Velocity Scaled Plot"
for i=1:m
    a=AVGL(:, :, i)./velb(i);
    figure('Name','NonDim Velocity - ScatPlot','NumberTitle','off')
    hold on
    for j=1:xmax
        subplot(2,ceil(xmax/2),j)
        hold on
        plot(a(:,j),y_Dh,'.','MarkerSize',6,'Color','k')
        set(gca,'FontSize',6)
        xlabel('u/u_b')
        ylabel('y/Dh')
        ylim([0 ceil(max(y_Dh*10))/10])
        xlim([0 ceil(10*nonavg1_max)/10])
        text(0.3,ceil(max(y_Dh*10))/10,strcat('Loc.',num2str(j)),'FontSize',8)
        hold off
    end
    if mod(j/2,2)==0
        b=subplot(2,ceil(xmax/2),ceil(m/2));
    else
        b=subplot(2,ceil(xmax/2),ceil((m+1)/2));
    end
    title(b,strcat('Re= ',num2str(Re(i)), ' (u/u_b)'), 'FontSize',10);
    saveas(gcf,strcat(maindir,'\figures\scat_vel\' ,num2str(Re(i)),'_scat_vel'),...
'png');
    set(gcf,'visible','off');
end

```

```

end
hold off
clearvars a b i j

% %U(U/Ub) "Non-dimensional velocity Uncertainty Plot"
for i=1:m
    a=NONVELUNCRTPRCNT(:, :, i);
    figure('Name', 'NonDim Velocity Uncertainty- ScatPlot', 'NumberTitle', 'off')
    hold on
    for j=1:xmax
        subplot(2, ceil(xmax/2), j)
        hold on
        plot(a(:, j), y_Dh, '.', 'MarkerSize', 6, 'Color', 'k')
        set(gca, 'FontSize', 6)
        xlabel('%U(u/u_b)')
        ylabel('y/Dh')
        ylim([0 ceil(max(y_Dh*10))/10])
        xlim([0 ceil(10*nonveluncrtprcnt_max)/10])
        text(0.3, ceil(max(y_Dh*10))/10, strcat('Loc.', num2str(j)), 'FontSize', 8)
        hold off
    end
    if mod(j/2, 2) == 0
        b = subplot(2, ceil(xmax/2), ceil(m/2));
    else
        b = subplot(2, ceil(xmax/2), ceil((m+1)/2));
    end
    title(b, strcat('Re= ', num2str(Re(i)), ' (%U(u/u_b))'), 'FontSize', 10);
    saveas(gcf, strcat(maindir, '\figures\scat_uvel\ ', num2str(Re(i)), '_scat_uvel'), ...
        'png');
    set(gcf, 'visible', 'off');
end
end
hold off
clearvars a b i j

% U_RMS /Ub "Tubulence Intensity, TI, Scaled by Bulk velocity" Plot
for i=1:m
    a=STDV(:, :, i) ./ AVGL(:, :, i);
    figure('Name', 'TI - ScatPlot', 'NumberTitle', 'off')
    hold on
    for j=1:xmax
        subplot(2, ceil(xmax/2), j)
        hold on
        plot(a(:, j), y_Dh, '.', 'MarkerSize', 6, 'Color', 'k')
        set(gca, 'FontSize', 6)
        xlabel('TI')
        ylabel('y/Dh')
        ylim([0 ceil(max(y_Dh*10))/10])
        xlim([0 ceil(10*ti_max)/10])
        text(0.3, ceil(max(y_Dh*10))/10, strcat('Loc.', num2str(j)), 'FontSize', 8)
        hold off
    end
    if mod(j/2, 2) == 0

```

```

        b=subplot(2,ceil(xmax/2),ceil(m/2));
    else
        b=subplot(2,ceil(xmax/2),ceil((m+1)/2));
    title(b, strcat('Re= ', num2str(Re(i)), ' (TI)'), 'FontSize', 10);
    saveas(gcf, strcat(maindir, '\figures\scat_ti\ ', num2str(Re(i)), '_scat_ti'), ...
        'png');
    set(gcf, 'visible', 'off');
    end
end
hold off
clearvars a b i j

% %U(TI) "Tubulence Intensity Uncertainty" Plot
for i=1:m
    a=TIUNCRTPRCNT(:, :, i);
    figure('Name', '%U(TI) - ScatPlot', 'NumberTitle', 'off')
    hold on
    for j=1:xmax
        subplot(2,ceil(xmax/2),j)
        hold on
        plot(a(:,j), y_Dh, '.', 'MarkerSize', 6, 'Color', 'k')
        set(gca, 'FontSize', 6)
        xlabel('%U(TI)')
        ylabel('y/Dh')
        ylim([0 ceil(max(y_Dh*10))/10])
        xlim([0 ceil(10*tiuncrtprcnt_max)/10])
        text(0.3, ceil(max(y_Dh*10))/10, strcat('Loc.', num2str(j)), 'FontSize', 8)
        hold off
    end
    if mod(j/2,2)==0
        b=subplot(2,ceil(xmax/2),ceil(m/2));
    else
        b=subplot(2,ceil(xmax/2),ceil((m+1)/2));
    title(b, strcat('Re= ', num2str(Re(i)), ' %U(TI)'), 'FontSize', 10);
    saveas(gcf, strcat(maindir, '\figures\scat_uti\ ', num2str(Re(i)), '_scat_uti'), ...
        'png');
    set(gcf, 'visible', 'off');
    end
end
hold off
clearvars a b i j

% Standard Deviation "u_{rms}"
for i=1:m
    a=STDV(:, :, i);
    figure('Name', 'u_{rms} - ScatPlot', 'NumberTitle', 'off')
    hold on
    for j=1:xmax
        subplot(2,ceil(xmax/2),j)
        hold on
        plot(a(:,j), y_Dh, '.', 'MarkerSize', 6, 'Color', 'k')
        set(gca, 'FontSize', 6)
    end
end

```

```

xlabel('u_{rms}','FontSize',7)
ylabel('y/Dh')
ylim([0 ceil(max(y_Dh*10))/10])
xlim([0 ceil(10*stdev_max)/10])
text(0.3,ceil(max(y_Dh*10))/10, strcat('Loc.',num2str(j)), 'FontSize',8)
hold off
end
if mod(j/2,2)==0
    b=subplot(2,ceil(xmax/2),ceil(m/2));
else
    b=subplot(2,ceil(xmax/2),ceil((m+1)/2));
title(b, strcat('Re= ',num2str(Re(i)), ' (u_{rms})'), 'FontSize',10);
saveas(gcf, strcat(maindir, '\figures\scat_stdev\', num2str(Re(i)), ...
    '_scat_stdev'), 'png');
set(gcf, 'visible', 'off');
end
end
hold off
clearvars a b i j

% Non-dimensional Standard Deviation "u_{rms}/u_{bulk}"
for i=1:m
    a=STDV(:, :, i)/velb(i);
    figure('Name', 'NonDim Stdev - ScatPlot', 'NumberTitle', 'off')
    hold on
    for j=1:xmax
        subplot(2,ceil(xmax/2),j)
        hold on
        plot(a(:,j),y_Dh, '.', 'MarkerSize',6, 'Color', 'k')
        set(gca, 'FontSize',6)
        xlabel('u_{rms}/u_b', 'FontSize',7)
        ylabel('y/Dh')
        ylim([0 ceil(max(y_Dh*10))/10])
        xlim([0 ceil(10*nonstdv_max)/10])
        text(0.3,ceil(max(y_Dh*10))/10, strcat('Loc.',num2str(j)), 'FontSize',8)
        hold off
    end
    if mod(j/2,2)==0
        b=subplot(2,ceil(xmax/2),ceil(m/2));
    else
        b=subplot(2,ceil(xmax/2),ceil((m+1)/2));
    title(b, strcat('Re= ',num2str(Re(i)), ' (u_{rms}/u_b)'), 'FontSize',10);
    saveas(gcf, strcat(maindir, '\figures\scat_stdev_ub\', num2str(Re(i)), ...
        '_scat_stdev_ub'), 'png');
    set(gcf, 'visible', 'off');
    end
end
hold off
clearvars a b i j

```

## Sample Convergence Testing:

```
disp('Locate Sample Convergence Velocity Data Folder');
directory=uigetdir;
cd(directory)
files=dir(directory);
fileindex=find(~[files.isdir]);
filelist=cell(length(fileindex),1);
for i=1:length(fileindex)
    filelist{i}=files(fileindex(i)).name;
end
clearvars i
clc

% Structuring Velocity Data
abclist=('a':'z').';

for i=1:length(filelist)
    s.(char(abclist(i)))=load(filelist{i});
end
```

## Sample Mean Convergence

```
% load sample from cell
for i=1:length(filelist)
    N=length(s.(char(abclist(i))));
    mu.(char(abclist(i)))=zeros(N,1);
    mu.(char(abclist(i)))(1)=s.(char(abclist(i)))(1);
    for j=2:N
        mu.(char(abclist(i)))(j)=(j-1)*mu.(char(abclist(i)))(j-1)+s.(char(abclist(i)))(j)/(j);
    end
end
```

## Sample Standard Deviation Convergence

```
% load sample from cell
% N=length(sample)
% for i=1:N(of each test)
% diff=zeros(i,1)
% diff=sample(1:i)-mu(i)
% sumsq=sum(diff.^2)
% stdev(i)=sqrt(1/(i-1)*sumsq)

% we have mean
for i=1:length(filelist)
    N=length(s.(char(abclist(i))));
    for j=1:N
```

```

        x=s.(char(abclist(i)))(1:j);
        diff=x-mu.(char(abclist(i)))(j);
        sqrdiff=diff.^2;
        ss=sum(sqrdiff);
        stdv.(char(abclist(i)))(j,1)=sqrt((1/(j-1)*ss));
    end
end

tic
for i=1:l
    for j=1:N % takes about 3.5 hours per test
        m(j,i)=mean(U(1:j,i)); % requires about an hour and ten minutes for 1000000 samples
        s(j,i)=std(U(1:j,i)); % takes about two hours for 1000000 samples
    end
end
end
toc
clearvars i
% save(strcat(maindir,'\hotwire convergence test\Re=15000_Convergence_Results.mat'),'s','U','m');

m_fluct=zeros(N,3);
s_fluct=zeros(N,3);
mbar=mean(m);
sbar=mean(s);
for i=1:3
    for j=1:N
        m_fluct(j,i)=m(j,i)-m(N,i);
        s_fluct(j,i)=s(j,i)-s(N,i);
    end
end
end
end

```

*Published with MATLAB® R2014a*

## King's Law Analysis:

```

% King's Law
disp('Locate Hotwire Calibration Folder');
directory=uigetdir;
cd(directory)
files=dir('*txt*');
filelist={files.name}';
clc

```

```

Kinglaw=zeros(4,length(filelist));

```

```

for i=1:length(filelist)

```



```

disp(filelist{i})
Re=input('what Reynolds number was this calibration for? ');
A=input('Wire voltage at 0m/s ');
G=input('Calibration wire gain ');
Offset=input('Calibration wire offset ');

Bin=load(filelist{i});
load(strcat('Calib_',strep(filelist{i},'_Calib.txt',''),'mat'),...
      'calibcoeff','nv')
volt=Bin(:,2);
% Calibration velocities
King.(strcat('Re',num2str(Re)))=nv;

% Calibration unamplified voltages squared (E^2)
King.(strcat('Re',num2str(Re)))(:,2)=(volt./G+Offset).^2;

% Natural log of calibration velocities
King.(strcat('Re',num2str(Re)))(:,3)=...
    log(King.(strcat('Re',num2str(Re)))(:,1));

% Natural log of calibration unamplified voltages
King.(strcat('Re',num2str(Re)))(:,4)=...
    log(King.(strcat('Re',num2str(Re)))(:,2)-A);

coeff=polyfit(King.(strcat('Re',num2str(Re)))(3:end,3),...
              King.(strcat('Re',num2str(Re)))(3:end,4),1);

B=exp(coeff(2));

Kinglaw(1,i)=Re;
Kinglaw(2:4,i)=[A;B;coeff(1)];
clc
end
save('kings_law','King','Kinglaw')

```

*Published with MATLAB® R2014a*

## REFERENCES

- [ 1 ] L. Ahmed, C. Vergos, P. K. Tran, W. Wang, and J. S. Kapat. "Investigation of Pressure Drop and Heat Transfer Behavior of a Square Channel with 45° Angle Ribs at Wide Range of Reynolds Numbers", 51st AIAA/SAE/ASEE Joint Propulsion Conference, 2015.
- [ 2 ] Han, J.C., Park, J.S., and Lei, C.K., 1985, "Heat Transfer Enhancement in Channels with Turbulence Promoters," ASME Journal of Engineering for Gas Turbines and Power, 107, pp. 628-635.
- [ 3 ] J. C. Han and H. C. Chen, "Turbine Blade Internal Cooling Passages with Rib Turbulators," *Journal of Propulsion Power*, vol. 22, no. 2, pp. 226-248, 2006.
- [ 4 ] J. C. Han, S. Ou, J. Park and C. K. Lei, "Augmented Heat Transfer in Rectangular Channels of Narrow Aspect Ratios with Rib Turbulators," *Int. J. Heat Mass Transfer*, vol. 32, pp. 1619-1630, 1989.
- [ 5 ] H. J. C., L. R. Glicksman and W. M. Rohsenow, "An Investigation of Heat Transfer and Friction for Rib-Roughened Surfaces," *Int. J. Heat Mass Transfer*, vol. 21, pp. 1143-1156, 1978.
- [ 6 ] Han, J. C., 1984, "Heat Transfer and Friction in Channels with Two Opposite Rib-Roughened Walls," ASME J. Heat Transfer, 106, pp. 774-781.

- [ 7 ] J. S. Park, J. C. Han, Y. Huang, S. Ou and R. J. Boyle, "Heat Transfer Performance Comparisons of Five Different Rectangular Channels with Parallel Angled Ribs," *Int. J. Heat Mass Transfer*, vol. 35, no. 11, pp. 2891-2903, 1992.
- [ 8 ] M. E. Taslim and G. Korotky, "Low-Aspect-Ratio Rib Heat Transfer Coefficient Measurements in a Square Channel," *Journal of Turbomachinery*, vol. 120, pp. 831-838, 1998.
- [ 9 ] M. Taslim and A. Lengkong, "45 deg Round-Corner Rib Heat Transfer Coefficient Measurements in a Square Channel," *Journal of Turbomachinery*, vol. 121, pp. 272-279, 1999.
- [ 10 ] M. E. Taslim and C. M. Wadsworth, "An Experimental Investigation of the Rib Surface-Averaged Heat Transfer Coefficient in a Rib-Roughened Square Passage," *Journal of Turbomachinery*, vol. 119, pp. 381-389, 1997.
- [ 11 ] F. P. Berger and K. Hau, "Local Mass/ Heat Transfer Distribution on Surfaces Roughened with Small Square Ribs.," *International J. Heat and Mass Transfer*, vol. 22, pp. 1645-1656, 1979.
- [ 12 ] J. Bailey and R. Bunker, "Heat Transfer and Friction in Channels with Very High Blockage 45° Staggered Turbulators.," in *ASME*, 2003.
- [ 13 ] P. T. I. T. K. T. K. W. C. Z. Wang, "Heat Transfer Measurements to a Gas Turbine Cooling Passage With Inclined Ribs," *Journal of Turbomachinery*, vol. 120, pp. 63-69, 1998.

- [ 14 ] M. L. Valentino, L. Tran, M. Ricklick and J. S. Kapat, "Comparison of heat transfer and friction augmentation for symmetric and non-symmetric wedge turbulators on two opposite walls," in *47th ASME Joint Propulsion Conference & Exhibit*, San Diego, California, 2011.
- [ 15 ] N. Alkhamis, A. P. Rallabandi and J. C. Han, "Heat transfer and pressure drop correlations for square channels with v-shaped ribs at high reynolds numbers," *ASME Journal of Heat Transfer*, vol. 133, no. 11, 2011.
- [ 16 ] L.M.Wright, W. LungFu and J. Han, "Thermal performance of angled, V-shaped, and W-shaped rib turbulators in rotating rectangular cooling channels (AR=4:1)," *Journal of Turbomachinery*, vol. 126, pp. 604-614, 2004.
- [ 17 ] M. Q. M. A. G. Rau, "The Effect of Periodic Ribs on the Local Aerodynamic and Heat Transfer Performance of a Straight Cooling Channel," *Journal of Turbomachinery*, vol. 120, pp. 368-374, 1998.
- [ 18 ] A. P. Rallabandi, H. Yang and J. C. Han, "Heat Transfer and Pressure Drop Correlations for Square Channels with 45 Deg at High Reynolds Numbers.," *Journal of Heat Transfer*, vol. 131, 2009.
- [ 19 ] J. C. Han, "Heat Transfer and Friction Characteristics in Rectangular Channel with Rib Turbulators.," *ASME J. Heat transfer*, vol. 110, pp. 321-328, 1988.

- [ 20 ] P.R. Chandra, M.E. Niland, J.C. Han, Turbulent Flow Heat Transfer and Friction in a Rectangular Channel with Varying Numbers of Ribbed Walls, *ASME Journal of Turbomachinery* 119 (1997) 374-380
- [ 21 ] P.R. Chandra, C.R. Alexander, J.C. Han, Heat Transfer and Friction Behaviors in Rectangular Channels with Varying Number of Ribbed Walls, *International Journal of Heat and Mass Transfer* 46 (2003) 481-495
- [ 22 ] Han, J.C., 2004. Recent studies in turbine blade cooling. *Int. J. Rotat. Mach.*, 10: 443-457
- [ 23 ] A. P. Rallabandi, N. Alkhamis and J.-C. Han, "Heat Transfer and Pressure Drop Measurements for a Square Channel with 45 deg Round-Edged Ribs at High Reynolds Numbers," *Journal of Turbomachinery*, vol. 133, July 2011.
- [ 24 ] R. L. Webb, "Heat Transfer and Pressure Drop in Blade Cooling Channels with Turbulence Promoters," *International Journal of Heat and Mass Transfer*, vol. 24, no. 4, pp. 715-726, 1981.
- [ 25 ] S. J. Kline and F. A. McClintock, "Describing Uncertainties in Single Sample Experiments.," *Mechanical Engineering*, pp. 3-8, January, 1953.
- [ 26 ] R. Moffat, "Uncertainty Analysis in the Planning of an Experiment," *Journal of Fluids Engineering*, vol. 107, no. 2, pp. 173-181, 1985.
- [ 27 ] Champagne, F.H., Sleicher, C.A. and Wehrmann, O.H. Turbulence Measurements with Inclined Hot Wires, Part 1: Heat Transfer Experiments with Inclined Hot Wires, *J. Fluid Mech.*, 28, 1967, 153-175.

[ 28 ] Brunn H. H. 1995 Hot-Wire Anemometry: Principles and Signal Analysis (Oxford: Oxford University Press.

[ 29 ] Freymuth P 1977 Frequency response and electronic testing for constant temperature hot-wire anemometers J. Phys. E: Sci. Instrum. 10 705–10

[ 30 ] Richard B. Rivir, Mingking K. Chyu, and Paul K. Maciejewski, “Turbulence and Scale Measurements in a Square Channel with Transverse Square Ribs,” International Journal of Rotating Machinery, vol. 2, no. 3, pp. 209-218, 1996.